Alma Mater Studiorum · University of Bologna

School of Science
Department of Physics and Astronomy
Master Degree in Nuclear and Subnuclear Physics

Evaluation of Th and U contamination in the CUORE experiment using a delayed coincidence analysis

Supervisor:
Prof. Stefano Zucchelli

Co-supervisor:
Dott. Giovanni Benato

Submitted by:
Giulio Benuzzi

Academic Year 2021/2022

Abstract

The discovery of the non-zero neutrino mass, not predicted by the Standard Model, is a direct evidence of new physics.
Several open questions arise from this observation, regarding the mechanism originating the neutrino mass, the neutrino mass hierarchy, the violation of lepton number conservation in the neutrino sector and the generation of the baryon asymmetry via leptogenesis. All these questions can be addressed by the experimental search for neutrinoless double beta ($0\nu\beta\beta$) decay, a nuclear decay consisting of two simultaneous beta emissions without the corresponding emission of two antineutrinos. $0\nu\beta\beta$ decay is possible only if neutrinos are identical to antineutrinos, namely if neutrinos are Majorana particles. Several experiments are actively searching for $0\nu\beta\beta$ decay. Among these, CUORE (Cryogenic Underground Observatory for Rare Events) is employing ^{130}Te embedded in TeO_2 crystals operated as bolometers.

Rare event searches, such as CUORE, need to have an accurate understanding of the background contribution in the energy region close to the Q-value of the decaying isotope. In CUORE one of the main contributions is given by particles coming from the decay chains of contaminating nuclei, mainly ^{232}Th and ^{235,238}U, present in the active crystals of the detector or in the support structure. The main goal of this thesis is to use the 1 ton·yr CUORE data, corresponding to the first 3 years of data taking, to study these contamination by looking for events belonging to precise sub-chains of the Th and U decay chains and reconstructing their energy and time difference distributions, in a so-called delayed coincidence analysis. These results in combination with the reconstruction efficiency coming from the Monte Carlo simulations of the decay chains are then used to evaluate the specific activity of the contaminants. This is the first time this analysis technique is applied to the real CUORE data and this thesis highlights the feasibility of it while providing a starting point for further more refined studies.
A part of the obtained results are in agreement with the ones coming from previous analysis, demonstrating that additional work on delayed coincidence searches for the characterization of natural radioactive contamination might improve the understanding of the CUORE experiment background and provide a more precise determination of the contribution of specific components to the CUORE background model.

This kind of delayed coincidence analysis can also be reused in the future once the CUPID (CUORE Upgrade with Particle IDentification) experiment data will be ready to be analyzed, with the aim of improving the experiment sensitivity to the $0\nu\beta\beta$ decay of ^{100}Mo.

Contents

List of Figures

List of Tables

Introduction

The Cryogenic Underground Observatory for Rare Events (CUORE) is an experiment hosted at the Laboratori Nazionali del Gran Sasso of INFN, Italy, searching for $0\nu\beta\beta$ decay in ^{130}Te in form of TeO_2 crystals operated as bolometers. CUORE employs 988 such crystals for a total active mass of 206 kg of ^{130}Te.

Rare decay experiments such as CUORE need to have a precise understanding of the possible background contributions that will impact the detector sensitivity to the rare $0\nu\beta\beta$ decay of ^{130}Te. One of the main contributions is particles coming from radioactive decays of natural contaminating nuclei present in the TeO_2 crystals and in the surface of the copper structures that hold the CUORE towers in place inside the cryostat. The main topic of this thesis is the study of the background events coming from Th and U contamination and the search of them in the CUORE data using a delayed coincidence analysis.

The first three chapters of this thesis cover the relevant physics aspects for CUORE and describe all the experiment components together with the CUORE data processing techniques. Chapter 1 begins with a theoretical view of neutrinos in the Standard Model and on the possible descriptions of their mass generation, which is still an open problem of particle physics. Moreover, an overview of double beta decays, both with and without neutrinos, is provided. The chapter ends with a brief discussion on experimental possibilities for neutrinoless double beta decay searches. Chapter 2 describes the CUORE experiment in detail, from the bolometric detectors to all the cryostat components. Some details about the bolometric technique for particle detection are also discussed. Chapter 3 is dedicated to the CUORE data acquisition and processing which first consist of the acquisition of the signals coming from particles interacting in the crystals, and then the analysis techniques needed to produce the final datasets.

The fourth chapter is devoted to the explanation of the CUORE background model and all the analysis and simulations related to it, together with a brief introduction of the relevant background sources. Chapter 5 begins with the description of the considered decay chains, namely the ^{232}Th and ^{235,238}U ones, and the explanation of the analysis ap-

proach is given. Then the results of the studies on the various coincidences are reported. Finally, Chapter 6 describes the simulations used for the evaluation of the containment efficiency, and the determination of the specific activities (in Bq/cm^2 or Bq/kg) of the considered contaminants.

Chapter 1

Physics of Neutrinoless Double Beta Decay

1.1 Neutrinos in the Standard Model

The Standard Model (SM) of particle physics has been built around a well known gauge symmetry, namely $SU(3) \times SU(2)_L \times U(1)_Y$. Within this model, neutrinos, which are still the least understood and most interesting particles, are $SU(3)$ singlets and form $SU(2)_L$ doublets with their corresponding leptons. In the SM framework, neutrinos are massless, electrically neutral particles with a -1 hypercharge and comes in three flavours: electron, muon and tau neutrinos (ν_e, ν_μ, ν_τ). This distinction arise dynamically from the fact that weak processes involving charged leptons ($e^\pm, \mu^\pm, \tau^\pm$) create or destroy neutrinos, so the ν flavour is linked to that of the corresponding charged lepton involved in the considered process. Moreover another important fact is that neutrinos ν_α ($\alpha = e, \mu, \tau$) are produced in a left-handed (LH) chiral state while antineutrinos $\bar{\nu}_\alpha$ in a right-handed (RH) one; this distinction is needed since the whole theory needs to be invariant under CPT transformations.

The history of these peculiar particles started with their first theorization in 1931 by the Austrian physicist W. Pauli; he needed to introduce a new particle with no electric charge and close to zero mass to explain the observed continuum spectrum of beta decay, which until then was thought to be a two-body decay. Then after three years Enrico Fermi finalized the beta decay theory by including this new kind of particles and he also proposed their name: "neutrinos". However the Fermi theory predicted very rare interactions between neutrinos and matter such that their experimental observation required more than 20 years of researches.
In 1956 the Cowan and Reines experiment provided the first experimental evidence of the electron antineutrino. They used a flux coming from a nuclear reactor of the Sa-

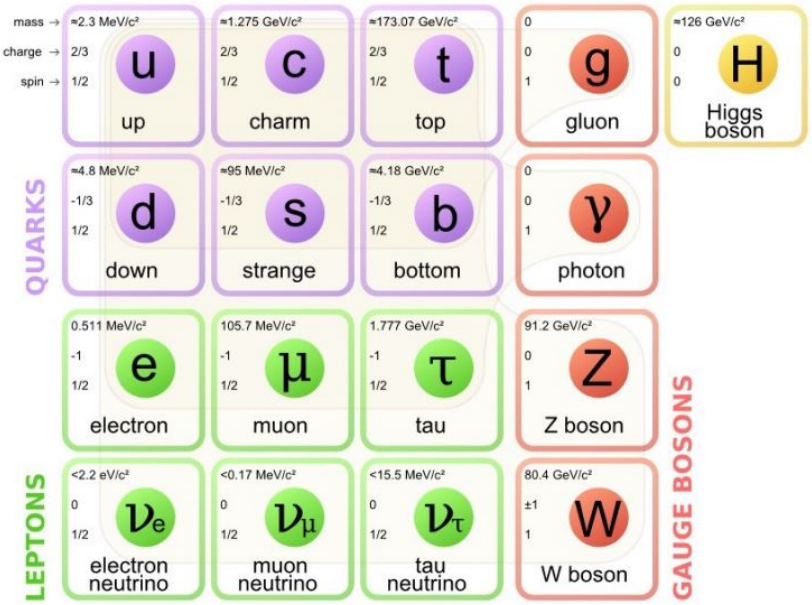

Figure 1.1: Fundamental particles predicted by the Standard Model of Particle Physics with some characteristic quantities.

vannah River complex and were able to observe the inverse beta decay $\bar{\nu}_e p \rightarrow n e^+$ in a liquid scintillator with dissolved cadmium chloride, and combining the prompt signal from the positron kinetic energy and its annihilation, together with the delayed signal from the (n,γ) reaction on ^{108}Cd. Moreover they also measured the inverse beta decay cross section obtaining a result compatible with what the Fermi theory predicted [1].
Then in 1962 the discovery of the muon neutrino ν_μ was achieved at the Brookhaven National Laboratories by L.Lederman, M.Schwartz and J.Steinberg by looking for long muon tracks produced by the reaction $\bar{\nu}_\mu X \rightarrow \mu X'$ using neutrinos coming from pions decay. So they were able to highlight that the electron and muon neutrinos are two different particles [2].
The discovery of tau neutrinos came almost 40 year later, due to the fact that the τ lepton was discovered only in 1975. The last of the three neutrinos was observed by the DONUT experiment at Fermilab where ν_τ was produced by the decay of charmed mesons [3].

1.2 Neutrino Masses

Initially neutrinos were considered to be massless particles and the SM description of particle physics rely deeply on this property. However, several indications that neutrinos are indeed massive particles were accumulated over several decades, until the first

undisputed proofs in the late nineties by two different and independent experiments: the Sudbury Neutrino Observatory [4] and the Super-Kamiokande experiment [5]. They were able to observe neutrino flavour oscillations in solar and atmospheric neutrinos, which is a possible phenomenon only for massive particles.
Neutrinos flavour oscillations are possible since neutrinos of a precise flavour $\alpha = e, \mu, \tau$ are not mass eigenstates, but they can be expressed as a combination of them, namely

$$\nu_\alpha = \sum_{i=1}^{3} U_{\alpha i} \nu_i \ . \tag{1.1}$$

The three neutrinos flavour states ν_α can be expressed as the linear combination of the mass states $\nu_i = (\nu_1, \nu_2, \nu_3)$ with given mass $m_i = (m_1, m_2, m_3)$ through the so called Pontecorvo-Maki-Nakagawa-Sakata (PMNS) matrix $U_{\alpha i}$ [6]. This matrix is parametrized by three mixing angles $\theta_{ij} \in [0, \pi/2)$ and one phase $\delta \in [0, 2\pi)$ which takes into account the possible CP violations in the ν-sector. For the sake of simplicity $c_{ij} = \cos\theta_{ij}$ and $s_{ij} = \sin\theta_{ij}$; then

$$U_{\alpha i} = \begin{pmatrix} c_{13}c_{12} & c_{13}s_{12} & s_{13}e^{-i\delta} \\ -c_{23}s_{12} - c_{12}s_{23}s_{13}e^{i\delta} & c_{12}c_{23} - s_{12}s_{23}s_{13}e^{i\delta} & c_{13}s_{23} \\ s_{12}s_{23} - c_{12}s_{23}s_{13}e^{i\delta} & -c_{12}s_{23} - s_{12}s_{23}s_{13}e^{i\delta} & c_{23}c_{13} \end{pmatrix} . \tag{1.2}$$

If neutrinos are Dirac particles, the PMNS matrix has the same number and types of parameters as the Cabibbo-Kobayashi-Maskawa quark mixing matrix. Instead, if they are Majorana particles (i.e. $\nu = \overline{\nu}$), two additional phases ϕ_{21}, ϕ_{31} have to be added [7]. From existing data it is currently impossible to clearly prove that neutrinos are Dirac or Majorana particles.

In this framework one can compute the oscillation probability $P(\nu_\alpha \to \nu_\beta)$ which describes the probability for a ν created with flavour α to be detected as a ν of flavour β; in the vacuum it takes the form

$$P(\nu_\alpha \to \nu_\beta) = \left| \sum_{j=1}^{3} U_{\beta j} U^*_{\alpha j} \exp\left(-i \frac{\Delta m^2_{j1} L}{2E_\nu} \right) \right|^2 , \tag{1.3}$$

where E_ν is the neutrino energy, L is the distance between the creation and detection point, $U_{\alpha i}$ are the entries of the PMNS matrix (Eq. 1.2) and $\Delta m^2_{ij} = m^2_i - m^2_j$ is the mass squared difference, with $i, j = 1, 2, 3$ and $i \neq j$. In the 3ν framework only two of the possible mass squared differences are independent: Δm^2_{21} and $\Delta m^2_{31(32)}$ [8].
Oscillation experiments cannot provide information on the absolute values of neutrino masses since the oscillation probability 1.3 depends only on their squared differences Δm^2_{ij}. While this kind of experiments can give precise measurements of Δm^2_{21}, they do not permit the determination of the sign of Δm^2_{31} which is needed to solve one very important open problem about neutrino phenomenology, their mass ordering:

- If $\Delta m^2_{31} > 0$ we have Normal Ordering (NO), where $m_1 < m_2 < m_3$.
- If $\Delta m^2_{31} < 0$ we have Inverted Ordering (IO), where $m_3 < m_1 < m_2$.
- If the mass of the lightest neutrino m_0 is much greater than $\sqrt{|\Delta m^2_{31}|}$ we have the Quasi Degenerate (QD) mass spectrum, where $m_1 \simeq m_2 \simeq m_3$.

In the Standard Model, neutrinos are the only neutral fundamental fermions and so they are the only particles that can be either of Dirac or Majorana type, as first theorized by Ettore Majorana in 1937 [9]. In the first case particles and antiparticles are different, for example the electron and the positron; whereas in the Majorana case particles and antiparticles are the same. This two possible natures are strictly related to the conservation of a quantum number, namely the total lepton number L, defined as

$$L = L_e + L_\mu + L_\tau \ . \tag{1.4}$$

If this quantity is indeed conserved then the neutrinos are Dirac particles, otherwise they are of the Majorana type. If a process that violates the total lepton number is observed the nature of neutrinos can be determined. The most important and sensitive process that would prove the Majorana nature of neutrinos is the neutrinoless double beta decay

$$(A, Z) \rightarrow (A, Z + 2) + 2e^- \ , \tag{1.5}$$

where A and Z are the mass and atomic number respectively and the total lepton number conservation is violated by two units.
The fact that neutrinos can be of different types with respect to charged fermions is widely used in many theories that have the goal to extend the minimal SM by also including neutrino masses. One example is the Seesaw mechanism of neutrino mass generation, predicting that neutrinos are of the Majorana type; this mechanism is particularly significant because it can explain the smallness of neutrino masses as well as the observed baryon asymmetry in the Universe.

The search for neutrinoless double beta decay is driven by crucial theoretical motivations: it will allow us to understand the nature of neutrinos and the mechanism that generates their masses while verifying if the total lepton number is violated. This latter motivation is both important for the extension of the SM and for the possible explanation of the matter/antimatter asymmetry in the Universe, so it is directly linked to matter generation.

1.2.1 Dirac and Majorana Mass Terms

To build a consistent SM Lagrangian for the lepton sector, a term that takes into account the non zero neutrino masses should be added.

A Dirac mass term can be built only through a RH neutrino field $\nu_{\alpha R}$ and a LH field $\nu_{\alpha L}$. Then neutrino masses can be generated in the same way as other fermionic masses, exploiting the standard Brout-Englert-Higgs (BEH) mechanism via Yukawa interaction. Before the electroweak symmetry breaking, this term of the Lagrangian can be written as

$$\mathcal{L} = -\sqrt{2} \sum_{\alpha,\beta} \overline{L}_{\alpha L} Y_{\alpha\beta} \nu_{\beta R} \widetilde{\Phi} + h.c. \ , \tag{1.6}$$

where α, β are the flavour indices;

$$L_{\alpha L} = \begin{pmatrix} \nu_{\alpha L} \\ l_L \end{pmatrix} , \tag{1.7}$$

is the lepton doublet, $\nu_{\beta R}$ the RH neutrino singlet, $\widetilde{\Phi}$ is the Higgs doublet and $Y_{\alpha\beta}$ is the matrix of dimensionless Yukawa couplings. After spontaneous electroweak symmetry breaking the Dirac mass term becomes

$$\mathcal{L}^D_{mass} = -\sum_{\alpha,\beta} \overline{\nu}_{\alpha L} (M^D)_{\alpha\beta} \nu_{\beta R} + h.c. \ , \tag{1.8}$$

where M^D is the product of the vacuum expectation value $v \simeq 246$ GeV with the $Y_{\alpha\beta}$ matrix. M^D can be diagonalized, allowing to write the Dirac mass term as

$$\mathcal{L}^D_{mass} = -\sum_{i=1}^{3} m_i \overline{\nu}_i \nu_i \ , \tag{1.9}$$

where $m_i > 0$ are the neutrino masses, that can be also be written as

$$m_i = v y_i \ , \tag{1.10}$$

where the y_i are the terms of the diagonalized Yukawa matrix.
Considering the NO scenario, one can assume the heaviest neutrino mass to be equivalent to the largest mass splitting:

$$m_3 \simeq \sqrt{\Delta m^2_{31}} \simeq 0.05 \text{ eV} \ , \tag{1.11}$$

where the current best fit value for Δm^2_{31} is $\sim 2.52 \times 10^{-3}$ eV^2 [10] [11]. By doing this it is possible to give an estimation of the Yukawa couplings, from Eq. 1.10 one can get

$$y_3 \simeq 10^{-13} \ , \tag{1.12}$$

while $y_{1,2}$ are even smaller. If I compare this value with the Yukawa couplings of other fermions it is clear that the neutrino Yukawa couplings are strangely small, by at least

10 orders of magnitude. This fact is usually seen as one of the main evidences against the neutrino mass generation via SM mechanisms, together with the presence of sterile RH particles that do not participate in SM interactions.

On the other hand, a massive Majorana fermion can be described by a 4 dimensional complex spinor χ similar to the classical Dirac one, but satisfying the so-called Majorana condition

$$\chi^C = C\overline{\chi}^T = \chi \ , \tag{1.13}$$

where C is the charge conjugation operator which inverts all the quantum number of a particle and it is defined as

$$C = i\gamma^2\gamma^0 \quad \text{with} \quad \gamma = \text{Dirac Matrices.} \tag{1.14}$$

From this it follows that the independent components of χ are only two with respect to the four of the Dirac spinor.
Consider now a $U(1)$ global gauge transformation of χ, namely

$$\chi \to e^{i\alpha Q}\chi \ , \tag{1.15}$$

then the condition 1.13 holds true only if $Q = 0$ which implies that χ cannot carry quantum numbers such as the electric charge or the lepton number. Moreover as stated earlier, the PMNS matrix should be extended including also the two extra CP violating phases ϕ_{21} and ϕ_{31} [7]. Then the PMNS matrix can be rewritten as

$$\mathcal{U} = UM, \quad \text{with} \quad M = diag(1, e^{i\frac{\phi_{21}}{2}}, e^{i\frac{\phi_{31}}{2}}) \ , \tag{1.16}$$

where U is the PMNS matrix of Eq. 1.2.
Within the SM neutrinos are the only particles that could be described by a Majorana spinor χ so it is possible to require that the RH neutrino field has to be equal to the charge conjugated of the LH one

$$\nu_{\alpha R} = C\overline{\nu_{\alpha L}}^T = (\nu_{\alpha L})^C, \tag{1.17}$$

which is an application of the Majorana condition 1.13. Then the Majorana neutrino field can be written as

$$\nu_\alpha = \nu_{\alpha L} + \nu_{\alpha R} = \nu_{\alpha L} + (\nu_{\alpha L})^C, \tag{1.18}$$

and then its charge conjugate ν_α^C will be clearly equal to ν_α itself, meaning that Majorana neutrinos are their own antiparticles.
Since Majorana fields cannot carry a nonzero additive quantum number, like the total lepton number (see Eq. 1.4), the mass term will not be invariant under a global $U(1)$ transformation and so it will be explained only by an extension of the SM. A simple way to introduce such a mass term is to write a dimension 5 term which is suppressed

by a very large new energy scale Λ so that the total term will have mass dimension 4, compatible with what the Lagrangian needs. A possibility is given by

$$\mathcal{L} = -\frac{1}{\Lambda}\sum_{\alpha,\beta}\overline{L}_{\alpha L}\widetilde{\Phi}Y_{\alpha\beta}\widetilde{\Phi}^{T}(L_{\alpha L})^{C} + h.c. \ . \tag{1.19}$$

After the spontaneous electroweak symmetry breaking the Majorana mass term will be written as

$$\mathcal{L}^{M}_{mass} = -\frac{1}{2}\sum_{\alpha,\beta}\overline{\nu}_{\alpha L}\frac{v^2}{\Lambda}Y_{\alpha\beta}(\nu_{\beta L})^{C} + h.c. \ , \tag{1.20}$$

with

$$M^{M} = \frac{v^2}{\Lambda}Y_{\alpha\beta} \ . \tag{1.21}$$

By diagonalizing Y with the PMNS matrix (Eq. 1.16), the neutrino masses are obtained

$$m_i = \frac{v^2}{\Lambda}y_i = \frac{v}{\Lambda}vy_i \ . \tag{1.22}$$

This latter equation allows to estimate the scale Λ, assuming that the largest of neutrino masses m_i is $m_3 \simeq 0.05$ eV and that the parameter y_3 is of the order of $10^0 - 10^{-1}$, one gets

$$\Lambda \simeq 10^{14,15} \text{ GeV} \ , \tag{1.23}$$

which is a very large energy scale that cannot be currently probed in a laboratory. This is an example of the so-called Seesaw mechanism (Type I) [12].

1.3 Double Beta Decay

Neutrino oscillations cannot be used to study the nature of neutrinos because of one main reason: flavour oscillations conserve the total lepton number.
To test the nature of these particles, it is necessary to look for processes that violate lepton number conservation. The most sensitive and important one is the neutrinoless double beta decay ($0\nu\beta\beta$). In this process, which takes place in nuclei, two neutrons (down quarks) undergo β^- decays at the same time producing two protons (up quarks) and two electrons, without neutrino emission. This missing ν emission, $\overline{\nu}_e$ to be precise, is possible if and only if neutrinos are Majorana particles because this process violates lepton number by two units and so it is not allowed in the minimal SM. For this reason the detection of this peculiar process will give clear evidence of the Majorana nature of neutrinos.

1.3.1 Two Neutrino Double Beta Decay ($2\nu\beta\beta$)

To better understand the physics of neutrinoless double beta decay, I will first introduce two neutrino double beta decay ($2\nu\beta\beta$). It still is a very rare process that takes place in nuclei, but here the two electron anti-neutrinos are present in the final state, which means that in this kind of process the total lepton number is conserved. The reaction in nuclei is written as

$$(A, Z) \rightarrow (A, Z + 2) + 2e^- + 2\overline{\nu}_e, \tag{1.24}$$

while considering elementary constituents

$$d + d \rightarrow u + u + 2e^- + 2\overline{\nu}_e \tag{1.25}$$

and its Feynman diagram is

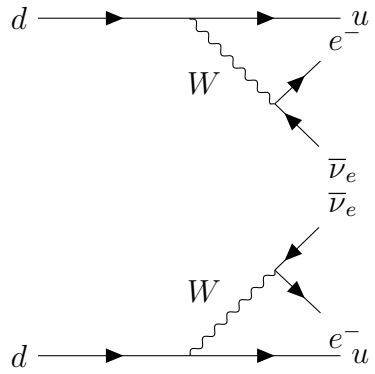

Figure 1.2: Feynman diagram for the $2\nu\beta\beta$ decay involving elementary particles.

This process is heavily suppressed since it is a second order weak process that takes place in nuclei when the single beta decay is energetically forbidden. Some suitable isotopes for which $2\nu\beta\beta$ decay searches can be made are: ^{76}Ge, ^{100}Mo, ^{130}Te and ^{136}Xe. Because of the heavy suppression the half-lives of these isotopes vary between 10^{18} and 10^{24} years.
The $2\nu\beta\beta$ half life is expressed by:

$$\frac{1}{T^{2\nu}_{1/2}(A, Z)} = G_{2\nu} g_A^4 |m_e c^2 M_{2\nu}(A, Z)|^2 \ , \tag{1.26}$$

where $G_{2\nu}$ is the phase space factor, g_A is the axial vector coupling constant, m_e the mass of the electron and $M_{2\nu}(A, Z)$ is the nuclear matrix element, that can be determined by studying nuclear properties of the isotopes present in the reaction and it is the main source of uncertainty in the calculations.
For the majority of double beta experiments, the significant quantity that can be measured in the final state of double beta decays, both with or without neutrinos, is the sum

of the kinetic energy of the produced electrons. In the $2\nu\beta\beta$ case it forms a continuous spectrum from 0 up to the endpoint energy, where the two neutrinos are produced close to at rest. This endpoint energy is the $Q_{\beta\beta}$ of the reaction and it is defined as

$$Q_{\beta\beta} = m(A, Z)c^2 - m(A, Z + 2)c^2 \ , \tag{1.27}$$

where m refers to the atomic masses.
Figure 1.3 reports the $2\nu\beta\beta$ decay spectrum, which will be very important for the discussion about $0\nu\beta\beta$ decay and it is similar to the well known spectrum of the single β decay.

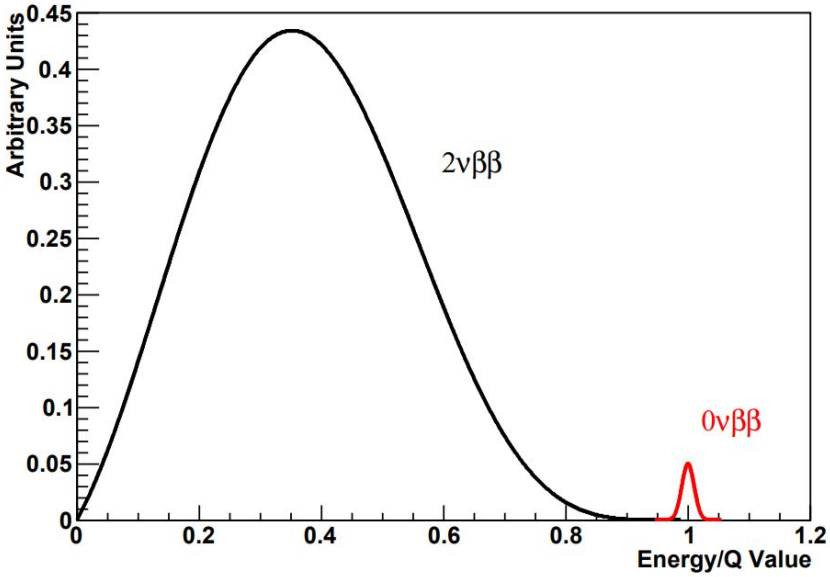

Figure 1.3: Energy spectrum for $2\nu\beta\beta$ decay (black) and, as an anticipation, for $0\nu\beta\beta$ decay (red). In the x-axis label Q Value stands for the $Q_{\beta\beta}$ of Eq. 1.27.

1.3.2 Neutrinoless Double Beta Decay ($0\nu\beta\beta$)

Neutrinoless double beta ($0\nu\beta\beta$) decay is a theorized beyond SM process that involves total lepton number violation, because in this case the final state consists of only two electrons and two up quarks. As for $2\nu\beta\beta$, the reaction is expected to take place in nuclei and it is written as

$$(A, Z) \rightarrow (A, Z + 2) + 2e^-, \tag{1.28}$$

and with only elementary constituents

$$d + d \rightarrow u + u + 2e^-, \tag{1.29}$$

then the Feynman diagram becomes

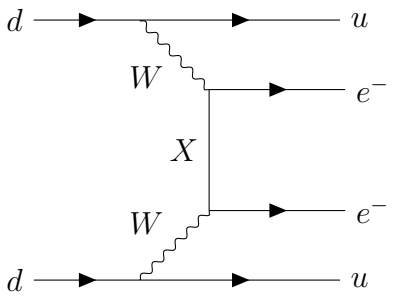

Figure 1.4: Feynman diagram for the $0\nu\beta\beta$ decay involving elementary particles.

In the simplest case, which does not involve the introduction of new particles, the exchanged particle X is one of the three known light neutrinos. Since the exchanged neutrino needs to be both emitted and absorbed it has to be equal to its antiparticle, which is possible if and only if neutrinos are Majorana particles.
Many research programs for $0\nu\beta\beta$ decay are working or are under development (see Section 1.4) because its discovery would prove that lepton number is not one of the fundamental symmetries of nature and that neutrinos are indeed Majorana fermions. Moreover, precise measurements would also give information about the neutrino mass hierarchy and mass scale [13].
Considering the light neutrino exchange, the decay half-life $T^{0\nu}_{1/2}$ can be obtained starting from the interaction Lagrangian [14], it can be expressed as

$$\frac{1}{T^{0\nu}_{1/2}(A,Z)} = G_{0\nu}(Q_{\beta\beta},Z)g_A^4|M_{0\nu}(A,Z)|^2\frac{|m_{\beta\beta}|^2}{m_e^2}, \tag{1.30}$$

where an additional term related to beyond SM physics, the effective Majorana mass $m_{\beta\beta}$, is present with respect to Eq. 1.26. $m_{\beta\beta}$ is defined as

$$m_{\beta\beta} = \sum_{i=1}^{3}\mathcal{U}_{ei}^2 m_i, \tag{1.31}$$

where $\mathcal{U}$ is the PMNS matrix of Eq. 1.16. A measurement of $T^{0\nu}_{1/2}$ would give information on the effective Majorana mass which contains the physics not explained by the minimal SM. The equation 1.31 can be expanded to make the PMNS matrix elements explicit:

$$m_{\beta\beta} = m_1|U_{e1}|^2 + m_2|U_{e2}|^2 e^{i\phi_{21}} + m_3|U_{e3}|^2 e^{i(\phi_{31}-2\delta)}, \tag{1.32}$$

where m_i are the three neutrino masses, U_{ei} are the elements of the first row of the matrix 1.2 and ϕ_{21}, ϕ_{31} and δ are the two Majorana and one Dirac phases.
The main concern in the derivation of $m_{\beta\beta}$ from experimental measurements is the calculation of the nuclear matrix element $M_{0\nu}$, which can be determined by using different

nuclear models with their chosen approximations, and does not depend on neutrino related quantities. Different nuclear models can provide very different values for $M_{0\nu}$, so its precise determination will be very important for $0\nu\beta\beta$ searches in the future. A review about this theoretical subject can be found in [15].

The determination of the effective Majorana mass would give important information on the neutrino mass spectrum and on the overall neutrinos mass scale. A deeper look into $m_{\beta\beta}$ will allow us to better understand what is already known and what will be studied by $0\nu\beta\beta$ experiments. The expanded Eq. 1.32 takes the form

$$m_{\beta\beta} = c_{12}^2 c_{13}^2 m_1 + c_{13}^2 s_{12}^2 e^{i\phi_{21}} m_2 + s_{13}^2 e^{-i2\delta} e^{i\phi_{31}} m_3, \tag{1.33}$$

which is a complex number; if for simplicity $\phi_{31} - 2\delta = \Phi$ then its absolute value is

$$\begin{aligned} |m_{\beta\beta}| &= |c_{12}^2 c_{13}^2 m_1 + c_{13}^2 s_{12}^2 e^{i\phi_{21}} m_2 + s_{13}^2 e^{i(\phi_{31}-2\delta)} m_3| = \\ &= |c_{12}^2 c_{13}^2 m_1 + c_{13}^2 s_{12}^2 (\cos\phi_{21} + i\sin\phi_{21}) m_2 + s_{13}^2 (\cos\Phi + i\sin\Phi) m_3| = \\ &= \sqrt{(c_{12}^2 c_{13}^2 m_1 + c_{13}^2 s_{12}^2 m_2 \cos\phi_{21} + s_{13}^2 m_3 \cos\Phi)^2 + (c_{13}^2 s_{12}^2 m_2 \sin\phi_{21} + s_{13}^2 m_3 \sin\Phi)^2}. \end{aligned} \tag{1.34}$$

Some of these parameters are well know while others need to be probed experimentally in the future:

- the two mixing angles θ_{12} and θ_{13} are obtained with good precision ($\sim 3\%$) by oscillation experiments, respectively by solar and short baseline nuclear reactor experiments [16];
- the neutrino masses m_i are not currently known, but the effective Majorana mass could also be written in terms of neutrino squared mass differences; oscillation experiments have measured Δm_{21}^2, which is also called *solar squared mass difference*, and the absolute value of Δm_{3l}^2 (related to the *atmospheric squared mass difference*). The sign of the latter quantity depends on the mass ordering: it will be positive for NO, with $l = 1$ and negative for the IO, with $l = 2$ [10][11][17]. Moreover, information on neutrino masses can be extracted from cosmological studies that can set upper bounds of around 0.9 eV on the total neutrino mass $\Sigma = m_1 + m_2 + m_3$ [18];
- no experimental evidence or predictions are available on the two Majorana phases ϕ_{21} and ϕ_{31}.

In the Table 1.1 the results of the most recent fits of the effective Majorana mass parameters are outlined [10][11].

Table 1.1: Most recent values for the parameters of the effective Majorana mass $m_{\beta\beta}$, excluding the two Majorana phases for which an experimental measurement is not currently available.

Parameter	Normal Ordering	Inverted Ordering
θ_{12} [°]	$33.45^{+0.77}_{-0.75}$	$33.45^{+0.78}_{-0.75}$
θ_{13} [°]	$8.62^{+0.12}_{-0.12}$	$8.61^{+0.14}_{-0.12}$
δ [°]	230^{+36}_{-25}	278^{+22}_{-30}
$\frac{\Delta m^2_{21}}{10^{-5}}$ [eV^2]	$7.42^{+0.21}_{-0.20}$	$7.42^{+0.21}_{-0.20}$
$\frac{\Delta m^2_{3l}}{10^{-3}}$ [eV^2]	$+2.510^{+0.027}_{-0.027}$ $(l=1)$	$-2.490^{+0.026}_{-0.028}$ $(l=2)$

It is important to have predictions of the effective Majorana mass because it is directly linked to the half-life of the decay (see Eq. 1.30). Notice that all the numerical bounds on $m_{\beta\beta}$ are obtained considering the 3σ error on the oscillation parameters, which are not listed in this thesis but are accessible in Ref. [11]. Moreover, notice that all the predictions for the $m_{\beta\beta}$ depends on the two Majorana phases, which are not precisely known, then to obtain the different bounds these two phases are varied in their allowed range [0°,360°].
Depending on the value of the lightest neutrino mass $m_{\downarrow}$, $m_{\beta\beta}$ behaves in different ways for the possible mass orderings, see Figure 1.5.
If $m_{\downarrow} > 10^{-2}$ eV the $m_{\beta\beta}$ bands are degenerate and the mass spectrum is considered QD. If the value of $m_{\downarrow}$ is between 10^{-3} eV and 10^{-2} eV there are combinations of the parameters entering the $m_{\beta\beta}$ definition that might lead to it vanishing and other combinations that allow a bound in the IO case. Then if $m_{\downarrow} < 10^{-3}$ eV more precise bound on $m_{\beta\beta}$ can be found for both normal and inverted mass orderings:

- In NO $m_1 < m_2 < m_3$, then in Eq. 1.34 the m_1 contribution can be neglected and an approximation of the effective Majorana mass is given by

$$|m_{\beta\beta}|^2_{NO} \simeq c^4_{13}s^4_{12}\Delta m^2_{21} + s^4_{13}\Delta m^2_{31} + 2c^2_{13}s^2_{12}s^2_{13}\sqrt{\Delta m^2_{21}\Delta m^2_{31}}\cos(\phi_{21} - \phi_{31} + 2\delta) \ , \tag{1.35}$$

  The first term is suppressed by Δm^2_{21}, the second by $\sin^4\theta_{13}$ and the last one by the same dependencies. The obtained prediction is then

$$|m_{\beta\beta}|_{NO} \simeq (1.1 - 4.2) \text{ meV} \ . \tag{1.36}$$

  In this case the scale is much smaller than the sensitivity of planned $0\nu\beta\beta$ decay experiments. The observation of anomalies in short-baseline oscillations experiments [19] might suggest the existence of sterile neutrinos in the eV scale; their contribution to the effective Majorana mass will then make this spectrum verifiable with future $0\nu\beta\beta$ decay experiments.

- Instead in IO $m_3 < m_1 < m_2$, so the m_3 contribution can be neglected. One has

$$|m_{\beta\beta}|^2_{IO} \simeq |\Delta m^2_{32}| \cos^4\theta_{13} \left(1 - \sin^2 2\theta_{12} \sin^2 \frac{\phi_{21}}{2}\right) . \tag{1.37}$$

In this case the prediction is one order of magnitude higher than the one in the Normal Ordering case, namely

$$|m_{\beta\beta}|_{IO} \simeq (15 - 50) \text{ meV} . \tag{1.38}$$

Current and planned ton scale $0\nu\beta\beta$ decay experiments aim to cover a part of this interval, thus the nature of neutrinos in the inverted ordering hypothesis will be probed.

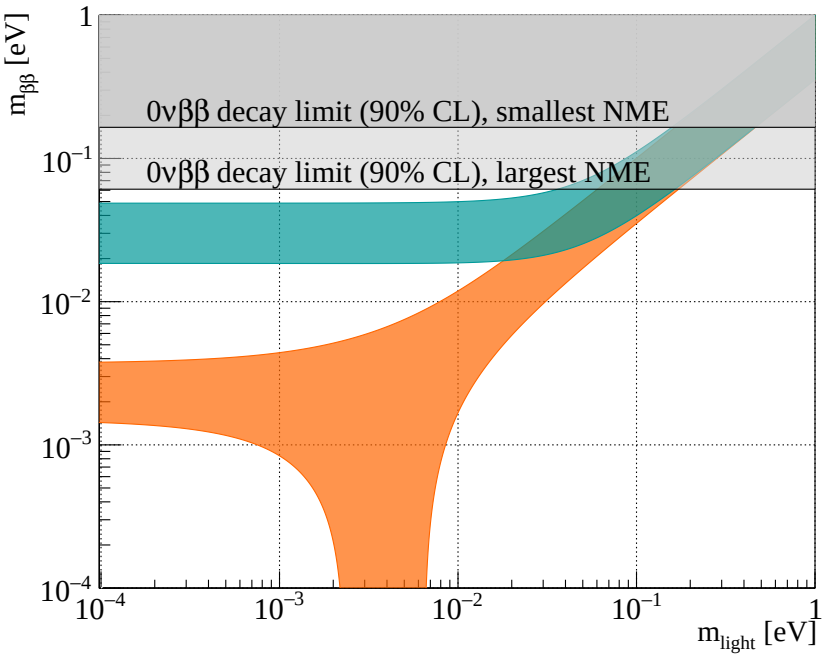

Figure 1.5: Allowed regions for $m_{\beta\beta}$ as a function of the lightest neutrino mass, assuming the central values of the PMNS matrix parameters [20]. The orange area refers to the normal ordering while the green to the inverted one. Grey areas are regions already excluded by $0\nu\beta\beta$ decay experiments.

In the QD spectrum case some approximations can be done, here three neutrino masses are similar $m_1 \simeq m_2 \simeq m_3 = m_0$. With this spectrum hypothesis the $m_{\beta\beta}$ takes the form

$$|m_{\beta\beta}|_{QD} \simeq m_0 \left|(\cos^2\theta_{12} + \sin^2\theta_{12} e^{i\phi_{21}}) \cos^2\theta_{13} + e^{i(\phi_{31} - 2\delta)} \sin^2\theta_{13}\right| , \tag{1.39}$$

then by plugging in the numerical predictions

$$|m_{\beta\beta}|_{QD} \simeq (0.29 - 1.0)\ m_0\ . \tag{1.40}$$

As expected this prediction depends on the scale of neutrino masses which its determination is currently an open problem [21]. In the last years, the KATRIN experiment, exploiting the tritium β decay, were able to put an upper bound on m_0 at the order of 0.9 eV (at 90% confidence level) [22]; improving previous results from other ^{3}H decay searches such as the Mainz [23] and Troitsk [24] experiments. In the future the KATRIN experiment will aim to investigate this upper bound on m_0 with a better sensitivity (~ 0.2 eV).

Another very useful way to look at the effective Majorana mass is by writing it as a function of the lightest neutrino mass $m_\downarrow$: m_1 in the NO spectrum and m_3 within the IO one. Because the masses of the other two neutrinos can then be written in terms of $m_\downarrow$ and the mass squared differences (Δm^2_{21}, $\Delta m^2_{31(32)}$). In the NO case

$$\begin{aligned} m_1 &= m_\downarrow\ , \\ m_2 &= \sqrt{m_\downarrow^2 + \Delta m^2_{21}}\ , \\ m_3 &= \sqrt{m_\downarrow^2 + \Delta m^2_{31}}\ . \end{aligned} \tag{1.41}$$

While in the IO one

$$\begin{aligned} m_1 &= \sqrt{m_\downarrow^2 - \Delta m^2_{32} - \Delta m^2_{21}}\ , \\ m_2 &= \sqrt{m_\downarrow^2 - \Delta m^2_{32}}\ , \\ m_3 &= m_\downarrow\ . \end{aligned} \tag{1.42}$$

This descriptions allow to obtain the graph shown in Figure 1.5, where the allowed regions of $m_{\beta\beta}$ are obtained by computing it using its two possible approximations (in NO and IO) while propagating the uncertainties of the known parameters and considering the extreme values of the ranges of the unknown Majorana phases [25].

Before discussing about the current and future experimental $0\nu\beta\beta$ decay searches, one has to keep in mind that present data cannot predict effectively what is the correct ordering, but future experiments will aim to have an high enough sensitivity to be able to cover the lower part of the inverted ordering $m_{\beta\beta}$ allowed region (see green band in Figure 1.5); if possible this will give crucial information about this open problem in neutrino physics.

1.4 Experimental $0\nu\beta\beta$ Decay Searches

1.4.1 $T^{0\nu}_{1/2}$ and $m_{\beta\beta}$ Dependences on Experiment Features

To better understand current results and bounds obtained by $0\nu\beta\beta$ decay experiments, one has to acknowledge how the main observable of this kind of searches (i.e. the decay half-life $T^{0\nu}_{1/2}$) depends on quantities directly linked to the experimental set up.
Figure 1.3 shows that $0\nu\beta\beta$ experiments need an excellent energy resolution and detection efficiency in a Region Of Interest (ROI) around $Q_{\beta\beta}$.
During a time interval t, the number of occurring decays is

$$N_D = N_0\left(1 - e^{-\frac{\ln 2}{T^{0\nu}_{1/2}}t}\right) , \tag{1.43}$$

where N_0 is the initial number of the emitting isotopes. Since $T^{0\nu}_{1/2}$ is much greater than the usual experimental time scale t, N_D can be expanded as

$$N_D \simeq N_0\frac{\ln 2}{T^{0\nu}_{1/2}}t \ . \tag{1.44}$$

A common solution to maximize the sensitivity of the detector is to build them directly with material that contains the decaying isotope. Some materials can be isotopically enriched, yielding an increase of N_0, which can be written as

$$N_0 = \frac{N_A}{m_a}f_{en}m \ , \tag{1.45}$$

where N_A is the Avogadro number, m_a the atomic mass of the isotope, f_{en} is the enrichment fraction and m the total mass of decaying material. This the expected number of signal events becomes

$$N_S = N_D \cdot f_{AV} \cdot \varepsilon = \frac{N_A \ln 2}{T^{0\nu}_{1/2}m_a}f_{en} \cdot f_{AV} \cdot \varepsilon \cdot mt \tag{1.46}$$

where f_{AV} is the active volume fraction and ε the total efficiency. The quantity mt is also called exposure (expressed in kg·yr), and captures the rate with which an experiment can collect signal events.
It is very important to consider the number of background events N_B in the ROI. These kinds of events might be caused by a lot of different sources, but the most relevant ones are radioactive contamination of the detector components or the cosmic radiation. N_B can be expressed as

$$N_B = \mathrm{BI} \cdot \Delta E \cdot mt \ , \tag{1.47}$$

BI stands for Background Index which is the average background level in the ROI and it is expressed in counts/(keV·kg·yr) and ΔE is the width in keV of the ROI.

To have a higher sensitivity to possible $0\nu\beta\beta$ decay events N_B has to be minimized, that is feasible via a lower BI or by minimizing the ROI so that fewer background events will be present in it. The background can be suppressed in an active or passive way: the latter means by screening the detector from external events while the former means by implementing particle discrimination or by looking to events topologies. While the ROI minimization is related to an optimization of the energy resolution ΔE.

The sensitivity to $T^{0\nu}_{1/2}$ can be estimated by considering it as the time needed to collect a number of signal events N_S equal to the uncertainty on the number of background events N_B, this holds for high background experiments like the CUORE experiment. Since N_B follows the Poisson distribution this condition becomes

$$N_S = \sqrt{N_B} \ , \tag{1.48}$$

then from Eq. 1.46 and 1.47

$$\frac{N_A \ln 2}{T^{0\nu}_{1/2} m_a} f_{en} \cdot f_{AV} \cdot \varepsilon \cdot mt = \sqrt{\mathrm{BI} \cdot \Delta E \cdot mt} \ , \tag{1.49}$$

and by isolating $T^{0\nu}_{1/2}$

$$T^{0\nu}_{1/2} = \frac{N_A \ln 2}{m_a} f_{en} \cdot f_{AV} \cdot \varepsilon \cdot \sqrt{\frac{mt}{\mathrm{BI} \cdot \Delta E}} \ . \tag{1.50}$$

The result from this description is that the half-life $T^{0\nu}_{1/2}$ depends on the square root of the exposure divided by the BI. Additionally, from Eq. 1.30, $|m_{\beta\beta}|$ depends on $1/\sqrt{T^{0\nu}_{1/2}}$; so an exposure increase and a background reduction will correspond to an improvement on the effective Majorana mass.

1.4.2 Current Results from $0\nu\beta\beta$ Decay Experiments

There are a lot of experiments focused on this open problem of neutrino physics, but at present times $0\nu\beta\beta$ decay events has not been observed yet. Then a variety of projects are currently arising, aiming to reach an improved sensitivity.
Neutrinoless double beta decay experiments mainly differ depending on the chosen isotope, because different isotopes have distinct $Q_{\beta\beta}$ and its position in the energy spectrum is correlated to the possible background events in the ROI.

- If the $Q_{\beta\beta}$ is lower than 2615 keV, which is the ^{208}Tl γ line and it is the end point of natural gamma radioactivity, then the background coming from this kind of radiation is not negligible and has to be accounted for in the design of the experiment.

- If $Q_{\beta\beta}$ is above the 2615 keV threshold the background is much lower and mainly consists of cosmic rays and α radiations. So an isotope with high $Q_{\beta\beta}$ is typically favored for $0\nu\beta\beta$ searches.

Other factors that impact the choice of the isotope are its natural abundance, the enrichment possibility and its availability or cost.
At the same time, the isotope choice is related to the features of the detector such as the efficiency and the energy resolution, but also the possibility to scale the technology in terms of time of work and active mass (*exposure*) while maintaining the detector stability.
Moreover, background reduction aspects of the detector have to be taken into account when considering the possible isotopes and detection technologies. The most important ones are the level of radiopurity of the material and the possibility to shield itself from external background sources.
Table 1.2 reports the reaction, the $Q_{\beta\beta}$ and the natural isotopic abundance of the most studied $\beta\beta$ emitting isotopes that might undergo neutrinoless double beta decay.

Table 1.2: List of the most commonly used isotopes in $0\nu\beta\beta$ decay experiments. Listed here are the reactions, the values of their $Q_{\beta\beta}$ and the isotopic abundances (from [26]).

Isotope	Reaction	$Q_{\beta\beta}$ [keV]	Isotopic Abundance [%]
^{48}Ca	^{48}Ca$\rightarrow^{48}$Ti	4268 [27]	0.2
^{76}Ge	^{76}Ge$\rightarrow^{76}$Se	2039 [28]	7.7
^{82}Se	^{82}Se$\rightarrow^{82}$Kr	2998 [29]	8.7
^{96}Zr	^{96}Zr$\rightarrow^{96}$Mo	3356 [30]	2.8
^{100}Mo	^{100}Mo$\rightarrow^{100}$Ru	3034 [28]	9.8
^{116}Cd	^{116}Cd$\rightarrow^{116}$Sn	2813 [31]	7.5
^{130}Te	^{130}Te$\rightarrow^{130}$Xe	2527 [31]	34.1
^{136}Xe	^{136}Xe$\rightarrow^{136}$Ba	2456 [32]	8.9

In the last part of the first chapter I will briefly review two $0\nu\beta\beta$ decay experiments, namely GERDA and KamLAND-Zen, because they obtained the best results related to the investigated isotope. They used different isotopes and analysis strategies and of course these are only an example of the many experiments in working in this research field or planned for the future. This review about them will be useful if compared with the CUORE experiment description, which will be discussed in a deeper way in the next chapters.

GERDA

The GERmanium Detector Array (GERDA) experiment, was located at the Laboratori Nazionali del Gran Sasso (LNGS) in Italy, searched for the $0\nu\beta\beta$ decay of ^{76}Ge using high purity Ge detectors made of a material enriched in ^{76}Ge.
GERDA used a total mass of 35.6 kg of high purity Ge detectors placed inside a liquid Ar cryostat that was used both for cooling and shielding from external particles coming from cosmic rays. This cryostat was then surrounded by a tank containing very pure water that serves as an additional shield and as a Cherenkov muon veto, surrounded by Photo Multiplier Tubes (PMTs), and instrumented with plastic scintillators at the top. A scheme of the GERDA experimental setup is shown in Figure 1.6 [33] [34].

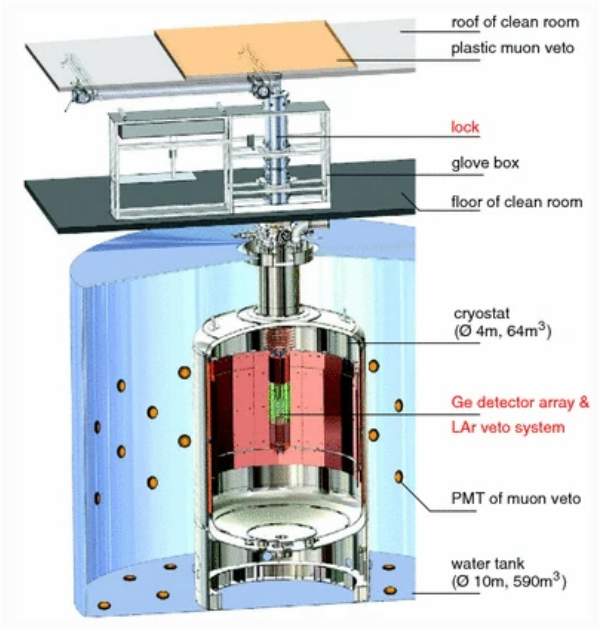

Figure 1.6: GERDA experimental setup. Above the tank there was a clean room with a glove box and a lock for the assembly and placement of the inner part of the detector. For an in depth description of all components see [34].

Phase-II of the GERDA experiment was designed to improve the sensitivity on $T^{0\nu}_{1/2}$ by at least one order of magnitude with respect to their phase-I results [35]; to do this the energy resolution and the background events discrimination had to be improved too. They moved from traditional high purity Ge detectors to broad energy ones (BEGe) ones and instrumented the liquid Ar cryostat to behave as veto.
The phase-I already reached almost an optimal background rejection, so to improve it even more they noticed that:

- Most background events came from radioactive nuclei in materials close to the main

detectors. So they opted to reduce to the minimum these materials around it or to replace them with ones with a lower level of radioactive contamination.

- $0\nu\beta\beta$ decay events will deposit the $Q_{\beta\beta}$ energy closely to the detector (R $\sim$ mm), while background events (such as $2\nu\beta\beta$ decay events) might deposit their energy also in the liquid Ar. So using the topology of background events and applying scintillation readout technologies to the liquid Ar cryostat (LAr veto system), the background contribution was decreased even more.

The GERDA experiment was crucial because of its capability of rejecting background events. This property can be compared with other non-^{76}Ge experiments via a normalized BI. The GERDA BI was at least a factor five smaller than the one obtained by other experiments. In particular they reached a BI in ROI of 0.6×10^{-4} counts/(keV·kg·yr). During phase-II a clear signal event wasn't detected, so the GERDA collaboration was able to set a lower bound on the $0\nu\beta\beta$ decay half life: $T^{0\nu}_{1/2} > 8.0 \times 10^{25}$ yr at a 90% confidence level (CL). This limit, using the knowledge on phase space factors and nuclear matrix elements, was translated into an upper bound on the effective Majorana mass $m_{\beta\beta}$, namely $m_{\beta\beta} < (120 - 260)$ meV [33].
The energy spectrum in the analysis range around $Q_{\beta\beta}$ is portrayed in Figure 1.7.

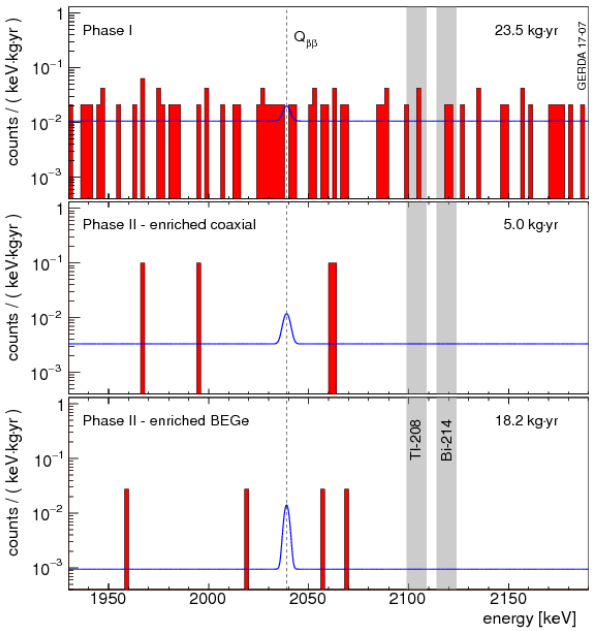

Figure 1.7: Energy spectrum, in a zoomed region around the $Q_{\beta\beta}$, for phase-I/II coaxial Ge detectors and phase-II BEGe ones. The blue lines show the supposed $0\nu\beta\beta$ signal for $T^{0\nu}_{1/2} = 8.0 \times 10^{25}$ yr on top of their own constant background. The grey vertical bands are excluded from known photon lines. For a full depiction of the energy spectra see Figure 1 in [33].

This experimental research group has subsequently teamed-up with the one of the MAJORANA Demonstrator experiment, which also exploits the ^{76}Ge as $0\nu\beta\beta$ decay source in a "background free" regime but uses different data acquisition technologies [36]. Having two independent experiments that work with similar background is leading to the construction of the LEGEND experiment that will combine the strengths of the two research collaborations. This experiment will use 200 kg of ^{76}Ge and will aim to a half life scale of 10^{27} yr [37].

KamLAND-Zen

KamLAND-Zen [38] is a very high sensitivity experiment searching for neutrinoless double beta decay of ^{136}Xe, with $Q_{\beta\beta}$ at 2456 keV. This experiment is located in the Kamioka mine in Japan and it uses the KamLAND (Kamioka Liquid scintillator AntiNeutrino Detector) facility. It is placed nearly 1 km underground because of the needed screening of the cosmic rays, which contribution is predominant at sea level.
The main components of the detector are: a steel tank containing a very pure liquid scintillator (LS), made of mineral oil, benzene and other fluorescent chemicals; at the heart of it, is placed an inner balloon made of a very thin casing of transparent nylon and filled with enriched Xenon dissolved in a decane ($C_{10}H_{22}$) based LS. The scintillation photons produced by the electrons coming from the $0\nu\beta\beta$ decay are observed by a grid of PMTs placed around the steel tank. Outside of it there is water acting as a Cherenkov detector for muon identification, that also acts as a radiation shield from the surrounding rock.
This experimental setup has the pros to be relatively low costed, to be capable of doing observations in other physical fields in parallel to the main one and it can easily scale up its statistics, proportional to the quality of its results, for example via the addition of Xe in the inner balloon or by improving the radioactive purification of the environment. In Figure 1.8 is shown a scheme of the KamLAND-Zen experiment [38].

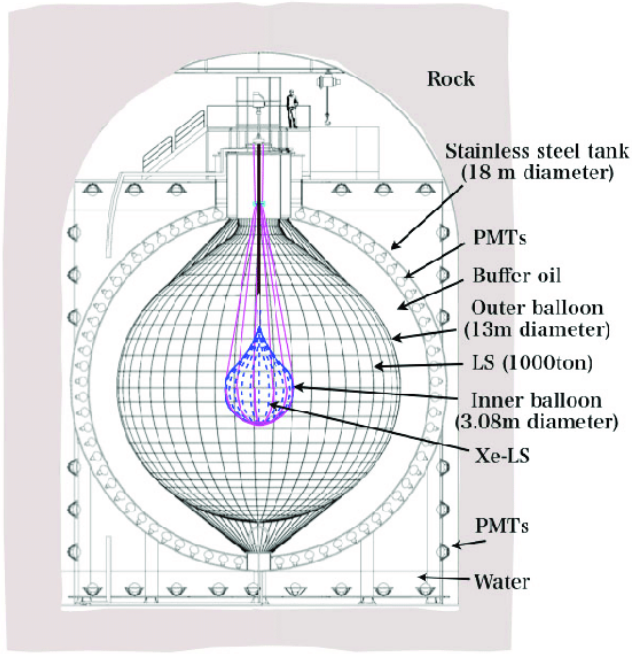

Figure 1.8: The KamLAND-Zen detector, placed at the KamLAND facility. A figure of a man is placed on the top to better understand the dimensions of the apparatus.

The first phase of data acquisition, using 320 kg of enriched Xe, was strongly influenced by the ^{110m}Ag β^- decay ($Q = 3.01$ MeV). The presence of the decay of this Ag metastable state and also other contamination coming from the ^{238}U chain were considered to be caused by the 2011 Fukushima nuclear accident, that happened when the main part of the reactor was being built in a University $\sim$ 120 km from the location of the nuclear reactor.
After the first phase, a purification campaign started in which the inner balloon and the Xe sample were purified via different procedures.
The phase-II started with an increased enriched Xe sample (380 kg) and a decrease of order 10 was observed in the ^{110m}Ag contamination. Other types of background processes were present.
Very recent results from the KamLAND-Zen collaboration exploited a very high exposure, namely 970 kg·yr, allowed them to set a lower limit on the ^{136}Xe $0\nu\beta\beta$ decay half life of $T^{0\nu}_{1/2} > 2.3 \times 10^{26}$ yr at a 90% CL. From this limit they also obtained the corresponding upper limit on the effective Majorana mass as $m_{\beta\beta} < (36 - 156)$ meV, using improved phase space factor and nuclear matrix elements calculations [39]. Figure 1.9 reports the energy spectra in the central region with the experimental data and the models for the background processes together with the limit on ^{136}Xe $0\nu\beta\beta$ decay events.

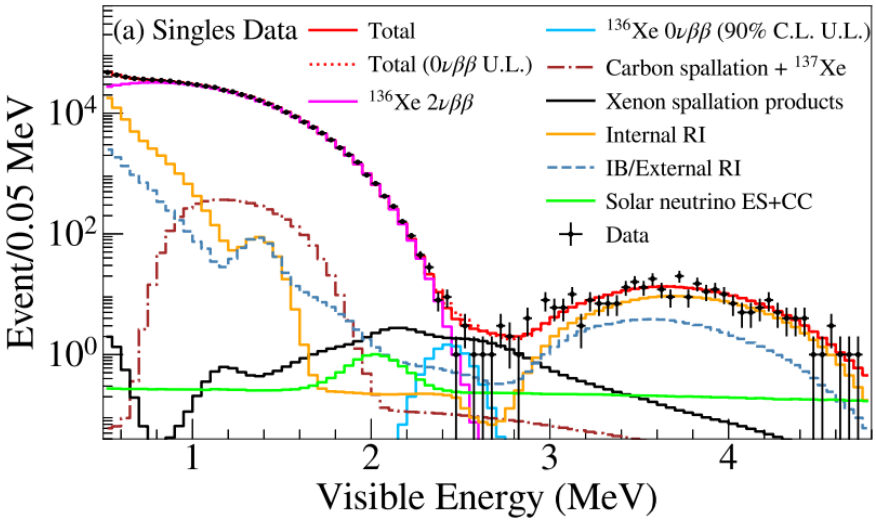

Figure 1.9: Energy spectra of the events in the inner part of the detector. Notice the limit on the ^{136}Xe $0\nu\beta\beta$ decay events in light blue, together with the best-fit for various background contributions. Plot courtesy of [39].

In the future the KamLAND2-Zen experiment plan to achieve a sensitivity on the effective Majorana mass that would cover the whole IO region and the branch point of the NO/IO mass spectrum, targeting a value for the $m_{\beta\beta}$ of around 20 meV with the need for better background discrimination techniques and improved energy resolution at $Q_{\beta\beta}$[40].

Chapter 2

The CUORE Experiment

2.1 Introduction

The Cryogenic Underground Observatory for Rare Events (CUORE) is an experiment designed to search for the neutrinoless double beta decay of ^{130}Te using TeO_2 crystals. It is located at the LNGS in Italy and it is the first ton-scale bolometric detector that looks for this very rare decay. It started its operation in 2017, after many years of research and tests with its predecessors CUORICINO [41] and CUORE-0 [42], and it is expected to perform data taking until reaching a total exposure of 3 ton·yr [43].
The CUORE detector is composed of 19 towers of 988 TeO_2 crystals working as bolometers at cryogenic temperatures ($\sim$ 10 mK). The total mass of TeO_2 is 742 kg which corresponds to 206 kg of active isotope (^{130}Te). The cryogenic conditions allow the crystals to detect particles thanks to the rise of temperature induced by their energy deposit. In CUORE the emitting source and the detector are the same since the crystals contains the active isotope and operate as particle detectors.
The CUORE main goal is to reach a discovery sensitivity of 4×10^{25} years on the ^{130}Te $0\nu\beta\beta$ decay half life. This goal can be achieved with a BI of 10^{-2} counts/(keV·kg·yr) and at an energy resolution of 5 keV in the ROI, which is around the $Q_{\beta\beta} = 2527$ keV [44].
As well as other $0\nu\beta\beta$ decay experiments (see Section 1.4.2), CUORE aims to reconstruct the energy spectrum of the double beta emitter and try to distinguish an event excess in the ROI. CUORE chose ^{130}Te as the candidate isotope mainly because of its high isotopic abundance, already shown in Table 1.2, that allows to grow the TeO_2 crystals without the need of an enrichment procedure. Moreover the $Q_{\beta\beta}$ of the reaction is above most of the relevant radioactive γ background but still below the 2615 keV end-point.
The background suppression is another key point of rare event searches like CUORE. To achieve this various shields are used in the experiment, like lead shield for γ rays and polyethylene ones for neutron induced background; together with the natural shield

which is the Gran Sasso mountain.

In this chapter I will discuss the design of CUORE, starting from the external part of the detector, and how the search for $0\nu\beta\beta$ decay is performed.

2.2 Experimental Setup

2.2.1 LNGS Underground Site

To reduce the ubiquitous background coming from cosmic rays, experiments looking for very rare processes must be located underground. The CUORE experiment has been built in Hall A of the LNGS, an INFN underground facility located in central Italy (Assergi, AQ).
The site is below the Gran Sasso mountain and it is shielded by 1400 m of rock (equivalent to 3600 m of water). This shield allows a reduction of the cosmic rays flux by 6 orders of magnitude with respect to the surface flux, thus reducing the possible background induced by these external particles [45].
Figure 2.1 shows a sketch of the LNGS underground laboratories.

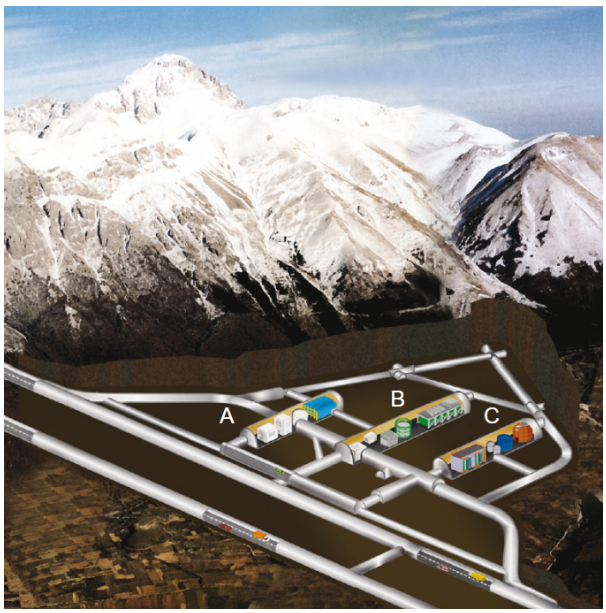

Figure 2.1: Sketch of the LNGS laboratories below the Gran Sasso mountain. The hall names are shown in the figure. The only way to access the underground site is by car through the highway tunnel that passes below the mountain.

2.2.2 TeO_2 Bolometric Detectors

In CUORE the TeO_2 bolometric detectors measure energy deposits by measuring a temperature increase ΔT in the TeO_2 absorber that is induced by the energy deposited by the particle. The cryogenic temperature is needed for the correct functioning of the bolometers and so that the detector will be sensible to small temperature increases.
The main advantage of bolometric techniques is the excellent energy resolution of 0.2-0.3%. However one has to take into account the technological challenge of cooling a very large mass to milliKelvin temperatures and maintaining this conditions for the entire duration of the experiment.

Cryogenic temperature calorimetry using crystals made with active $\beta\beta$ emitting isotopes was already developed in the early 1980s [46]. This early researches activities already highlighted TeO_2 crystals as suitable candidates for the search of ^{130}Te $0\nu\beta\beta$ decay in cryogenic conditions because of their thermodynamic and optical properties, as well as their commercial availability [47]:

- Tellurium dioxide (TeO_2) can easily be produced on a large scale.
- The established production techniques together with very low natural contamination allow the crystals to also have a very good radio-purity.
- TeO_2 is both dielectric and diamagnetic. At low temperatures its heat capacity C is described by the Debye law

$$C(T) \propto \left(\frac{T}{T_D}\right)^3 , \tag{2.1}$$

  where $T_D = 232$ K is the Debye temperature of the material, which can be obtained experimentally [48]. Since T_D is much greater than T, the heat capacity C is very low giving rise to a large temperature difference ΔT when some energy deposition occurs. In fact, the energy deposition is given by the formula:

$$\Delta T = \frac{E}{C(T)} . \tag{2.2}$$

  Therefore, the small heat capacitance yields an excellent energy resolution.
- Furthermore, the thermal expansion coefficient of TeO_2 crystals is close to the copper (Cu) one [49], making copper suitable for the construction of the detector support structure.

CUORE employs 988 TeO_2 cubic crystals of 5 cm per side. Each crystal weighs in average 750 grams, which corresponds to 208 g of ^{130}Te per unit. A picture of a CUORE crystal is shown in Figure 2.2.

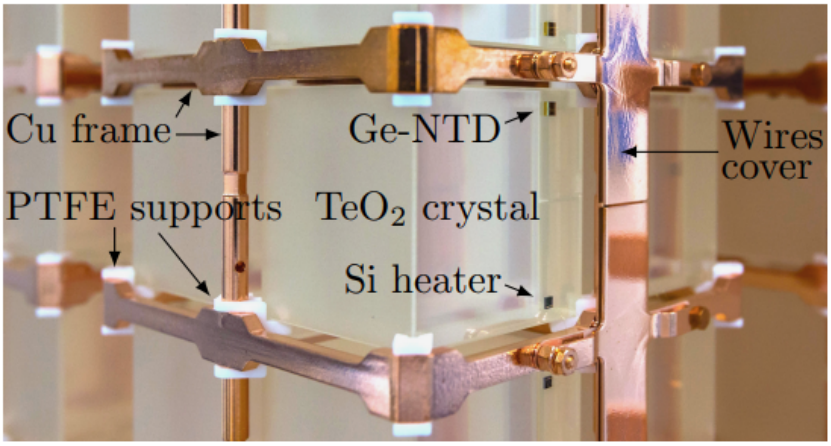

Figure 2.2: Closer look at a CUORE TeO_2 crystal, figure courtesy of [50].

The sensor used to measure temperature variation is a Neutron Transmutation Doped Germanium (NTD-Ge) thermistor which works as a voltage transducer. This thermistors converts the thermal signal produced by the deposited energy in the absorber into a voltage pulse, that is read out by the data acquisition system.
This kind of thermistors were chosen for CUORE because they have a wide temperature range of work, their readout technology is simple and their response is quite stable with respect to temperature variations. On the other hand they have a slow response, of the order of tens of ms, so they can not sustain high rates of events. However $0\nu\beta\beta$ decay experiments aim to have very low background rates and so the NTD-Ge are appropriate for rare event searches.
The NTD sensor is glued to the crystal using 9 spots of epoxy glue. Laying the glue in spots and not in a uniform way, will deliver a better thermal coupling and a lower risk of crystal fractures during the cooling procedure. The spots have a 0.5 mm diameter and a 50 μm thickness, they are all posed by a mechanical arm so that they will be always in the same position and with the same spacing for all the single detector units. This to guarantee the uniformity between all detectors [51].
For future bolometric experiments, like the CUORE update CUPID (CUORE Update with Particle Identification), this thermistor technology can be improved and research and development around this topic is currently ongoing [52].

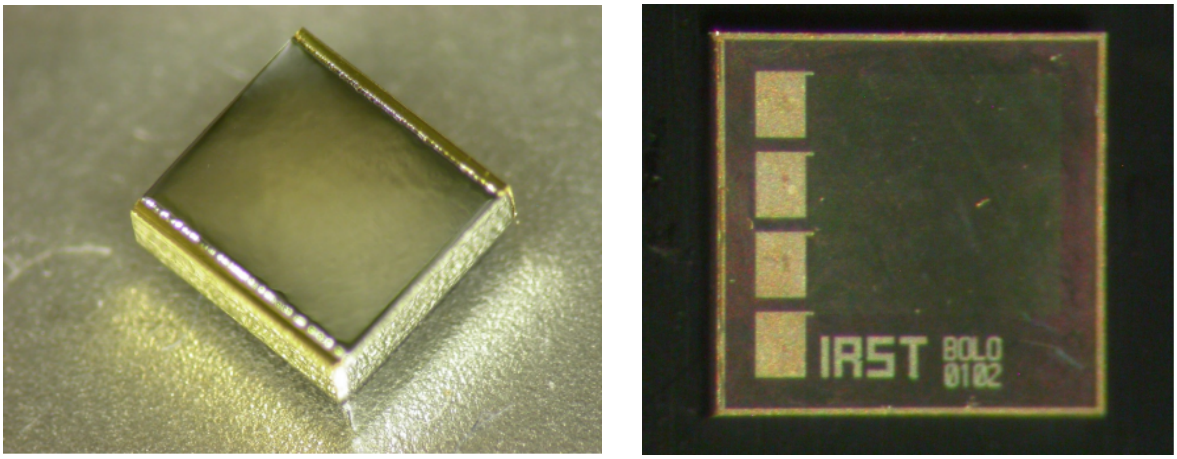

Figure 2.3: On the left a picture of a CUORE NTD-Ge thermistor. While on the right a picture of a CUORE silicon heater chip. Pictures taken from [51].

In addition to the NTD, each crystal is equipped with a silicon joule heater, see Figure 2.3 (right), consisting of a strongly doped Si semiconductor with a resistance of 300 kΩ. They are designed to periodically deliver a precise amount of heat to the detector for gain stabilization meanings. As well as the NTD thermistors, the Si heaters are glued to each unit using mechanically placed epoxy glue.
Each crystal is supported at its vertices by 8 PoliTetraFluoroEthilene (PTFE) holders mounted on a copper support structure. The PTFE holders act as thermal link to the copper heat bath. The copper used by CUORE is of type NOSV, chosen because of its low radioactivity component and absence of hydrogen, which makes it suitable for cryogenic operation. Figure 2.4 (left) shows the entire CUORE detector setup.

2.2.3 CUORE Cryostat System

The sensitivity of CUORE detectors to energy deposition depends on the temperature of the heat bath (see Eq. 2.2) and a very low T is needed to have a higher Signal to Noise Ratio (SNR). The CUORE cryostat system has been designed to fulfill the need to have the experiment operating at cryogenic temperatures, around 10 mK, in a stable way for 5 years. The cryogenic cooling system consists of three main parts: the Fast Cooling System (FCS), the Pulse Tube cryocoolers (PTs) and the He Dilution Unit (DU) [53].

Figure 2.4 (right) shows a schematic view of the CUORE cryostat system. The CUORE cryostat is a multi stage system made of six nested Cu vessels with six different temperatures, decreasing going deeper towards the detector. Their temperatures are (see Figure 2.4 right): 300 K, 40 K, 4 K, 800 mK, 50 mK and 10 mK. From now on, every vessel will be indicated by its temperature. The 300 K and 4 K vessels define two vacuum volumes,

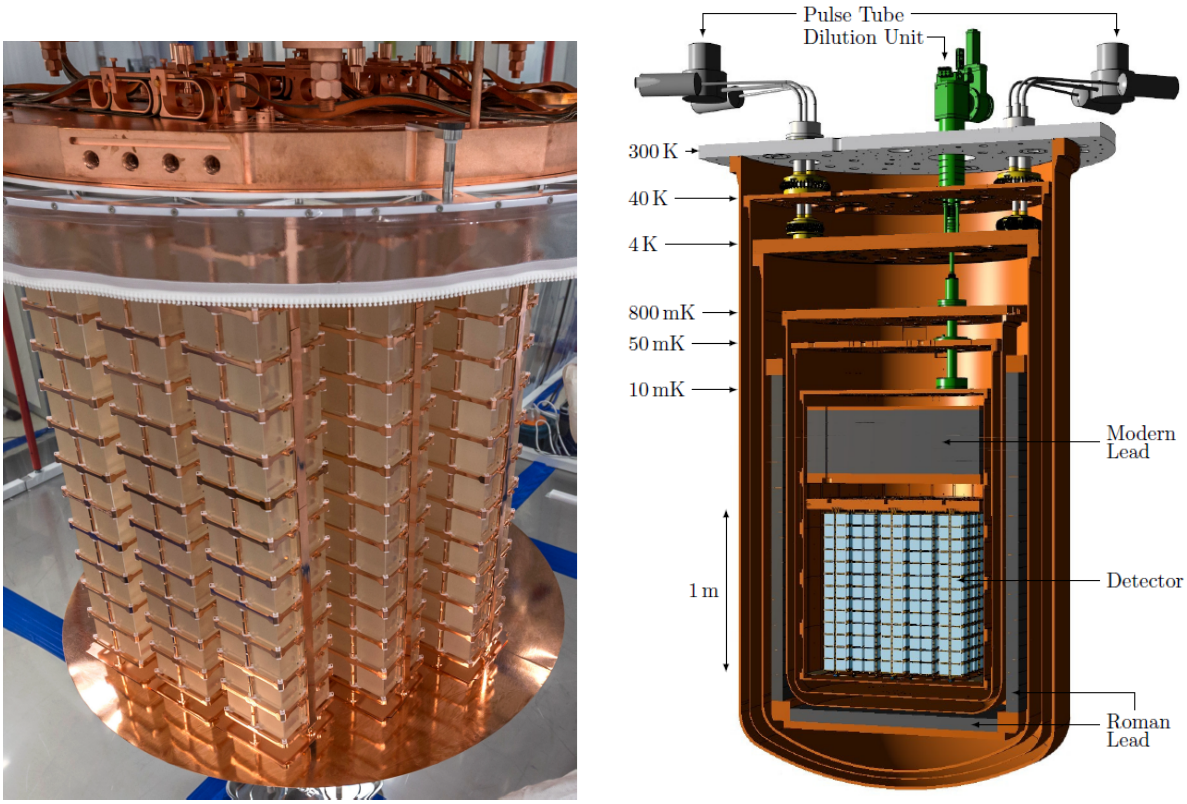

Figure 2.4: Picture of the CUORE towers (left) after the installation of all components. Rendering of the CUORE cryostat (right). The different stages are labeled with their temperatures. The lead shields are also highlighted in this picture. The CUORE detectors in the internal stage is said to be the coldest cubic meter of the known Universe. Pictures taken from [50].

the Outer and Inner Vacuum Chambers (OVC and IVC), and are kept at pressures of the order of 10^{-6} and 10^{-8} mbar respectively. The choice of the vessel material was very important because its possible contamination would impact the CUORE background. Vessels and plates, beside the 300 K upper plate, are made of very high purity copper. Two types of Cu were used:

- the 10 mK vessel is made of the same type of copper as the detector Cu frame (NOSV-Cu) which, together with the low radioactive component, needs to have a low hydrogen content. This is needed because at $\sim$ mK temperatures H_2 molecules can slowly convert from ortho to para H_2 causing heat leaks that will impact the detector stability [54];
- the other vessels are made of a different type of copper called Oxygen-Free Electrolytic (OFE) Cu, which has a purity of 99.99%.

The main radioactive components of the Cu vessels, and also the inner frame, comes from Th and U bulk contamination. Therefore, a systematic campaign of material selection has been performed to select the copper with the highest radiopurity.

Fast Cooling System and Pulse Tubes

The CUORE cooling procedure is divided in stages. The first one has the goal to cool the whole system to a temperature around 30-40 K. This first cooling is initially performed by the FCS [53] [55] thanks to a flow of a cold ^{4}He gas pumped through the IVC volume using PTFE tubes and then extracted from the inner vacuum chamber. The helium gas allows the IVC to reach a temperature of 200 K, then at this point the PTs are turned on and drive the temperature to the needed 30-40 K; then only the PTs stay on for subsequent cooling phases.
PTs will then take over for the second cooling phase. A PTs cryocooler uses ^{4}He gas in a closed circuit to cool down the IVC, exploiting its iso-enthalpic expansions. These expansions are obtained by varying the pressure inside the circuit, which is connected to the 4 K vessel. The pressure varies periodically thanks to a room temperature valve that connects the PTs to an external compressor.
The nominal values of the cooling power of the PTs, found in [53], lead to a minimum of three PTs needed to reach the 4 K temperature during the second cooling phase. However the CUORE experiments mounts five of them, for redundancy.
The main advantages of a gaseous cooling system, commonly referred as "dry", with respect to a system based on liquid helium (referred to as "wet"), are the higher duty cycle granted by the absence of frequent refills, and the reduced operation cost provided by the negligible losses of ^{4}He. A disadvantage encountered with the PTs system are the possible vibrations due to pressure variation in the tubes that might be induced

to the cryostat. Extensive work has been put into minimizing this noise contribution [56].

Dilution Unit

The last phase of the cooling procedure is driven by the DU and allows the detector to reach $\sim$ 10 mK working temperature. The DU is filled with a ^{3}He-^{4}He mixture (17%-83%) cooled at around 4 K by the PTs in an initially homogeneous state. The mixture is then pumped along the DU by a room temperature pump. Below 0.87 K (see Figure 2.5 left) the mixture separates in two distinct phases: one ^{4}He Bose liquid with a low ^{3}He concentration (^{3}He dilute phase) and an almost pure ^{3}He Fermi liquid (^{3}He concentrate phase). The two phases have different densities and so they remain separated inside the DU. The enthalpy of the ^{3}He dilute phase is higher than the ^{3}He concentrate one so ^{3}He atoms will move from the concentrate phase to the dilute one in order to reach equilibrium. This reaction is endothermic and subtract energy from the cryostat environment, generating the cooling power of the DU [57].
To achieve the continuous cooling required by CUORE, the ^{3}He dilute phase is kept out of equilibrium by extracting ^{3}He atoms and injecting them back in the DU. The CUORE DU consists of two lines containing the ^{3}He-^{4}He mixture; this allows the DU to continue its operation even if one of the two lines fails.

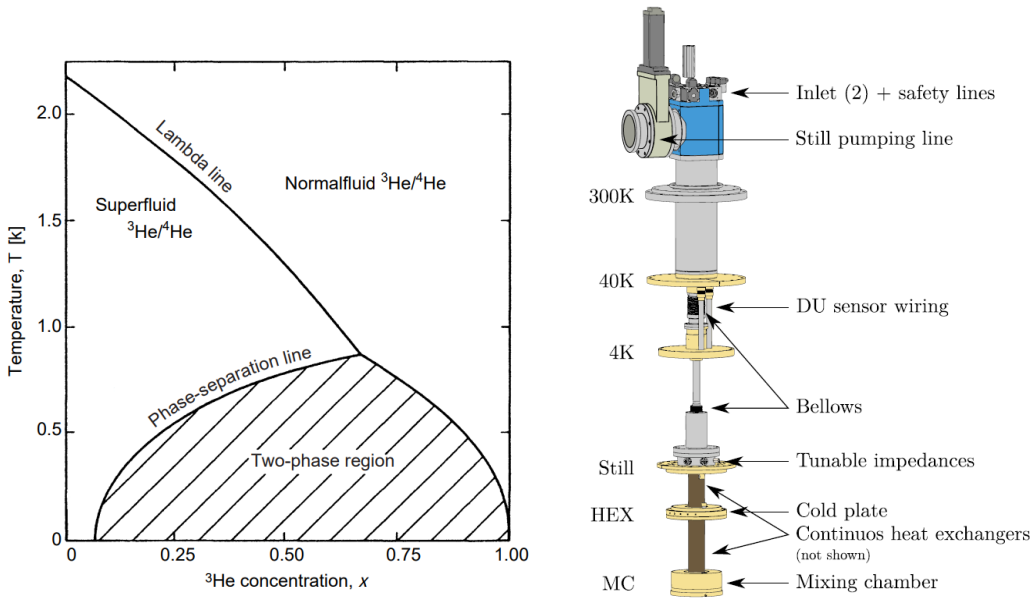

Figure 2.5: ^{3}He-^{4}He mixture phase space (left) [57] and rendering of CUORE Dilution Unit (right) [53]. The Still, HEX and Mixing chamber are connected to the 800, 50 and 10 mK vessels respectively.

Lead Shields

Another very important part of the CUORE experiment are the lead shields placed inside the cryostat (see Figure 2.4 right). Their goal is to shield the detector crystals from external radioactivity and from the radioactive contamination coming from the other cryostat elements.
The Modern Lead Shield (MLS) is a 30 cm thick lead disk placed above the detector towers, made of ~ 2 tons of modern lead and is maintained at a temperature of 50 mK. It mainly shields the crystals from the radioactivity coming from the cryostat components. The Roman Lead Shield (RLS) is a thinner layer of lead placed around and on the bottom of the detector. It weighs roughly 5 tons and it is thermalized to the 4 K plate. This lead is dated I century B.C. and was obtained from ingots found on a Roman shipwreck near Sardinia (Italy) coast; it was chosen for the CUORE shield structure because of its very low radioactivity since it has been below sea water for more than 21 centuries, also protecting it from cosmic rays. Measurements have been performed on the RLS radioactive contamination obtaining an upper bound on the specific activity of 715 μBq/kg [58] which is way less than the one of modern lead [59].

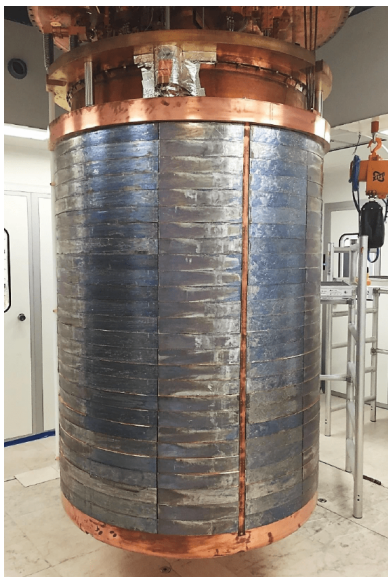

Figure 2.6: Picture of the recovery of the roman lead (left) [57] and of the CUORE RLS (right). The final installation of the shield is 6 cm thick, with a radius of 64 cm and height of 178 cm.

2.2.4 CUORE Auxiliary System

The CUORE auxiliary system consists of all the experiment components outside the cryostat whose main goals are to mechanically support the experiment and reduce the

possible noise induced on the detectors, such as the vibrations caused by the cooling system, earthquakes or human activity in the laboratories. Figure 2.7 reports a rendering of the whole CUORE support system. The red structure is called Main Support Plate (MSP) to which the cryostat is secured. The MSP stands on four 4.25 m tall columns filled with sand held by a concrete structure. At the base of the latter are placed four seismic insulators that aims to isolate the experiment from the earthquakes vibrations.

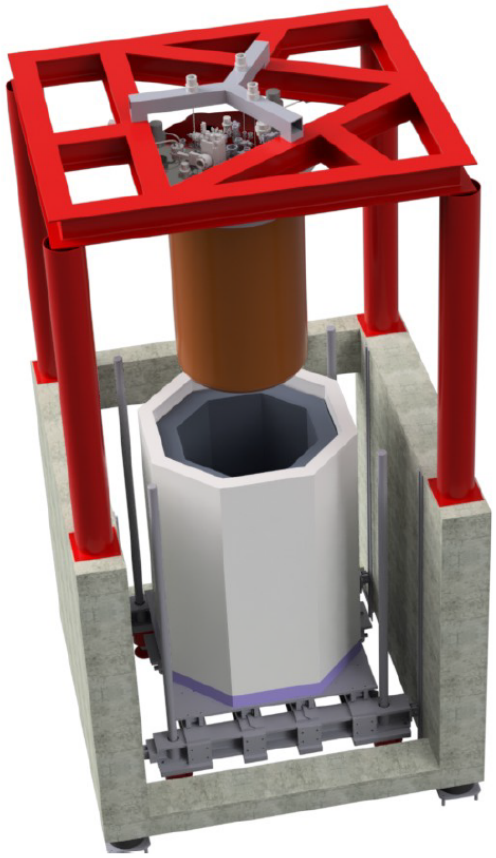

Figure 2.7: Rendering of the CUORE auxiliary system. The upper structure in red is the MSP, the orange cylinder is the cryostat , the dark grey octagon is the ELS and in white the polyethylene panels.

To further reduce the noises on the crystals, the detector is not directly connected to the MSP but it is held in place by a Y-shaped structure called Y-beam placed above the MSP (in grey in Figure 2.7) and mechanically isolated from it by means of three insulators (Minus-K insulation system) which are devices built with a precise spring scheme that allow to tolerate heavy loads while reducing the possible noises induced on the cryostat. The CUORE detector is connected to the Y-beam thanks to three vertical

Detector Suspensions (DS) wires that pass through all temperature and pressure stages of the cryostat. The DS have to be built with pure materials and by taking into account the difficult cryostat conditions, while reducing the vibrations coming from the Y-beam. The last part of the auxiliary system is the External Lead Shield (ELS), it is a 25 cm thick and ~ 70 tons modern lead shield that will additionally screen the CUORE crystals from γ rays coming from the environment. The ELS is covered by polyethylene panels (in white in Figure 2.7) that aims to thermalize and capture neutrons mainly caused by cosmic rays interactions and radioactive decays. This shield component is usually placed below the cryostat and it is raised up only during the data taking periods.

2.3 Bolometric Technique

Bolometric detectors convert the deposited energy in the crystals into thermal phonons and measure it as a temperature variation. The two main parts of a bolometer are the absorber (TeO_2 crystal), where the energy is deposited, and the temperature sensor (NTD thermistor). Figure 2.8 shows a simplified thermal model of a CUORE bolometer.

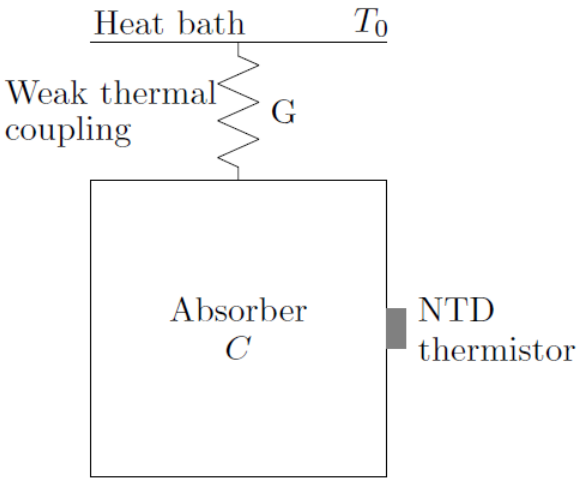

Figure 2.8: Simplified bolometer scheme. The detector can be considered as the crystal with heat capacity C, coupled with a T_0 copper thermal bath through a conductance G. Figure from [50].

2.3.1 Energy Absorber

The TeO_2 energy absorber has a heat capacity C and it is coupled with a thermal bath, at a constant temperature T_0, through a thermal conductance G. A particle releasing an

energy E will induce a temperature increase

$$\Delta T = \frac{E}{C} \ . \tag{2.3}$$

Then the produced heat will flow to the heat bath until the absorber returns at its initial temperature. Two assumptions have to made, i.e. that $\Delta T(t) = |T(t) - T_0|$ is much smaller than the temperature of the bath T_0, where $T(t)$ is the temperature of the absorber, and that C and G are constant in time.
The time evolution of the signal (see Figure 2.9) can be approximated as a single exponential decay

$$\Delta T(t) = \frac{E}{C} \cdot e^{-\frac{t}{\tau}} \ , \tag{2.4}$$

where $\tau = C/G$ is the decay time.

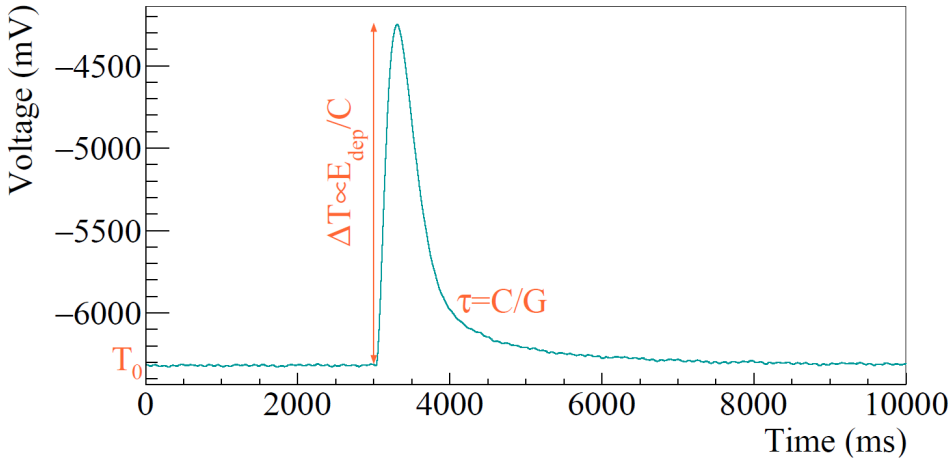

Figure 2.9: Example of a CUORE signal. The amplitude depends on ΔT, the decay time τ on the ratio C/G and the baseline level is T_0. Plot from [50].

Eq. 2.4 shows that to have a high ΔT and so a detectable signal the heat capacity needs to be as small as possible. For the CUORE crystals C follows the Debye law (see Eq. 2.1), so C depends on the temperature of the detector. This, together with the need to have a very low thermal noise, explains the need to run the experiment at cryogenic temperatures. For CUORE crystals C is typically around 10^{-9} J/K at $T_0 = 10$ mK then the temperature rise for a 1 MeV deposited energy is close to 100 μK, which is still very low but detectable by the NTD thermistor.

The energy deposited in the absorber is converted to thermal phonons, which are vibrational excitations of the lattice. A detailed description of phonon production and interaction can be found in [60] and [61]. In a simplified way phonons are produced when a particle interact with the nuclei or the electrons of the absorber:

- in the first case the interaction of particles with the lattice nuclei causes vibrational excitations;
- while when a particle interacts with the electrons of the crystal an electron-hole pair is created and phonons are produced by the interaction of these pairs.

The production of phonons imply possible fluctuations in the detected energy; one can estimate the intrinsic energy resolution of a bolometer by means of simple considerations [62]. The number of phonon modes at equilibrium can be written as

$$N = \frac{C(T)}{k_B} \ , \tag{2.5}$$

where $C(T)$ is the usual heat capacity and k_B is the Boltzmann constant. While their mean energy is

$$\varepsilon = k_B T \ . \tag{2.6}$$

The intrinsic energy fluctuations will depend on this two quantities as

$$\Delta E = \varepsilon \cdot \sqrt{N} = \sqrt{k_B \cdot T^2 \cdot C(T)} \ , \tag{2.7}$$

since the number of phonons follows the Poisson statistic. Using typical values of the CUORE bolometers and considering the right unit conversion, one get a prediction of the energy uncertainty of around 10 eV which is orders of magnitude smaller than the CUORE energy resolution at $Q_{\beta\beta}$, since it is dominated by thermal[1] and vibrational noise.

2.3.2 Temperature Sensor

Phonons produced by particles interacting in the crystals can be considered as coherent vibrations of the lattice that after a short period of time become incoherent vibrations of single atoms which are the heat that will cause the temperature increase in the detectors. The sensors used in bolometric experiments convert temperature variations into an electric signal. To achieve this, CUORE uses NTD-Ge thermistors. They are semiconducting Ge chips doped with thermal neutrons; the electric signal is obtained by a resistance variation in the thermistor. They are slow sensors, however they were chosen for the CUORE experiment because they are sensitive to phonon-caused temperature increases, can be operated in a wide range of temperatures and have a simple readout circuit [63].

Semiconductors at room temperature behave as insulators because the energy gap between the full valence band and the empty conduction band is 0.67 eV for Ge, while the

[1] The thermal noise is generated by the heat exchange between the TeO_2 crystals and the heat bath.

average electron thermal energy is $k_B T \sim 0.025$ eV. So conduction is possible only at higher temperatures. Thanks to the impurities added to the Ge lattice, new energy levels are added that will reduce the gap between the valence and conduction bands allowing conduction also at lower temperatures.
At $T < 10$ K the conduction is driven by the migration of the charge carriers between the impurities sites. Conduction happens when electrons move from a donor site to another, without using the conduction band; this is possible thanks to the quantum tunneling throughout the potential wall that separates the donor sites. This is called hopping conduction mechanism [64], in Figure 2.10 (left) displays a simple scheme of this conduction mechanism.

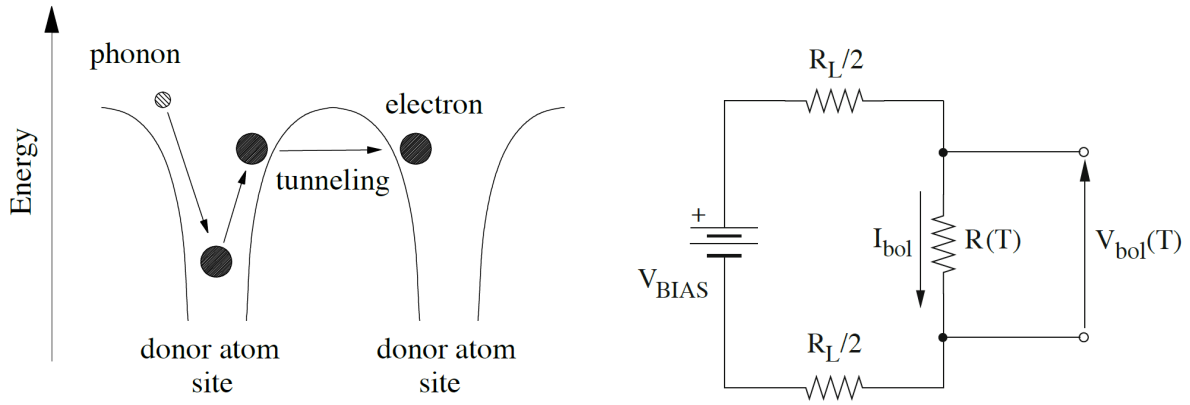

Figure 2.10: Scheme of the hopping mechanism (left) and bias circuit for NTD-Ge thermistor readout (right). $R(T)$ is the varying resistance that will induce a voltage pulse.

The CUORE NTDs are obtained by bombarding Ge wafers with thermal neutrons to create the required impurity level. The thermistor resistance depends on the absorber temperature as

$$R(T) = R_0 e^{\gamma \frac{T_0}{T}} \ , \tag{2.8}$$

where R_0 depends on the sensor geometry and is about 1 Ω, $T_0 \sim 3$ K and $\gamma = 0.5$. These three parameters are all obtained experimentally [65].
When energy is released in the absorber, the temperature increases and, from Eq. 2.8, $R(T)$ decreases. This variation in the thermistor resistance can be measured if the NTD is connected to a bias circuit (see Figure 2.10 right) characterized by a load resistor R_L, V_{BIAS} the bias voltage and the varying voltage on the NTD-Ge thermistor $V_{bol}(T)$ can be obtained as

$$V_{bol}(T) = I_{bol} \cdot R(T) = \frac{V_{BIAS}}{R_L} \cdot R(T) \ , \tag{2.9}$$

if the load resistance is much greater than the bolometer one [66].
The linearity between V_{bol} and I_{bol} is lost if the power dissipated by the current is considered, this dissipation causes the thermistor to heat up and decrease its resistance.

The new non-linear relation between V_{bol} and I_{bol} allow to build the Load Curve, see Figure 2.11 for an example, which allow to choose the so-called Working Point of the bolometer that, in static conditions (no interactions in the absorber), defines the V_{BIAS}. This procedure needs to be performed for each bolometer separately.

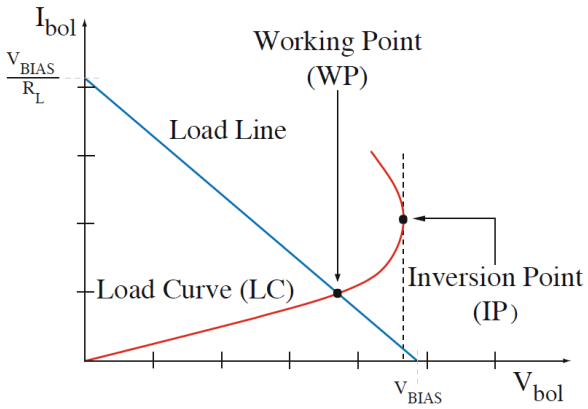

Figure 2.11: Example of load curve of a NTD-Ge thermistor.

Chapter 3

CUORE Data Acquisition and Processing

This chapter describes the CUORE data processing, which consists of the acquisition of a continuous data stream for each detector, and its processing for the reconstruction of physical events.

3.1 Read-Out Chain

The CUORE Read-Out Chain (ROC) consists of three components, located at room temperature above the cryostat: the front-end electronics, the digitizers, and the pulser boards. A scheme of the read-out chain is given in Figure 3.1. The Front-End (FE) electronics was customly developed for the CUORE experiment and consists of 180 boards reading 6 channels each [66]. The FE system provides the bias voltage to the NTD of each bolometer and also acts as a dual stage amplifier for the voltage signals, namely the digital preamplifier and the Programmable Gain Amplifiers (PGA) in Figure 3.1. All the parameters of the FE electronics, like V_{BIAS}, R_L and the gains, can be controlled independently for each channel.
The signal is then sent to the Bessel board, which acts as antialiasing filters. Each board controls 12 channels. The filter is an active six-pole Bessel-Thompson filter whose main feature is the preservation of the pulse shape while avoiding possible deformation of the signals [67].
The data digitization is performed by 64 digitizer modules that receive the output of the Bessel filter. The digitizers have a noise corresponding to an energy resolution of $\sim$ 150 eV, which is negligible if compared to the resolution of the CUORE bolometers, and a sampling frequency of 1 kHz to fully preserve the timing information of the signals. The DAQ consists of seven computers placed in the CUORE control room, above the cryostat: six of them perform an online trigger of the data streams from the 988

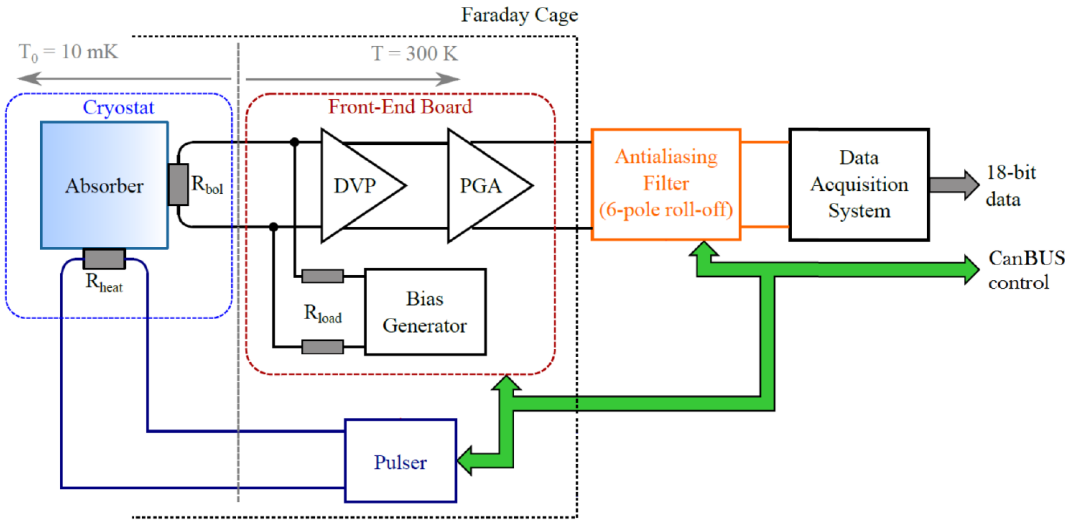

Figure 3.1: Scheme of the CUORE Read-Out Chain. The DVP and PGA are the two amplifier stages while the CanBUS control system allow the Data AQuisition (DAQ) system to manage the pulser and filter boards. Scheme adapted from [51].

channels, while one computer controls all the digitizers and writes the data to disk. The data is divided into Raw and Continuous data. The latter consist of files containing the continuous waveforms while the former contain the triggered data [68] [69].
Lastly the pulser boards are used to send very short and precise voltage pulses to the silicon heater chips. This will simulate the energy release in the crystal by the interaction of a particle. The heater signals are used to study the temperature dependence of the signal amplitude, and correct for it [70].

Data Triggering

The events can be divided in three categories

- physics events consist of particles interacting with the crystals and releasing energy;
- heat pulse events, one in each channel every $\sim$ 6 minutes;
- noise events.

CUORE uses two types of triggers to detect the signal events in the detectors. The DAQ computers run a Derivative Trigger (DT), which fires when the derivative of the waveform is higher than a previously set threshold. The DT is characterized by a threshold of 50-100 keV, depending on the channel. Additionally a dead time of 1 second is placed after the trigger to avoid multiple events to be triggered too closely (pile-up events).
A more advanced trigger algorithm, called Optimum Trigger (OT), is run offline at a

later time. The OT uses a filtered waveform (the so-called optimum filter) to suppress the noise and exploit the information from the full signal waveform, and allows to lower the threshold well below 10 keV [71].

Data Collection and Storage

The CUORE data are structured in runs of about one day, and grouped in datasets with a duration ranging from few weeks to two months. Before and after each dataset there are calibration runs.

3.2 Data Production and Analysis

The data production is done via the DIANA software, based on C++ and ROOT, developed by the CUORE collaboration. This software takes the triggered events and applies to them different procedures in a specific order. The DIANA workflow includes the reconstruction of event-related quantities such as the baseline or amplitude, the gain stabilization and energy calibration, the quality cuts and the reconstruction of multi-channel quantities such as the event multiplicity.

Bad Intervals

Prior to the signal processing, the periods affected by sub-optimal detector performance (so-called *bad intervals*) are identified and removed from the data stream. The *bad intervals* can be caused by a variety of reasons, including maintenance operations, earthquakes, or the malfunctioning of some cryogenic or electronic component [72].

Preprocessing

The first part of the event processing, denoted as preprocessing, starts with the analysis of the first 3 s (pre-trigger) of the event for baseline parameters evaluation. To obtain the average baseline and its slope a fit with a straight line is done in a part of the pre-trigger interval. Moreover the baseline noise is computed as the Root Mean Square (RMS) of the data in that time interval. At this point, the signal is differentiated and the number of pulses is computed as the number of times the derivative is higher than a given threshold.
Figure 3.2 shows two waveforms with 3 and 2 physical events, respectively. In the first case, all events are correctly triggered, while in the second case only one pulse is identified.

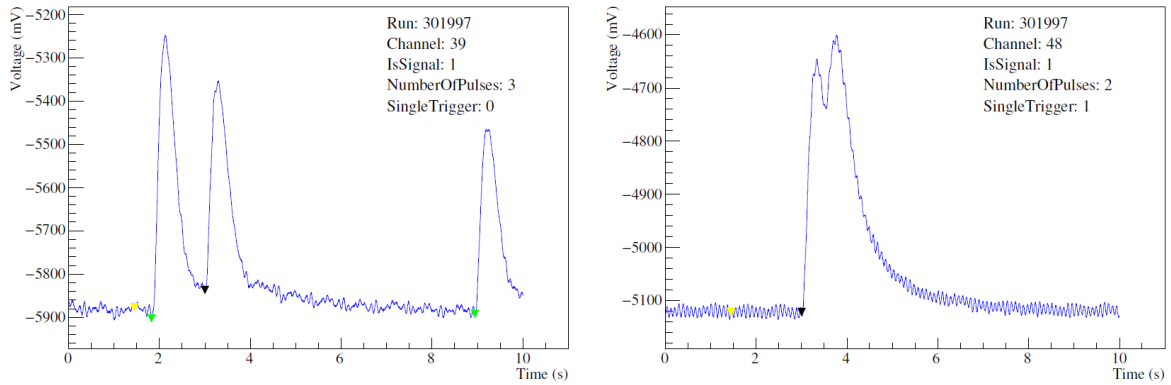

Figure 3.2: Example of two CUORE events with multiple pulses. On the left 3 pulses are found by the online DT and triggers are assigned to each event, while on the right the offline analysis found 2 close pulses but only one trigger time is assigned to it because the second pulse is not identified by the DT, due to its dead time [73].

Amplitude Evaluation

The amplitude of the events is evaluated via a time-modeled waveform defined as

$$v(t) = \overline{A} \cdot s(t) + n(t) + b \ , \tag{3.1}$$

where $\overline{A}$ is the amplitude of the pulse, $s(t)$ the signal response function, $n(t)$ the time-dependent noise and b is the baseline. $\overline{A}$ can be decomposed in two terms as

$$\overline{A} = G(T) \cdot A(E) \ , \tag{3.2}$$

the first being the bolometer gain depending on the thermistor temperature while $A(E)$ is the real amplitude of the signal and depends on the energy deposited in the crystal. The signal response $s(t)$ is determined using signals: heater ones and pulses at the ^{208}Tl 2615 keV γ-peak; averaging this pulses allow to have a measurement of $s(t)$ with reduced noise [74]. The so-called Optimum Filter (OF) [71] is then built using the power spectrum of the Average Pulse (AP) and of the Average Noise Power Spectrum (ANPS) obtained from randomly triggered noise events.
An important feature of the OF is that it will estimate the amplitude by leveraging the whole waveform and not only some points around the peak. In frequency space a filtered pulse can be written as

$$V^{OF}(\omega) = \mathcal{G} e^{i\omega t_M} \frac{S^*(\omega)}{N(\omega)} V_i(\omega) \ , \tag{3.3}$$

where $\mathcal{G}$ is a factor accounting for the gain, t_M is the time at which the signal reaches the maximum, while $S(\omega)$, $V(\omega)$ and $N(\omega)$ are the Fourier transform of the respective quantities of Eq. 3.1 and are the power spectra of the AP, the ANPS, and the power

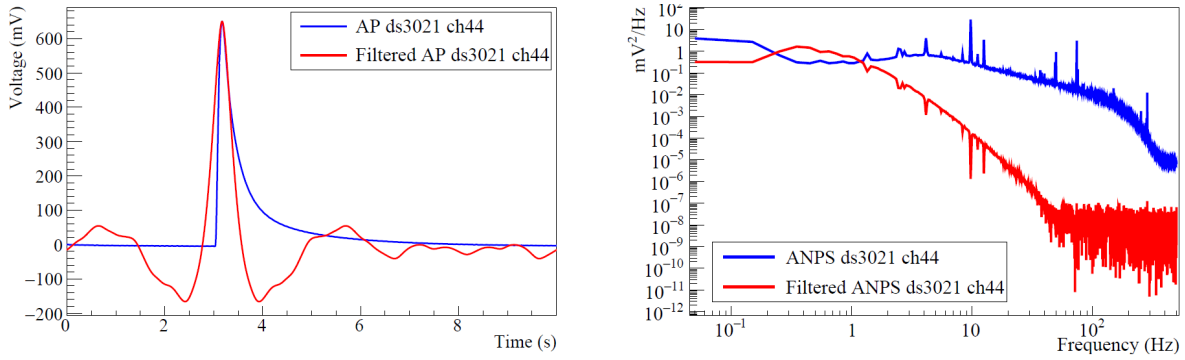

Figure 3.3: Example of the AP (left) and ANPS (right) before and after the application of the OF [73]. In the AP plot both pulses are moved to have a zero baseline for a better comparison.

spectrum of the event to be filtered, respectively. Then from the filtered pulse the amplitude of the signal is obtained as the height of its maximum. An example of the AP and the ANPS before and after the filtering procedure is shown in Figure 3.3.

Thermal Stabilization

The amplitude obtained from the OF does not correspond yet to the energy released in the crystal. Bolometers operation depends on the temperature of the detector and even small variations could induce significant effects on the measured amplitude.
To overcome this CUORE exploits two kinds of Thermal Gain Stabilization (TGS): the heater-TGS and the calibration-TGS [75]. In the heater-TGS, the amplitude of heater events is plot against their baseline and fit with a linear function, which is then inverted and applied to all heater and physical events. An example of the heater-TGS effect can be seen in Figure 3.4.
The second type of TGS is called calibration-TGS and uses pulses at exactly 2615 keV. This additional TGS procedure is used for channels with a non-working heater, but can also be useful for channels with dataset-long baseline drifts, which cannot be corrected by the heater-TGS algorithm.

Calibration

The signal amplitude is converted to energy (in keV) using the calibration data collected at the beginning and end of each dataset. The calibrations are performed deploying ^{232}Th and ^{60}Co sources between the CUORE cryostat and the external lead shield [76]. The most prominent peaks in the stabilized amplitude spectrum of each channel are identified (see Table 3.1).

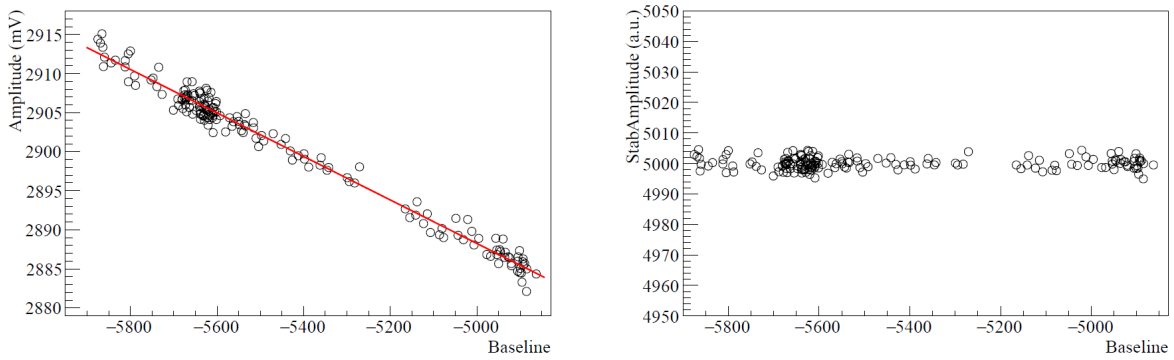

Figure 3.4: Example of the effect of the heater thermal gain stabilization. On the left is shown the amplitude from the OF versus the baseline before the stabilization with the gain function in red. While on the right the same data is shown after the amplitude correction. Plots courtesy of [73].

Table 3.1: List of the γ peaks from the ^{232}Th and ^{60}Co sources used in CUORE for energy calibration.

Peak Energy [keV]	Source
2615	^{232}Th
1332	^{60}Co
1173	^{60}Co
511	e^+e^-

After the peak identification, they are fitted using a specific probability density function that consists of a Gaussian with a power-law low-end tail plus a flat background. The output of the fit are the peak positions and if expressed in unit of stabilized amplitude they are used to obtain the calibration function, which is a second order polynomial in terms of A^S without a constant term, namely

$$E(A^S) = a \cdot (A^S) + b \cdot (A^S)^2 \ , \tag{3.4}$$

where a and b are the calibration coefficients.

3.3 Pulse Quality and Multi-channel Parameters

The last part of the offline data analysis goes from the calibrated events to the final data.

Pulse Shape Analysis

The Pulse Shape Analysis (PSA) is used to discriminate between clean physical events and various types of spurious events that might be triggered. For each pulse 6 quantities are calculated and then appropriate cuts on them will select the pulses that can be related to useful signals in the detector. Important kind of events that PSA aims to discard are noise pulses, piled-up events and electronic spikes.
The PSA parameters are:

- **Pulse Rise Time**: the pulse rise time is defined as

$$PRT[ms] = t(90\%) - t(10\%) \ , \tag{3.5}$$

  where $t(n\%)$ is the time when the pulse is $n\%$ of its maximum height. For example electronic spikes have very short rise time, while it is longer for pile-up events.

- **Pulse Decay Time**: in this case the time difference is calculated in the falling part of the pulse and it is defined as

$$PDT[ms] = t(30\%) - t(90\%) \ . \tag{3.6}$$

  Noise pulses also have a very short decay time.

- **Baseline Slope**: is the angular coefficient of a linear fit in the first part of the pre-trigger region (first 2.25 s out of the 3 s). It has to be as close to 0 as possible to discard events triggered on the tail of the previous one.

- **Peak Delay**: is the time, in milliseconds, between the beginning of the event window and the maximum of the pulse.

- **Test Variable Left and Right**: are the point by point sum of the squared difference between the detected pulse and the signal template pulse. The Left and Right refers to the fact that the sum is performed on the points on the left or right of the pulse maximum.

The distributions of these PSA parameters are energy dependent but there are also differences from channel to channel, due to different detector response, and between datasets [74]. To overcome these dependencies a new pulse shape discrimination technique, called Principal Component Analysis (PCA), is implemented. The main idea of PCA is to transform obtained data into a new basis ordered by how much of the data's variance is related to each coordinate [77]. First the PCA algorithm is trained with a sample of carefully chosen events, then the PCA decomposition is computed for signal-like events coming from calibration peaks obtaining a waveform very similar to the AP. In reality the AP of each detector within a dataset is treated as a sort of PCA eigenvector, then

every event coming from the same detector can be projected on it.
PCA for pulse shape discrimination exploit the fact that while it is not known how a "bad" pulse looks like, it is instead known that a "good" pulse should be similar to the AP, which is the obtained leading component. For each detected pulse the so-called Reconstruction Error (RE) can be calculated as

$$RE = \sqrt{\sum_i (\boldsymbol{x}_i - (\boldsymbol{x} \cdot \boldsymbol{p})\boldsymbol{p}_i)^2} \ , \tag{3.7}$$

where $\boldsymbol{p}$ is the leading component related to the AP and $\boldsymbol{x}$ are the values of the data vector, related to the analyzed waveform. Pulses similar to the average one have a low RE, while pulses that show atypical features are not well reconstructed and have a high RE. Therefore is possible to remove "bad" pulses from the obtained data by cutting on this calculated quantity.
PCA showed an improvement in the overall efficiency with respect the the usual PSA technique, along with a reduction in the pulse shape discrimination systematics and a higher robustness in the determination of the cut for all channels [50]. Moreover, precise details on the PCA used in CUORE can be found in [78].

Coincidence Analysis

The coincidence of events in different channels is very important, specifically for background rejection, because expected $\beta\beta$ events, both with or without neutrinos, will release their energy in a single crystal almost 90% of the times[1] while other radiations (β or γ) might trigger multiple detectors.
A variable called *Multiplicity* (M) is then attributed to each event, typically an event is said to be an Mn one, where n is the number of bolometers that detected an energy deposit. Understanding which is the value of the *Multiplicity* variable is what coincidence analysis part of the high level processing does. The difficult part is to being able to separate the true coincidence events, like Compton scattering in various crystals, from the accidental ones, which can be multiple $M1$ events occurring simultaneously.
Since different bolometers might have different response times, it is possible to define the *Jitter* as the time difference between the occurrence of the pulse maximum for two events in coincidence. An example is in Figure 3.5 where the two events, coming from calibration data, have a Jitter of about 27 ms and are compatible with the multiple Compton scattering of the 2615 keV ^{208}Tl γ ray.

[1] Obtained from Monte Carlo simulations [74].

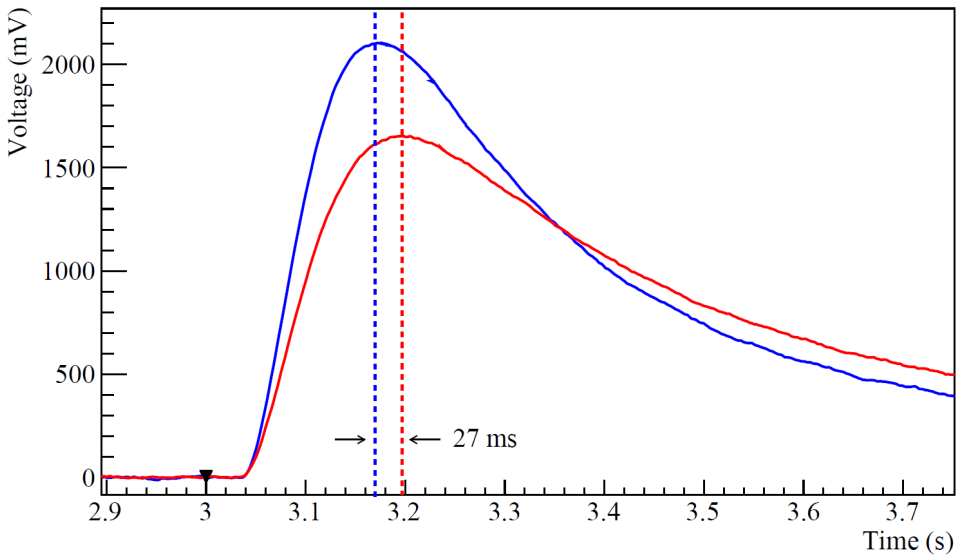

Figure 3.5: Example of the Jitter between two events in the same tower and in true coincidence. The vertical dotted lines highlight the position of the maximum and so the different response times of the bolometers.

For the analysis runs the coincidence time window on the Jitter is of ± 5 ms; moreover a geometrical condition can be implemented to select events that trigger detectors that are all in a small radius, since is more probable that true correlated events will deposit their energy in nearby crystals with respect to ones in opposite towers. Also an energy constraint is placed on the single pulses of this kind of events, $E > 40$ keV, since it is above the trigger threshold of the majority of the channels.

Chapter 4

CUORE Simulations and Background Model

The CUORE spectrum ranges from 40 keV to ~ 8 MeV, and can be divided in two regions. The energy region below the 2615 keV γ line from ^{208}Tl is dominated by the continuum of ^{130}Te $2\nu\beta\beta$ spectrum, and by gamma events induced by radioactive contamination of the TeO_2 crystals and of the cryostat components, while the energy region above the ^{208}Tl line is dominated by alpha events induced by radioactive contamination of the crystals and the crystal holders.
Figure 4.1 shows the latest measured CUORE spectrum together with a zoom into the ROI [50]. After the standard analysis cuts are applied, the continuum background at $Q_{\beta\beta}$ is estimated as composed by $\sim 90\%$ of degraded α particles coming from the radioactive decays of nuclei in the support structure, while the other $\sim 10\%$ comes from ^{208}Tl γ events at the 2615 keV peak. To quantify these background sources and how to suppress them, the so-called Background Model (BM) has been developed by fitting simulated spectra of all possible backgrounds to the data. This chapter will be dedicated to the description of the BM and the most important CUORE background sources.

4.1 CUORE Background Sources

A substantial number of background sources must be considered when studying the energy spectrum. The most important ones, for underground experiments, are events coming from the radioactive decays in the construction materials and from specific external sources, like cosmic rays.
The contribution from the latter type of events (e.g. cosmic muons or environmental photons and neutrons) is small thanks mainly to the natural shield which is the Gran Sasso mountain. Within the first category a distinction is required between events coming from the decay of long-lived radionuclide (natural ^{40}K and daughters of ^{232}Th and

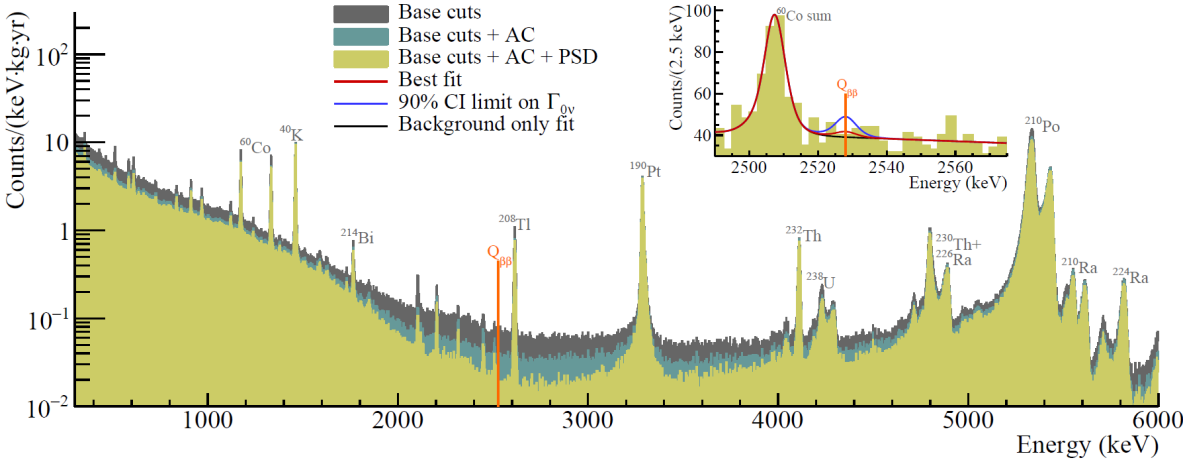

Figure 4.1: Physics spectrum for 1 ton·yr of TeO_2 exposure. The different colors shows the effect of the most important analysis cuts, namely anti-coincidence (AC) and pulse shape discrimination (PSD). The most prominent γ and α peaks are labeled. The inset shows the ROI with the best-fit curve (red), the same curve with the 90% CL limit on the $0\nu\beta\beta$ half-life (blue) and the background-only fit (black). Plot courtesy of [50].

^{235,238}U decay chains) and cosmogenically activated isotopes, like ^{60}Co, decays coming from the activation of Cu in the detector supports.

The CUORE BM is very similar to the one of its predecessor CUORE-0 [42], since the fabrication and cleaning of the detector towers is the same and also the underground location in the LNGS has not changed. The main difference between the two experiments is in the new CUORE cryostat, that has to be considered in BM studies.
In the following tables I report limits on the specific activity of different kinds of radioactive contamination of detector components, namely the TeO_2 crystals, the PTFE holders and the NOSV-Cu frames. In Table 4.1 are listed the specific activities obtained in the material screening campaign [59] while in Table 4.2 and 4.3 the ones from the CUORE-0 BM [42].

Table 4.1: 90% CL upper limits on surface contamination from material screening campaign. The measurement was performed at different depths in the material, listed in the second column, and the limit refers to the depth that yields the highest background contribution. The measurements are reported in Bq/cm^2.

Detector Component	Depth [μm]	^{238}U Activity	^{232}Th Activity	^{210}Pb Activity
TeO_2 Crystals	0.01-10	$< 8.9 \times 10^{-9}$	$< 1.9 \times 10^{-9}$	$< 9.8 \times 10^{-7}$
PTFE Holders	0.1-30	$< 6.8 \times 10^{-8}$	$< 1.9 \times 10^{-8}$	
NOSV-Cu Frames	0.1-10	$< 6.5 \times 10^{-8}$	$< 6.8 \times 10^{-8}$	$< 8.6 \times 10^{-7}$

Table 4.2: 90% CL upper limits and values of surface contamination from the CUORE-0 BM. Within the contamination type column if only the progenitor of the decay chain is reported then the rest of the chain is considered in secular equilibrium, otherwise single isotopes or sub-chains are taken into account.

Detector Component	Contamination Type	Depth [μm]	Activity [Bq/cm^2]
TeO_2 Crystals	^{238}U	10	$< 3.3 \times 10^{-11}$
	^{238}U-^{230}Th	0.01	$(2.07 \pm 0.11) \times 10^{-9}$
	^{232}Th	10	$(7.8 \pm 1.4) \times 10^{-10}$
	^{232}Th (single)	0.01	$(3 \pm 1) \times 10^{-9}$
	^{230}Th (single)	0.01	$(1.15 \pm 0.14) \times 10^{-9}$
	^{228}Ra-^{208}Pb	0.01	$(2.32 \pm 0.12) \times 10^{-9}$
	^{226}Ra-^{210}Pb	0.01	$(3.14 \pm 0.10) \times 10^{-9}$
	^{210}Pb	10	$< 2.7 \times 10^{-9}$
	^{210}Pb	1	$(8.6 \pm 0.8) \times 10^{-9}$
	^{210}Pb	0.001	$(6.02 \pm 0.08) \times 10^{-8}$
PTFE Holders	^{238}U	10	$(1.38 \pm 0.16) \times 10^{-8}$
	^{232}Th	10	$(5.0 \pm 1.7) \times 10^{-9}$
	^{210}Pb	10	$< 1.9 \times 10^{-8}$
	^{210}Pb	1	$(4.3 \pm 0.5) \times 10^{-8}$
	^{210}Pb	0.001	$(2.9 \pm 0.4) \times 10^{-8}$

Table 4.3: Values and 90% CL upper limits on bulk contamination in TeO_2 crystals from CUORE-0 BM. In the first column if only the progenitor of the decay chain is reported then the rest of the chain is considered in secular equilibrium, otherwise single isotopes or sub-chains of ^{232}Th and ^{238}U are considered.

Contamination Type	Activity [Bq/kg]
^{210}Po	$(2.39 \pm 0.11) \times 10^{-6}$
^{210}Pb	$(1.37 \pm 0.19) \times 10^{-6}$
^{232}Th (single)	$(7 \pm 3) \times 10^{-8}$
^{228}Ra-^{208}Pb	$< 3.5 \times 10^{-8}$
^{238}U-^{230}Th	$< 7.5 \times 10^{-9}$
^{230}Th (single)	$(2.8 \pm 0.3) \times 10^{-7}$
^{226}Ra-^{210}Pb	$< 7 \times 10^{-9}$

Figure 4.2 shows the CUORE expected background spectrum over a wider energy range, obtained by considering the contaminants activities non-compatible with zero together with CUORE-0 results on high activity background sources, like ^{130}Te $2\nu\beta\beta$ decay, NOSV-Cu bulk contamination and the ^{40}K ones in the crystals.

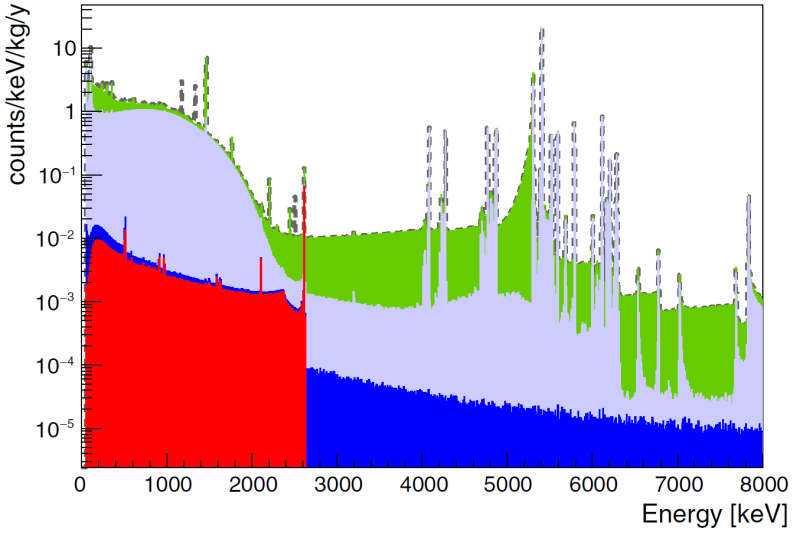

Figure 4.2: CUORE expected background spectrum considering most prominent background sources. The red distribution refers to natural radiation coming from far components such as insulation layers and support rods, the blue one refers to environmental muons, the light violet depends on TeO_2 crystals contamination and the ^{130}Te $2\nu\beta\beta$ decay, while the green one is obtained from NOSV-Cu contamination. Lastly, the grey dotted contour displays the total spectrum [59].

4.2 Background Reconstruction

The various backgrounds are simulated by means of two softwares: *qshields*, a Geant4 [79] code that simulate particles interacting and propagating in the whole detector geometry, and *Ares*, which will reprocess the simulated data including all the detector response parameters.
In *qshields* the whole CUORE geometry is implemented (from the crystals to the external shields) and it is possible to generate different kinds of events, like: single particles with precise energy or with a given distribution, the single decay of a nucleus and all the particles coming from it, a more complex decay chain or specific $\beta\beta$ decays.
Together with the detector geometry, other inputs are needed to perform an accurate simulation, like the particle source, its position in the volume and other parameters. Then several models can be used to simulate the interaction and all the propagation needed.
On the other hand, the *Ares* codes handles and processes the *qshields* output to obtain a data format similar to the one produced directly by the CUORE detector. Moreover, *Ares* will apply to Monte Carlo (MC) data the detector response and all the data analysis algorithms. Having two separated codes will allow a faster analysis if only some detector parameters change. To obtain simulated CUORE data which is as close as possible to real one, *Ares* needs to be able to reproduce all of the typical properties of real data. The most important ones being the energy resolution, the trigger threshold (which is different for each channel) and also a time information is needed to reproduce the expected event rate.

4.2.1 Reconstruction of the Background Sources

The cited simulation codes are used to study the effect of the various CUORE background sources. First we need to define the contamination source by specifying the radioactive nucleus, the contaminated part of the detector (e.g. crystals, NOSV-Cu, shields etc.) and the geometrical distribution of the contamination (surface or bulk).

The different types of background sources have been discussed in Section 4.1 and are mainly extracted from the BM of the CUORE-0 experiment. The main radioactive sources (^{232}Th and ^{235,238}U) are present in all the detector parts and ^{60}Co and copper are present in the crystals and in the frames, while cosmic and neutron fluxes information were obtained by previous measurements performed at LNGS [80].
The distinction between surface and bulk contamination has to be taken into account when α decays are considered, since the measured spectrum depends on the distribution of the radioactive contaminants:

- bulk contamination is uniform in the volume. Alpha decays induced by bulk contamination of the crystals will release their full energy, corresponding to the Q-value

of the reaction. On the other hand, alpha decays produced by bulk contamination of passive material will not release any energy in the crystals.

- Surface contamination is only present in a thin part of the volume. They are simulated only in the crystals and in the near part of the NOSV-Cu frames; moreover only fixed depths are analyzed (0.1, 1 and 10 μm). A shallow contamination ($\leq$ 10 nm) on the crystal surface will release the α energy in one crystal and the recoil energy in a neighboring one. A deep surface contamination of the crystal will release the nuclear recoil energy and a large fraction of the α energy on one crystal, and the remaining α energy on a neighboring one. On the other hand, a surface contamination on a passive material (PTFE or copper holders) will release a fraction of the energy in the passive material, and the remaining in the crystal, giving rise to a continuum spectrum of degraded α events.

Then the *Ares* parameters need to be set in order to go from MC data to CUORE-like one. For the energy resolution a true resolution curve response function is used and a fixed 40 keV trigger threshold is selected for all channels. A small event rate is then chosen to resemble the one of physics data.

4.3 Background Analysis

The CUORE BM is the fit of the combination of data coming from all background contributions. The data used for the BM belong to three spectra: $M1$, $M2$ and $M2Sum$, this latter refers to the spectrum of the sum on the energies of two events in coincidence. With M referring to the *Multiplicity* variable, see Section 3.3.
The M1 spectrum is selected because MC simulations predict that double beta events release their energy in one single crystal $\sim$ 90% of the time; while the two M2 ones because the majority of background events deposit their energy in two bolometers, like α particles coming from the radioactive decay of surface contamination. Therefore, $M2$ spectra contain a significant amount of information that can significantly improve the reconstruction of the $M1$ spectrum components.

Each of the expected spectra is obtained via MC simulations of the relative background source, then a linear combination of them is used to fit the observed spectra, via a Bayesian approach.
In the following, we denote the data as D, and the fit parameters (connected to the activity of all background sources and the half-life of the ^{130}Te $2\nu\beta\beta$ decay) with θ. We apply the Bayes theorem to evaluate the posterior distribution $P(\theta|D)$ [81]:

$$P(\theta|D) \propto P(D|\theta) \cdot P(\theta) \ , \tag{4.1}$$

where $P(\theta)$ is the product of the prior probability of all parameters θ and $P(D|\theta)$ is the likelihood, namely the probability of obtaining exactly the data D assuming the underlying parameters θ.
The CUORE BM is written as a linear combination of the N background spectra obtained by MC simulations as:

$$BM_i = \sum_j^N K_j \cdot C_{ij} \ , \tag{4.2}$$

where $i = M1, M2, M2Sum$ is the index referring to the multiplicity spectra, K_j is the normalization factor for the j-th background source (which are the parameters of the theory) and C_{ij} is the number of counts in the j-th simulated spectrum for a given multiplicity i.
The likelihoods are defined using the observed counts in the experimental (C_i^{exp}) and simulated (C_{ij}^{MC}) spectra, both following the Poisson statistics. Then directly from the Bayes' theorem, the joint posterior probability is:

$$\begin{aligned} P(K_j, \langle C_{ij}^{MC}\rangle | C_i^{exp}, C_{ij}^{MC}) = \prod_i Pois(C_i^{exp}|\langle C_i^{exp}\rangle) \times \prod_{ij} Pois(C_{ij}^{MC}|\langle C_{ij}^{MC}\rangle) \times \\ \times \prod_j Prior(K_j) \times Prior(\langle C_{ij}^{MC}\rangle) \ , \end{aligned} \tag{4.3}$$

where the counts in brackets refers to the expectation values of the counts in a single bin of the distribution. $Prior(K_j)$ express the knowledge about the background sources[1], while for $Prior(\langle C_{ij}^{MC}\rangle)$ a uniform prior is chosen.
To simplify the fitting procedure while also trying to reduce the systematics, the BM is considered as a binned analysis with a varying bin size. The minimum bin size is first set to 15 keV, however for example in regions near γ or α peaks some bins are merged to suppress the systematic uncertainties related to the peak shape. Moreover, less populated bins (counts < 30) are combined with their closest bin.

The fit is performed via Markov Chain Monte Carlo (MCMC) which aims at mapping the posterior by performing a random walk in the parameter space. Then the MCMC fit is performed using the Just Another Gibbs Sampler (JAGS) tool [82].
The evaluation of the parameters obtained by the corresponding fit of the BM can be used to obtain values or upper limits on the activity of the contamination.

[1]Gaussian prior for sources with a measured activity or uniform prior for lesser known sources.

Chapter 5

Study of Delayed Coincidences Events

5.1 Introduction

In the framework CUORE and its successor CUPID, the radiopurity of active and passive materials composing the experiment is a central parameter that influences the scientific potential of the experiments. Therefore different analysis methods are required to measure or set limits on the specific activities of the contaminating nuclei.
The contamination can have two different spacial distributions in all the experiment components; can be bulk, if its density is homogeneous in the component, or surface contamination, if instead is concentrated on the surface of the material. The former type can be entirely determined by the production history of the material, while the latter depends on many more factors like the possible exposure to contaminating sources or on how the cleaning of the component has been performed. Within my work I centered my attention on the evaluation of both bulk and surface contamination of the TeO_2 crystals, which induce event of different multiplicities: for example events with multiplicity M equal to 1 are more likely to be coming from bulk contamination while if $M > 1$ the event probably happened in the surface of the crystal.
Measurements from material screening campaign and from the CUORE-0 experiment on surface and bulk contamination of the most worrying radio nuclei are in Table 4.1 and 4.2-4.3 respectively.
For a more precise evaluation of such contamination, a more precise identification and measurement of the lower parts of the decay chains is needed. This is performed by the analysis of time-Delayed Coincidences (DC) produced by events belonging to the relevant decay chains occurring with precise time differences. In this thesis I focused on ^{232}Th and ^{235,238}U decay chains since they are the most common contamination of the active TeO_2 crystals and of the passive copper structure holding them.
DC analysis is very useful because it can provide additional information to the CUORE BM in an independent way, since this analysis exploits time correlations in order to high-

light the particular signatures of different radioisotopes; mainly when information taken from the energy spectrum does not allow for a distinct identification of the contaminants effect [50].

The first part of my analysis consists in searching in the CUORE data for pairs or triplets of events belonging to the selected sub-chain by imposing constraints on the multiplicity of the single event, on the energy of the involved particles and on the time difference between the decay of the nuclei. First I looked for events with energy compatible with a parent decay and then the same is done for events related to the decay of the daughters. A time constraint between the events is then put to consider only the ones that happened within 5 half-lives from each other, moreover for some specific signatures also a spacial condition is needed. The events are then stored to perform subsequent analysis on their energies and on the time difference.
All the selected sub-chains are chosen by taking into account the decay times of the involved nuclei; if is too short (order of ms) the events coming from the short-lived nucleus are piled up with the ones from its daughter and so it is not possible to distinguish between them, on the other hand if the decay time of a nucleus is too long (more than some days) the contamination of the selected events by random coincidences increases significantly since the time window is much larger. Moreover, the time duration of each CUORE dataset should be higher than all the decay times considered.
These cuts on the half-lives decrease the number of DC that it is possible to distinguish in the CUORE data, however thanks to the various signatures of the decays I managed to analyze relevant parts of the decay chains.

5.2 Decay Chains, Searched Signatures and Results

Figure 5.1 shows the ^{232}Th, ^{235}U and ^{238}U decay chains, together with information on the various types of decays taking place within the single chains. The important feature of a decaying nucleus are: its half-life (that can span from microseconds to 10^{10} years), the type of decay, with the energies of the relevant emitted radiations (α, β, γ) and their intensities.

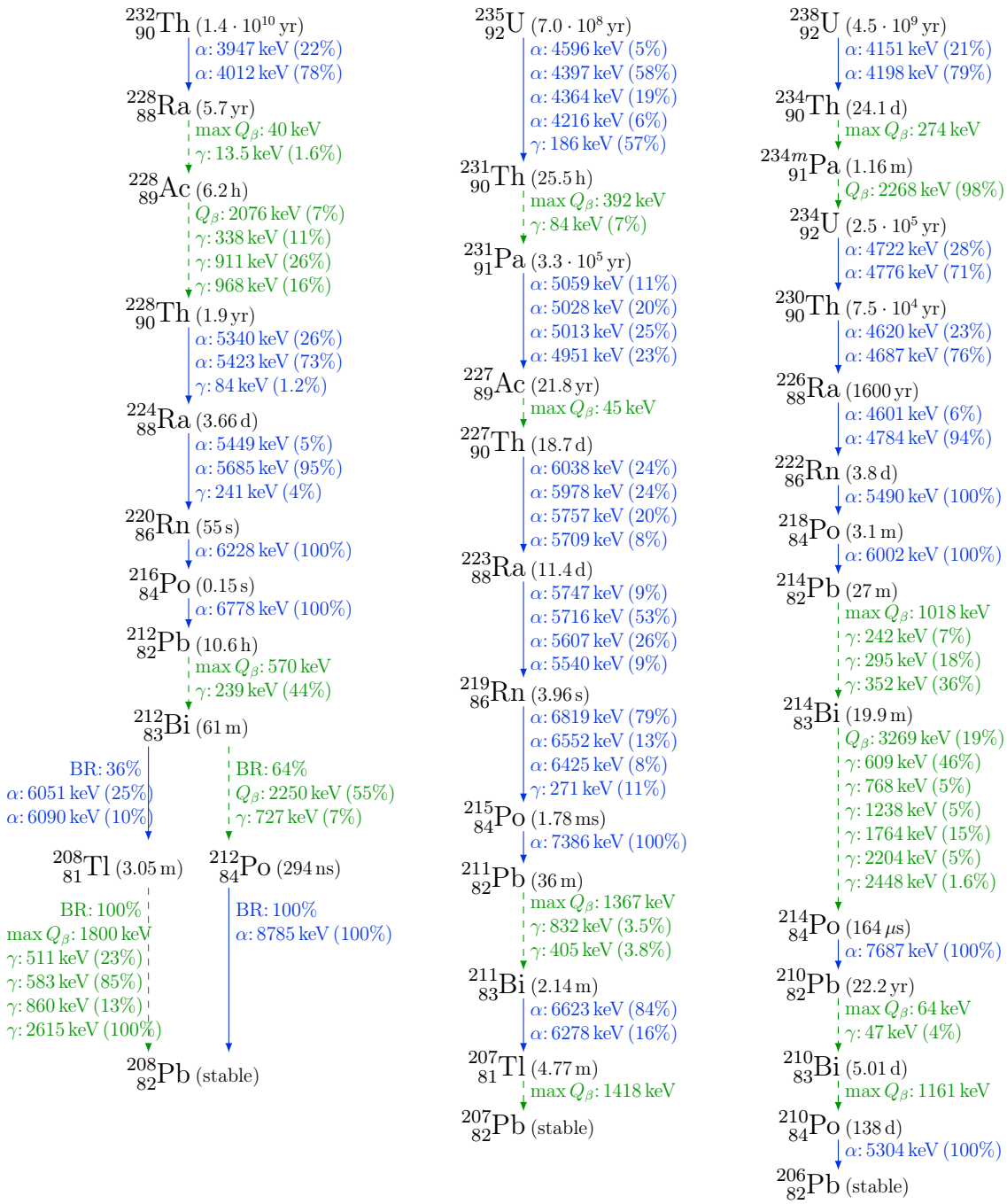

Figure 5.1: From left to right: ^{232}Th, ^{235}U and ^{238}U decay chains. For each nulcei in the decay chains the half-life is shown in brackets. The blue and green dotted lines represent α and β decays respectively. For each isotope I report the emitted radiations with relevant intensities. In the bottom part of the ^{232}Th decay chain, where more than one decay is possible, also the branching ratio is reported. The branches with a branches ratio $<1\%$ have been neglected.

Before reporting on the search of each DC, I will describe here the event selection procedure applied on the CUORE data. The first step was the selection of sub-chains and understanding which signatures to look for in the data. Each of them consist in two or three subsequent decays which generates events with a specific multiplicity. Then constraints are put on the multiplicity and on the energy of the particles taking place in the decays; for all the events satisfying these conditions, I stored the following quantities:

- **Energies**: the energies of the emitted radiations, stored in a vector of length equal to the M of the event;
- **Channels**: the M-vector of channels in which the particles released their energies;
- **Coordinates**: the tridimensional coordinates of each channel with a non-zero energy deposition, that are useful if spacial cuts are needed for the identification of the DC;
- **Time**: the time stamp of the event, also important for the DC identification.

Subsequently, spacial and time conditions were put on the stored quantities to identify the DC belonging to the searched signature. The spacial cuts can be translated as constraints on the channels and on the distances between them, obtained from their coordinates. Then for each event identified as the decay of a parent nucleus I opened a time window of 5 times the half-life of the daughter nucleus to search for an event in coincidence with the parent one.
When the events in coincidence are found, they are stored for subsequent analysis of their properties and also flagged so that they were not considered for following DC, removing in this way the possibility to have duplicates in the output data.

For each signature I will explain in detail the selection criteria and report the significant plots, e.g. the one and two dimensional energy distributions and the one of the time difference between the parent and daughter decay. The latter is fitted with a decaying exponential, namely

$$A(\Delta t) = B + A \exp\left(- \frac{\ln 2}{t_{1/2}} \Delta t \right) \tag{5.1}$$

where B, A and $t_{1/2}$ are the fit parameters. B is a constant component referring to possible background counts, while A is the amplitude of the exponentially decaying term, which is important for the activity evaluations. This fit is also performed to extract the half-life $t_{1/2}$ of the daughter nucleus and its comparison with tabulated values allow to understand if the DC has been well reconstructed.

5.2.1 Thorium-232 Decay Chain

Analysis of ^{228}Th $\rightarrow$ ^{224}Ra DC

The first part of the ^{232}Th decay chain that I analyzed is the ^{228}Th $\rightarrow$ ^{224}Ra DC. It is suitable for this kind of search since the ^{224}Ra half-life $t_{1/2}(^{224}\text{Ra}) = 3.66$ days is compatible with CUORE datasets duration.
For this decay sub-chain I analyzed three signatures, starting with $M1$-$M1$ α decays for both nuclei without the emission of other radiations, then I looked for $M1$-$M2$ and $M2$-$M1$ DC, where the $M2$ events consist of an α signal coming from the decay to an excited state with the emission of a de-excitation γ. An example of a simplified scheme of such DC can be seen in Figure 5.2. Notice that the light blue part is labeled as the "Superficial" part of the crystal; here and for all the signature schemes in this thesis the proportion between "Bulk" and "Superficial" part is exaggerated, since in reality the surface of the crystals is considered as the first few μm.

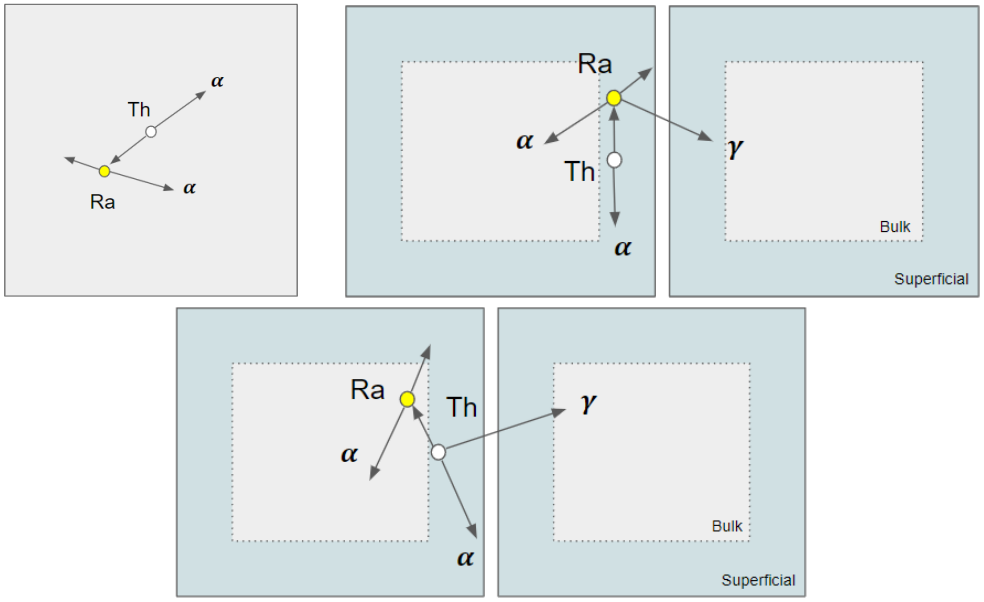

Figure 5.2: Scheme of ^{228}Th $\rightarrow$ ^{224}Ra DC signatures. The colored squares refer to the crystals in which the decay takes place. Top left $M1$-$M1$, top right $M1$-$M2$ and bottom $M2$-$M1$.

The correlated events should satisfy the following energy requirements: the $M1$ ^{228}Th events must have an energy compatible with its decay Q-value (5520 keV), while for $M1$ ^{224}Ra events the Q-value is 5789 keV. When $M2$ events are considered the energy of the de-excitation γ emitted should be compatible with 84 keV for ^{228}Th and 241 keV for ^{224}Ra, while the energy of the αs should be instead compatible with

$$E_\alpha = Q - E_\gamma \ . \tag{5.2}$$

Moreover events identified as the daughter decay need to be within $5 \cdot t_{1/2}(^{224}\mathrm{Ra})$ from the ones associated with the parent decay. The imposed spacial cuts are: the αs needs to be detected in the same channel while the γ must release its energy within a 30 cm radius from the channel of the αs. As an example, the following plots (Figure 5.3) displays the results relative to the $M1$-$M1$ signature, while results on the other two signatures are in Appendix A, namely in Figure A.1 and A.2.

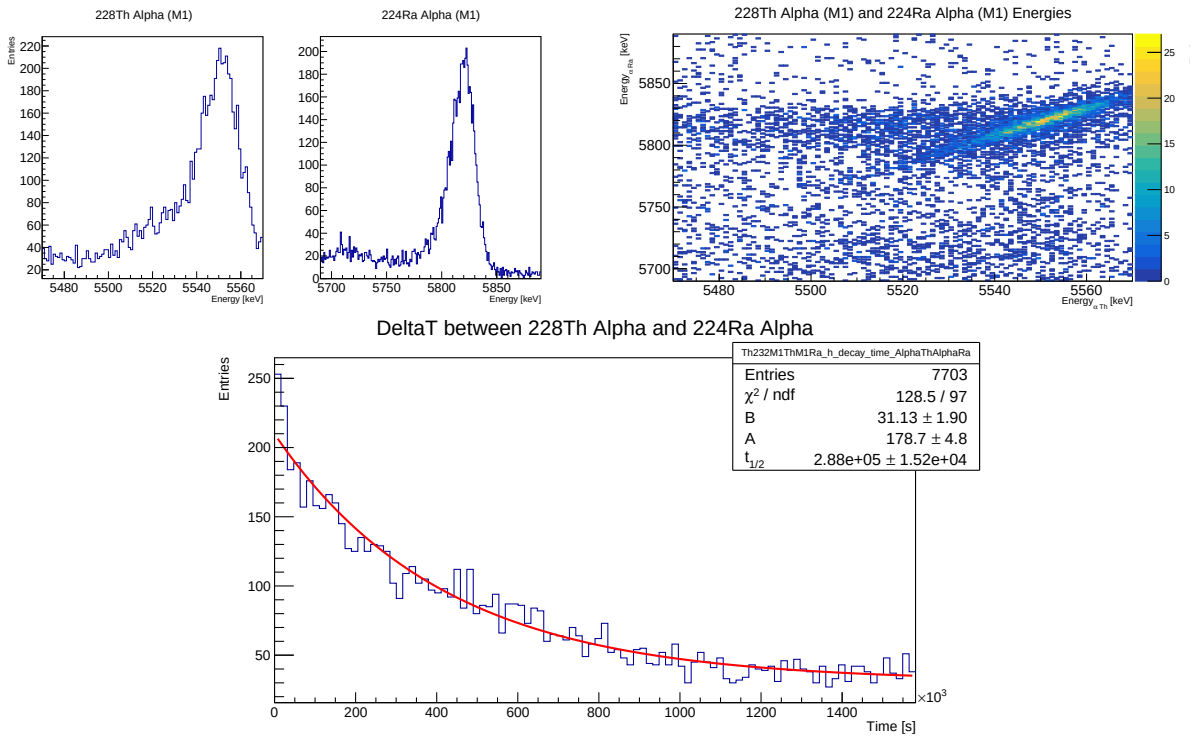

Figure 5.3: Results of $M1$-$M1$ $^{228}\mathrm{Th} \rightarrow {}^{224}\mathrm{Ra}$ DC search. Top left/right: one/two dimensional energy distribution. Bottom: time difference distribution fitted with Eq. 5.1.

Analysis of ^{212}Pb $\rightarrow$ ^{212}Bi DC

The lower part of the ^{232}Th chain can be studied via the

$$^{212}\mathrm{Pb} \rightarrow {}^{212}\mathrm{Bi} \rightarrow {}^{208}\mathrm{Tl}$$

sub-chain since the half-lives of the daughter nuclei are relatively small.
For the ^{212}Pb $\rightarrow$ ^{212}Bi DC I looked for only one signature (see Figure 5.4) consisting of an $M2$ β decay with a 238 keV γ emission for ^{212}Pb and an $M1$ α decay for ^{212}Bi. To select the correlated events the energy of the β emission should satisfy the following requirement

$$E_\beta < E_\beta^{\max} = Q(^{212}\mathrm{Pb}) - E_\gamma \ , \tag{5.3}$$

where $Q(^{212}\text{Pb}) = 569$ keV is the ^{212}Pb Q-value and E_γ is the energy of the emitted photon, while the ^{212}Bi event must have an energy compatible with its own Q-value (6207 keV) and be within $5 \cdot t_{1/2}(^{212}\text{Bi}) = 5 \cdot 60.5$ min from the ^{212}Pb decay. In this case further spacial conditions are needed: the channel in which the ^{212}Bi decay is detected must be the same in which the β emission releases its energy, while the γ needs to be detected within a 30 cm radius. See Figure A.3 for the results of this search.

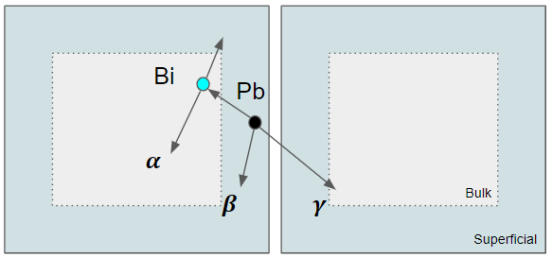

Figure 5.4: Scheme of the $M2$-$M1$ ^{212}Pb $\rightarrow$ ^{212}Bi DC signature. Notice that a β decay, such as the Pb one, will cause a close to zero recoil of the nucleus, here is exaggerated to better portray the searched signature.

Analysis of ^{212}Bi $\rightarrow$ ^{208}Tl DC

A very interesting DC that can be considered is the coincidence of ^{212}Bi and ^{208}Tl decay events. It fact the daughter Tl nucleus can decay with various signatures involving both β and γ emissions, while also having a short half-life, $t_{1/2}(^{208}\text{Tl}) = 3.05$ minutes. Moreover, being sensitive to this DC is useful since the main ^{208}Tl γ emission is the very sharp 2615 keV γ line, which is close to the ^{130}Te $Q_{\beta\beta}$ (see Table 1.2) which is also used for the calibration of the CUORE detectors.
The chosen signatures always consist of a $M1$ ^{212}Bi α decay with energy deposited compatible with its 6207 keV Q-value, while for the ^{208}Tl event I considered its β decay with γ emissions, the event can have various multiplicities ($M2$, $M3$ or $M4$ are the ones analyzed) depending on how many γ rays are emitted. The ^{208}Tl β emission should have an enery below the Q-value of the decay ($\sim$ 4999 keV) minus the energies of the considered photons[1], in this search I selected a combination of the 2615, 583, 510 and 860 keV γ emissions. The spacial cuts for this DC search are: the decay of the two nuclei should take place in the same crystal and the emitted photons should be detected in a 30 cm radius. The time constraint only selects the ^{208}Tl decays happening in a $5 \cdot t_{1/2}(^{208}\text{Tl}) = 5 \cdot 3.05$ minutes time window opened when a ^{212}Bi decay is identified. The usual schemes of the signatures are in Figure 5.5. A peculiarity of the $M1$-$M2$ signature is that the first event of ^{208}Tl decay is considered as a single energy deposition coming from two or more particles (the β emission and one or more γ).

[1]Since ^{208}Tl almost always decays to excited states of ^{208}Pb and then de-excitation γs are emitted to reach its ground state.

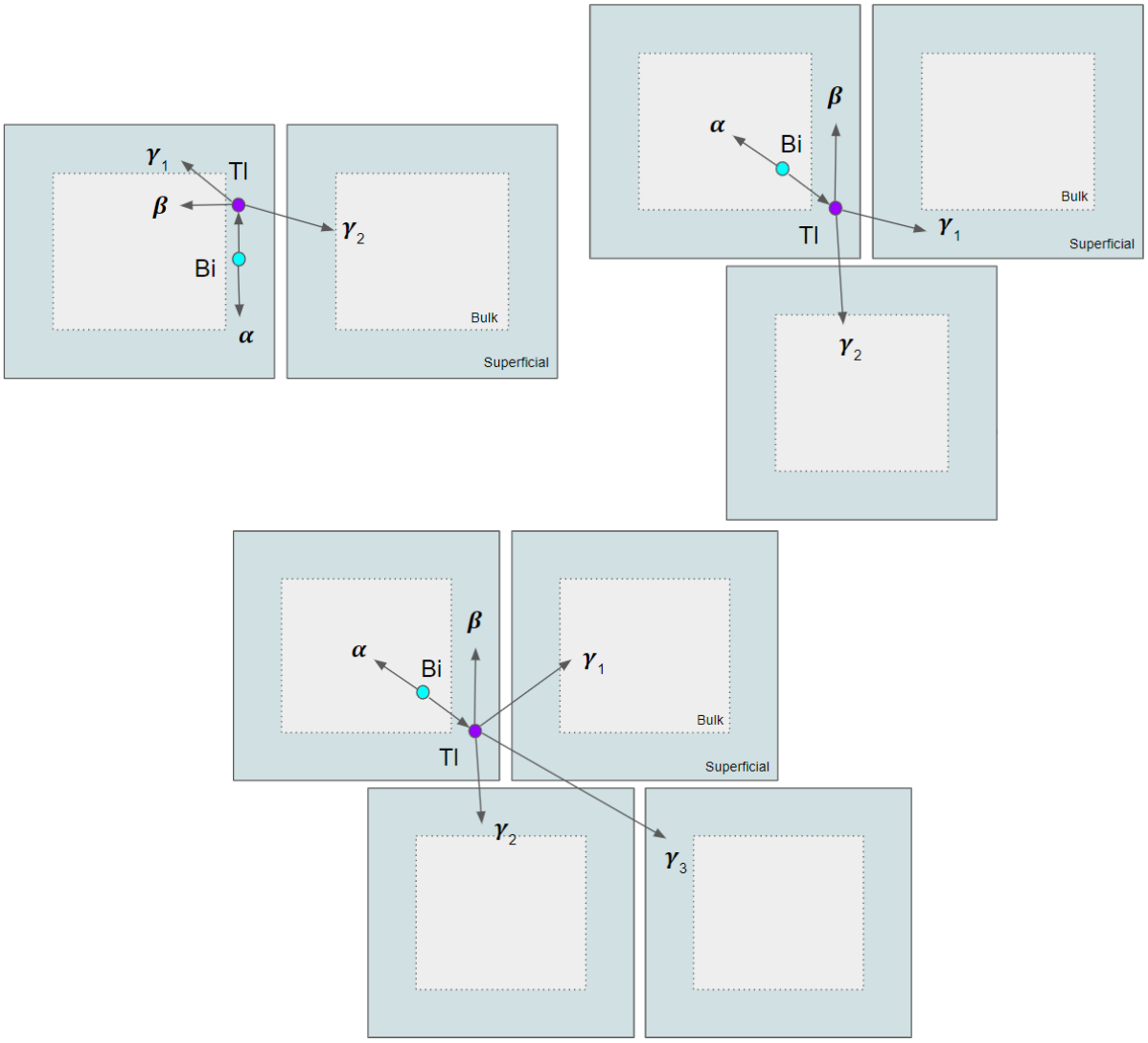

Figure 5.5: Scheme of ^{212}Bi $\rightarrow$ ^{208}Tl DC signatures. Top left $M1$-$M2$, top right $M1$-$M3$ and bottom $M1$-$M4$.

The considered ^{208}Tl events are:

- ***M4***: ^{208}Tl β with the 2615, 860 and 511 keV γs or with the 583 keV one instead of the 860 keV.
- ***M3***: ^{208}Tl β with the 2615 and 583 keV γs.
- ***M2***: The $M2$ events always consist of the 2615 keV photon and the other energy deposition here comes from the β and one or more γ in the same channel. I searched

for: $\beta + 860$ keV γ, $\beta + 583$ keV γ and $\beta + 583 + 511$ keV γs. Figure 5.6 shows here the results of the former $M2$ signature listed here.

Regarding the DC involving $M4$ ^{208}Tl events the combination of a very energetically constrained search with the consideration of low intensity emissions provided non-significant results, therefore they were removed from the analysis. In a similar way, for $M3$ ^{208}Tl events only the 583 keV photon is considered with the 2615 keV one, since it is the only combination laying out noteworthy results.
All graphical results regarding this DC can be found in Appendix A, from Figure A.4 throughout Figure A.6.

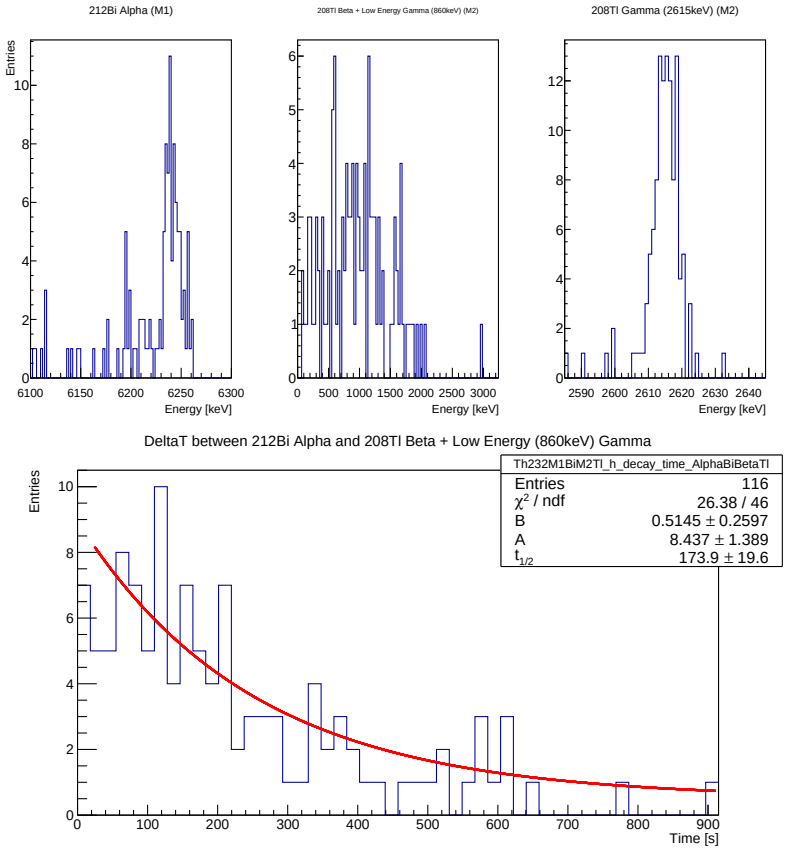

Figure 5.6: Results of $M1$-$M2$ ^{212}Bi $\rightarrow$ ^{208}Tl DC search. The top plots shows the one dimensional energy distribution of the particles emitted in the decays, while on the bottom is shown the distribution of the time differences between the ^{212}Bi decay and the ^{208}Tl, together with the fit results.

As a summary of the results of the performed DC searches, Table 5.1 lists the number of DC found for each of the explained signatures and the value of the fit parameter A

obtained by the time difference distributions. These results will then be useful for ^{232}Th specific activity evaluation.

Table 5.1: Summary of DC results for ^{232}Th decay chain.

Decay Sub-Chain	Signature	DC Found	A
^{228}Th $\rightarrow$ ^{224}Ra	$M1$-$M1$	7703	178.7 $\pm$ 4.8
	$M1$-$M2$	56	2.5 $\pm$ 0.8
	$M2$-$M1$	229	4.8 $\pm$ 0.7
^{212}Pb $\rightarrow$ ^{212}Bi	$M2$-$M1$	243	4.1 $\pm$ 0.7
^{212}Bi $\rightarrow$ ^{208}Tl	$M1$-$M3$, 583 keV γ	39	3.1 $\pm$ 0.8
	$M1$-$M2$, $\beta + 860$ keV	116	8.4 $\pm$ 1.4
	$M1$-$M2$, $\beta + 583$ keV	115	8.6 $\pm$ 1.4
	$M1$-$M2$, $\beta + 583 + 511$ keV	116	8.2 $\pm$ 1.4

5.2.2 Uranium-235 Decay Chain

Similarly to the last section, here I report the results of the DC searches for the ^{235}U decay chain. In this case I considered two decay sub-chains: ^{227}Th $\rightarrow$ ^{223}Ra and ^{211}Pb $\rightarrow$ ^{211}Bi.

Analysis of ^{227}Th $\rightarrow$ ^{223}Ra DC

Starting from the ^{227}Th $\rightarrow$ ^{223}Ra search, the ^{223}Ra half-life $t_{1/2}(^{223}\text{Ra}) = 11.4$ days is suitable for DC analysis. Notice that such long decay half-life might induce the presence of random DC due to other background sources in the considered energy ranges.
The selected signatures (see Figure 5.7) are: an $M1$ α emission from each nuclei both with energies compatible with their respective Q-values, namely 6146 keV for ^{227}Th and 5979 keV for ^{223}Ra, and detected in the same crystal; while for the slightly more complex $M2$-$M1$ signature, the $M2$ ^{227}Th event consist of the detection of both the α emitted and the recoil of the nucleus, in this case the α energy should be compatible with the 6038 keV ^{227}Th α emission, while the energy of the recoil is consistent with what obtained via

$$E_R = Q(^{227}\text{Th}) - E_\alpha = (6146 - 6038)\ \text{keV} = 108\ \text{keV}\ . \tag{5.4}$$

For this latter signature the spacial requirements is that the channel which detected the ^{223}Ra decay is the same as the one which detected the ^{227}Th recoil. Also in this case the time cuts requires that the ^{223}Ra decay happens within $5 \cdot t_{1/2}(^{223}\text{Ra}) = 5 \cdot 11.4$ days from

the ^{227}Th decay. Here I explicitly show the results obtained for the $M2$-$M1$ signature (see Figure 5.8) while other relevant results can be found in Appendix B.

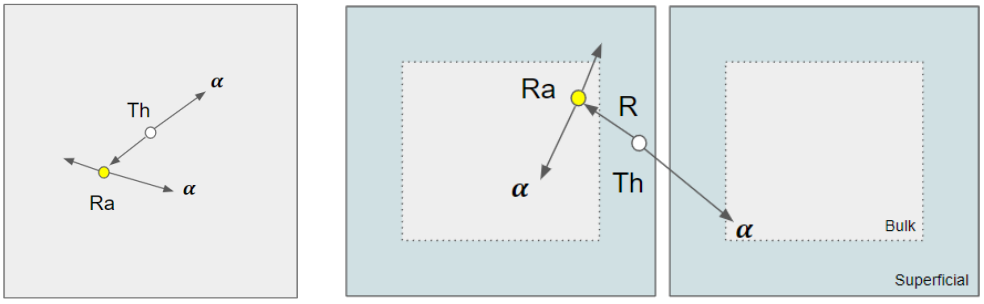

Figure 5.7: Scheme of ^{227}Th $\rightarrow$ ^{223}Ra DC signatures. Left $M1$-$M1$ and right $M2$-$M1$. The R labeled arrow refers to the recoil of the nucleus and it is made explicit in the schemes only if the recoil is explicitly a part of searched events.

Analysis of ^{211}Pb $\rightarrow$ ^{211}Bi DC

Another possible DC search is the one involving the ^{211}Pb decay into ^{211}Bi. While ^{211}Bi offers a very clear α decay easy to select in the CUORE data, ^{211}Pb decays with the emission of a β radiation with the possible presence of low intensity ($\sim 3\%$) photons. In principle the daughter half-life ($t_{1/2}(^{211}\text{Bi}) = 2.14$ minutes) is suitable for DC searches. However, the continuous β energy spectrum and the very low intensity of the emitted γs together with the fact that more random coincidences are present if a searched decay (^{211}Pb) only involves β and γ radiation, does not allow a significant DC search for this particular sub-chain. Therefore to characterize the ^{235}U contamination I will only consider the results obtained from the ^{227}Th $\rightarrow$ ^{223}Ra DC, that are summarized in Table 5.2.

Table 5.2: Summary of DC results for ^{235}U decay chain.

Decay Sub-Chain	Signature	DC Found	A
^{227}Th $\rightarrow$ ^{223}Ra	$M1$-$M1$	3653	34.2 ± 4.2
	$M2$-$M1$	854	8.5 ± 1.7

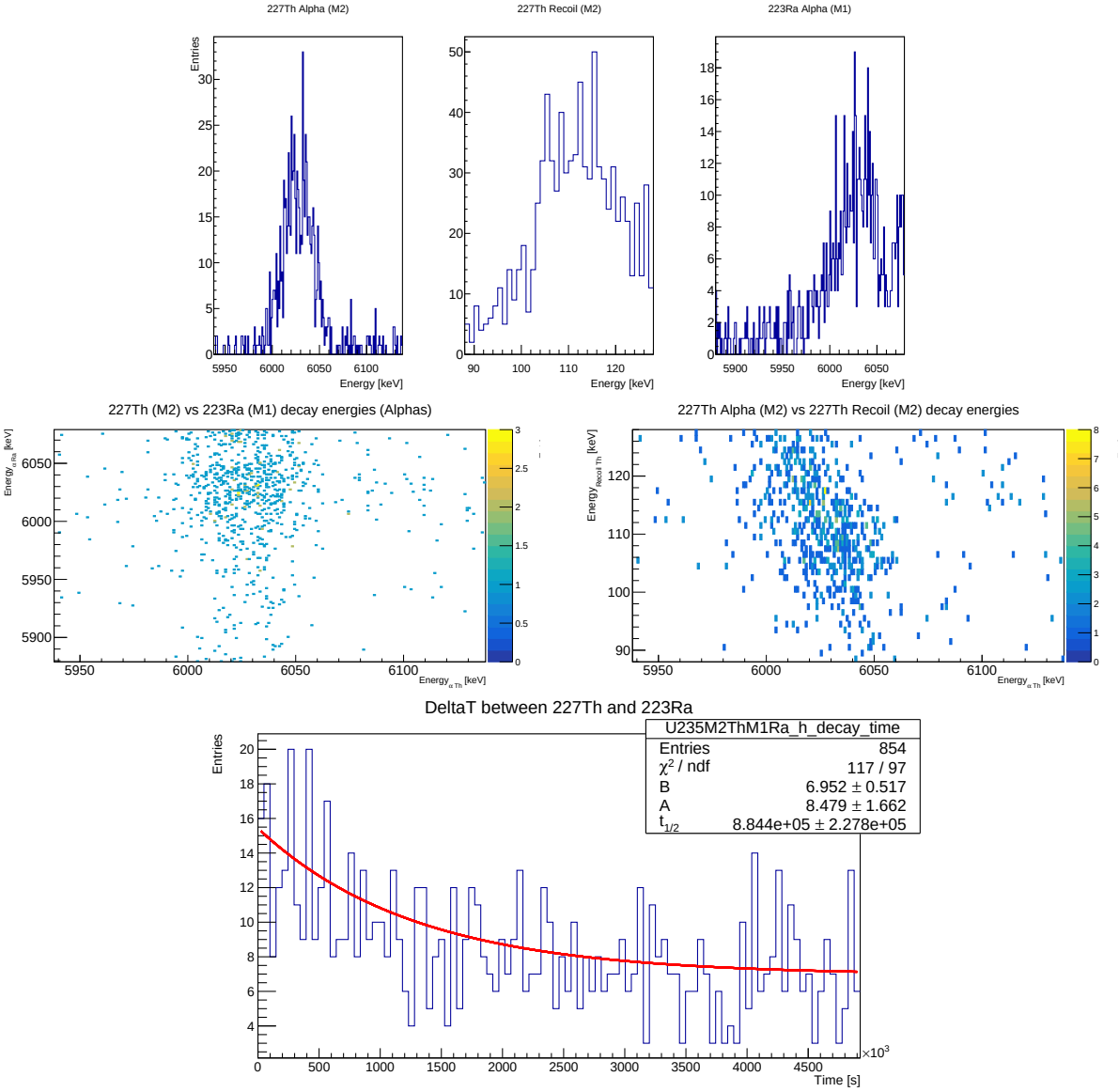

Figure 5.8: Results of $M2$-$M1$ ^{227}Ra $\rightarrow$ ^{223}Th DC search. Top left: one dimensional energy distributions. Top right: two dimensional energy distribution of α emissions. Bottom left: two dimensional energy distribution of ^{227}Th $M2$ events. Bottom right: time difference distribution between the two decays fitted with Eq. 5.1.

5.2.3 Uranium-238 Decay Chain

The last contamination analyzed in this thesis is the one relative to natural ^{238}U. Within this decay chain I was able to select various signatures all belonging to the same

$$^{226}\text{Ra} \rightarrow \ ^{222}\text{Rn} \rightarrow \ ^{218}\text{Po}$$

sub-chain. This part of the ^{238}U is easy to identify in the CUORE data since all three nuclei decays via α decay without the emission of other relevant radiations, while also having half-lives compatibles with what is needed to perform DC analysis, namely being around 186 seconds for ^{218}Po and 3.8 days for ^{222}Rn. This latter ^{222}Rn half-life is fairly long, in fact if only the ^{226}Ra $\rightarrow$ ^{222}Rn sub-chain is considered a lot of random DC are found. To avoid this, I did not focus on ^{226}Ra $\rightarrow$ ^{222}Rn DC searches but I rather considered coincidence events made of three decays, instead of the usual pairs; one for each nucleus of the sub-chain. This kind of DC search also allowed to select more complex signatures even if the three decays only involves α emissions.
Moreover, I also studied the ^{222}Rn $\rightarrow$ ^{218}Po part of the sub-chain independently.

Analysis of ^{222}Rn $\rightarrow$ ^{218}Po DC

The simpler ^{222}Rn $\rightarrow$ ^{218}Po DC search offers very clean α decay for both involved nuclei. Combining $M1$ and $M2$ events for both nuclei one can obtain the four signatures searched for this DC. $M1$ events consist of energy depositions compatible with the Q-values of decaying nucleus, these being

$$Q(^{222}\text{Rn}) = 5590 \text{ keV and } \ Q(^{218}\text{Po}) = 6115 \text{ keV} \ . \tag{5.5}$$

While $M2$ events are composed by first the energy deposition caused by the emitted α particle and the one related to the recoil of the nucleus. By knowing the energies of the α emissions, namely

$$E_\alpha(^{222}\text{Rn}) = 5489 \text{ keV and } \ E_\alpha(^{218}\text{Po}) = 6002 \text{ keV} \ , \tag{5.6}$$

then energies of the recoils of the nuclei can be obtained by subtracting E_α to the relative Q-value, as in Eq. 5.4.
A scheme of the four signatures considered in my analysis is shown in Figure 5.9.

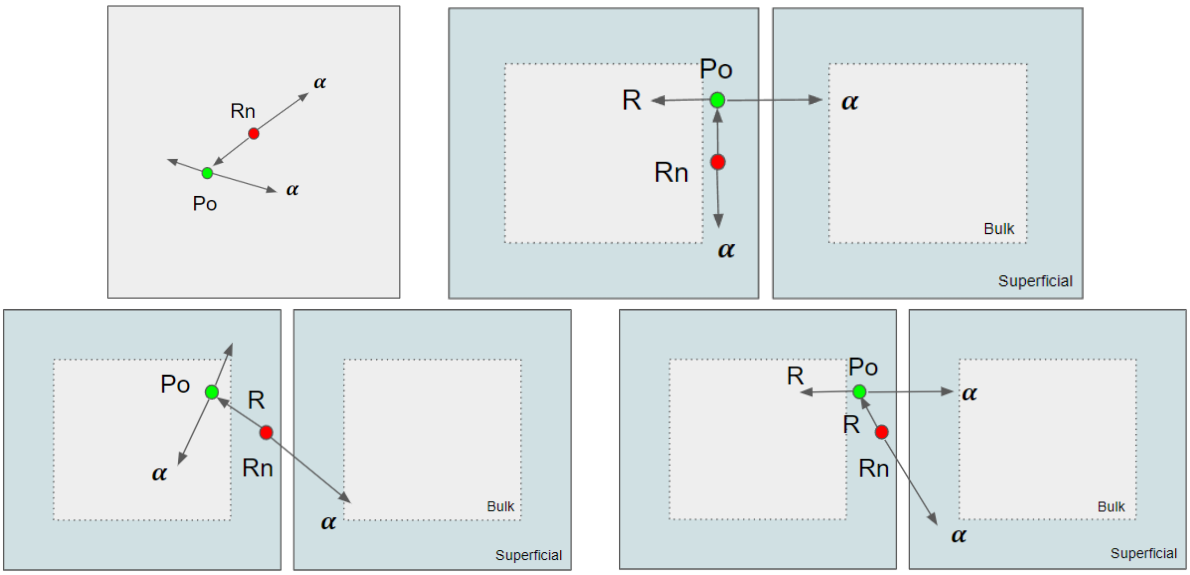

Figure 5.9: Scheme of ^{222}Rn $\rightarrow$ ^{218}Po DC signatures. From top left to bottom right: $M1$-$M1$, $M1$-$M2$, $M2$-$M1$ and $M2$-$M2$ signatures.

To select events belonging to this DC the ^{218}Po event should release its energy in a time window of $5 \cdot t_{1/2}(^{218}\text{Po}) = 5 \cdot 186$ seconds, opened when a radon event is detected. While spacial conditions are different for each signature (listed below), with a general requirement on the nucleus recoils that should be detected within a 12 cm radius from the channel impinged by the relative α particle.

- ***M1-M1***: both events detected in the same crystal.
- ***M1-M2***: one of the two energy depositions coming from the $M2$ ^{218}Po event should be in the same channel which detected the ^{222}Rn decay.
- ***M2-M1***: the $M1$ ^{218}Po event has to release its energy in the crystal in which the ^{222}Rn recoil is detected.
- ***M2-M2***: lastly for $M2$-$M2$ DC, one can have two possibilities. The channel of the ^{222}Rn recoil should be the same as the one of either the ^{218}Po recoil or α emission.

Figure 5.10 displays the graphical results for the $M1$-$M1$ DC search, while additional results can be found in Appendix C.

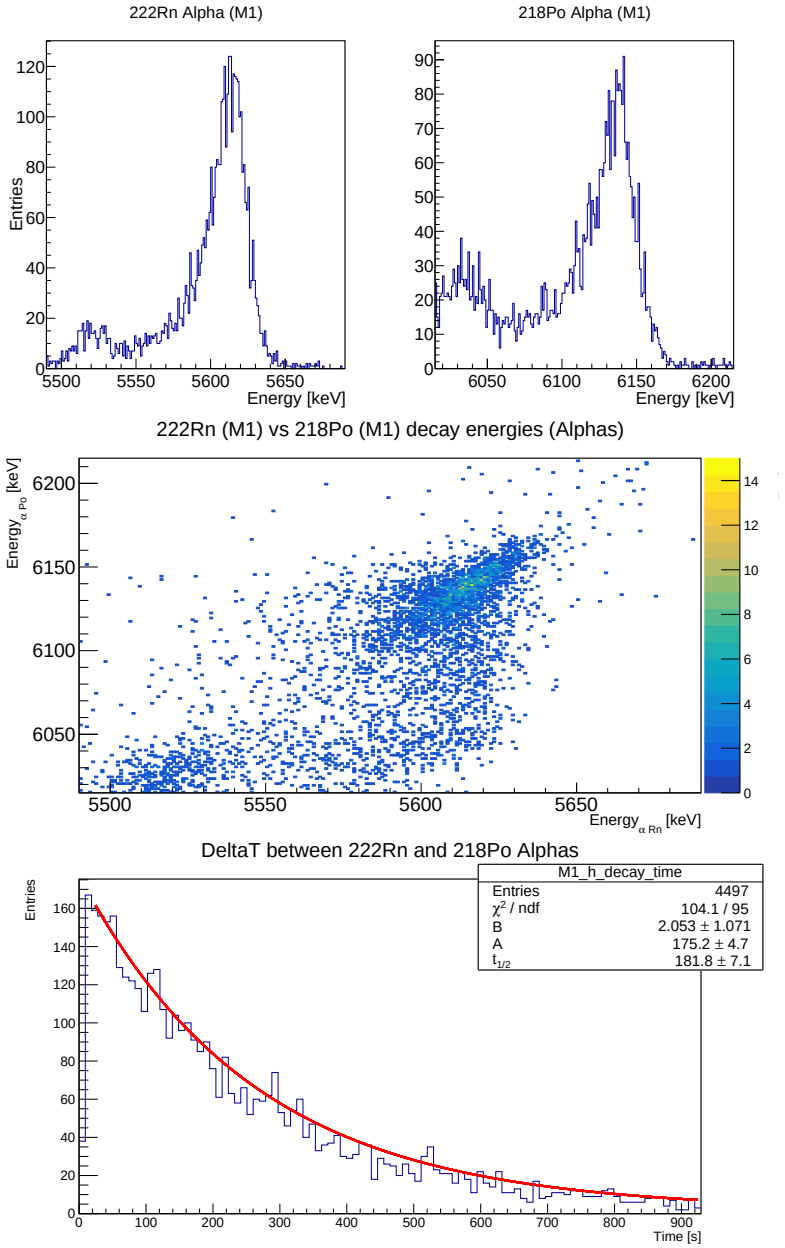

Figure 5.10: Results of $M1$-$M1$ ^{222}Rn $\rightarrow$ ^{218}Po DC search. The top plots show the energy distribution of the two $M1$ events, while the middle one combines them in a two dimensional distribution. On the bottom there is the distribution of the time differences between the two events, fitted with Eq. 5.1.

Analysis of ^{226}Ra $\rightarrow$ ^{222}Rn $\rightarrow$ ^{218}Po DC

The last DC analysis performed in this thesis adds another α decaying nucleus to the discussed ^{222}Rn $\rightarrow$ ^{218}Po DC. This allowed me to consider more specific signatures and further improve the study of the ^{238}U contamination. The energetic properties of the additional ^{226}Ra decaying nucleus are

$$Q(^{226}\text{Ra}) = 4870 \text{ keV}, \quad E_\alpha(^{226}\text{Ra}) = 4784 \text{ keV and} \quad E_R(^{226}\text{Ra}) = 86 \text{ keV} , \tag{5.7}$$

so an $M1$ ^{226}Ra event consist of one energy deposition compatible with $Q(^{226}\text{Ra})$, while an $M2$ one with two depositions compatible with E_α and E_R.
The considered signatures are: $M1$-$M1$-$M1$, $M2$-$M1$-$M1$, $M2$-$M2$-$M1$ and $M2$-$M2$-$M2$, schematically[2] shown in Figure 5.11.

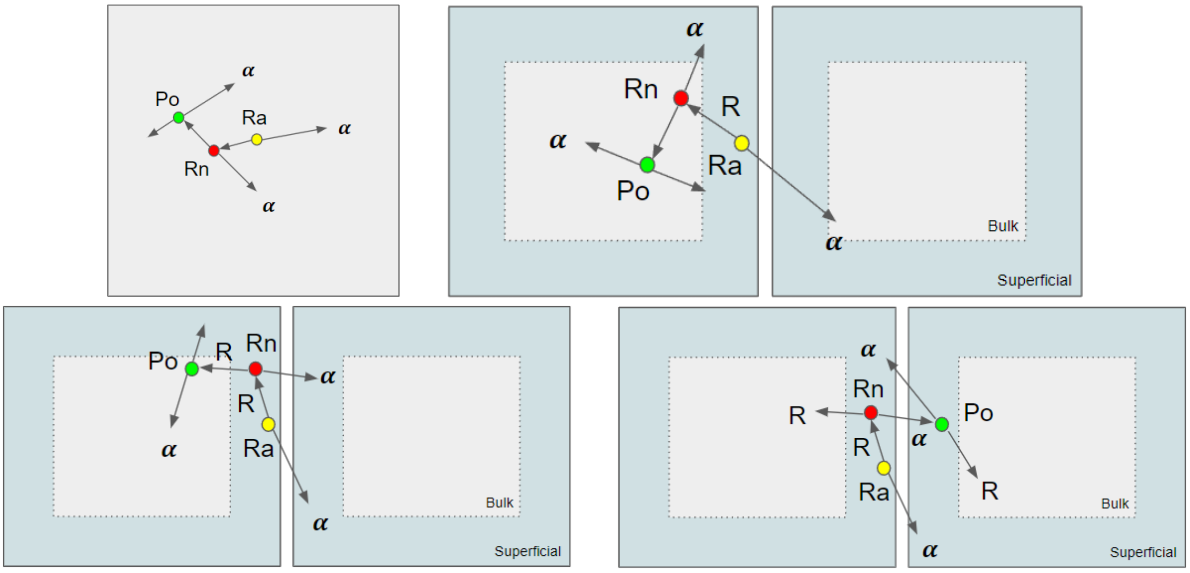

Figure 5.11: Scheme of ^{226}Ra $\rightarrow$ ^{222}Rn $\rightarrow$ ^{218}Po DC signatures. From top left to bottom right: $M1$-$M1$-$M1$, $M2$-$M1$-$M1$, $M2$-$M2$-$M1$ and $M2$-$M2$-$M2$ signatures.

To select the events in coincidence first I looked for a ^{222}Rn decay happening within $5 \cdot t_{1/2}(^{222}\text{Rn}) = 5 \cdot 3.8$ days from the identified ^{226}Ra event, then a ^{218}Po event in delayed coincidence with the ^{222}Rn one will complete the triplet of events in DC.
The spacial conditions for each pair of consecutive events within the triplet are the same as the one discussed above in the ^{222}Rn $\rightarrow$ ^{218}Po search section, always with the requirement that the recoil of the nucleus must be detected in a 12 cm radius with respect to the channel in which the relative α emission is identified.

[2]Notice that these are just examples, in reality the combination of channels in which the particles release their energy can be much more complex.

In the following plots (Figure 5.12) I report the results relative to the $M2$-$M1$-$M1$ signature, while the rest are all grouped in Appendix C.

The numerical results obtained from the study of the ^{238}U decay chain are outlined in Table 5.3. Here two A parameters are present, one for each time difference distribution; the one relative to the $^{226}\text{Ra} \rightarrow {}^{222}\text{Rn}$ events (A') is only present for triplet searches.

Table 5.3: Summary of DC results for ^{238}U decay chain.

Decay Sub-Chain	Signature	DC Found	A	A'
$^{222}\text{Rn} \rightarrow {}^{218}\text{Po}$	$M1$-$M1$	4497	175.2 ± 4.7	
	$M1$-$M2$	723	54.2 ± 3.3	
	$M2$-$M1$	640	31.3 ± 2.1	
	$M2$-$M2$	312	26.1 ± 2.7	
$^{226}\text{Ra} \rightarrow {}^{222}\text{Rn} \rightarrow {}^{218}\text{Po}$	$M1$-$M1$-$M1$	2020	79.4 ± 3.2	29.3 ± 2.7
	$M2$-$M1$-$M1$	550	40.6 ± 3.2	22.6 ± 2.4
	$M2$-$M2$-$M1$	68	4.6 ± 0.9	4.8 ± 1.6
	$M2$-$M2$-$M2$	56	4.2 ± 1.2	4.8 ± 0.9

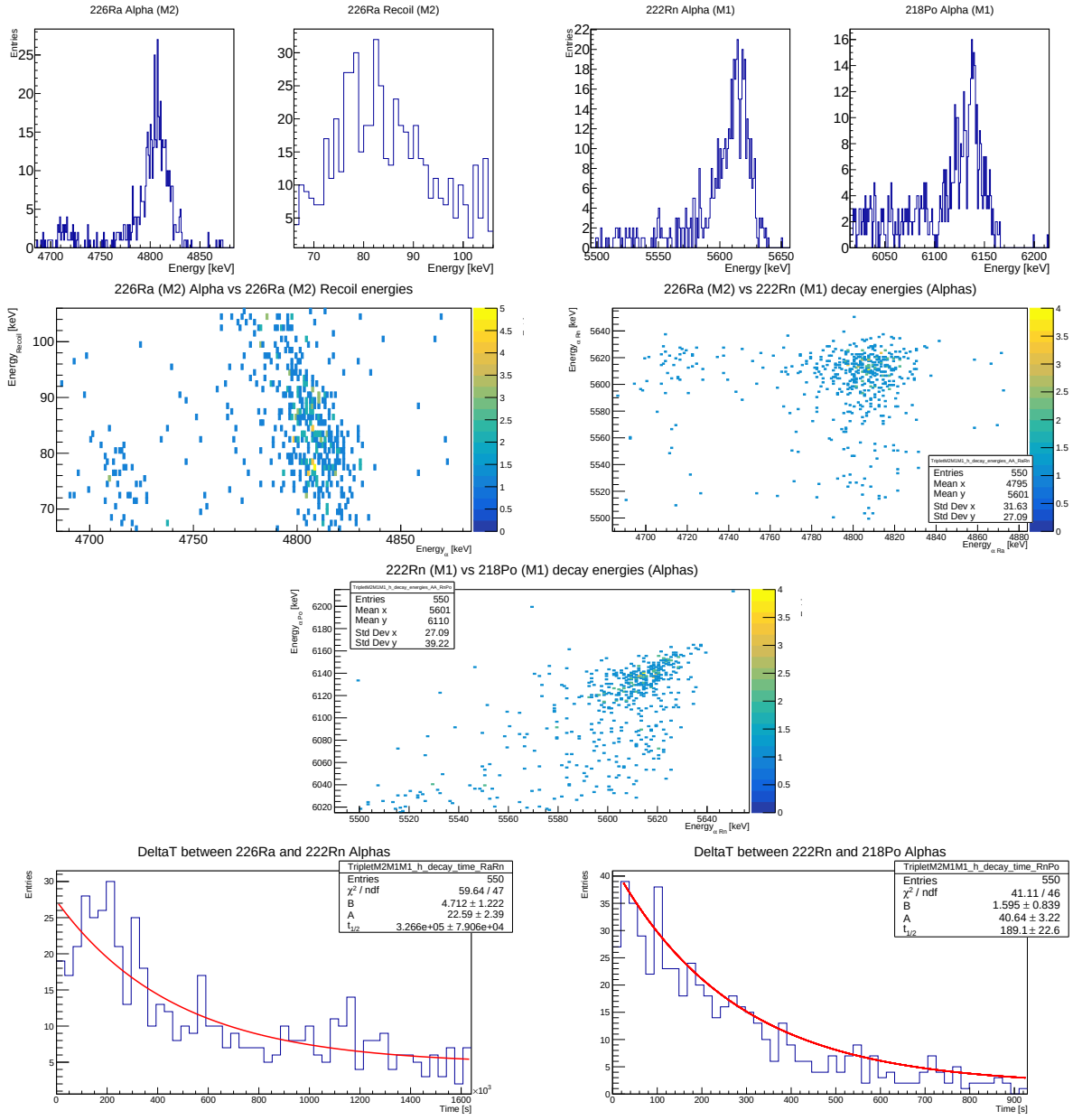

Figure 5.12: Results of $M2$-$M1$-$M1$ ^{226}Ra $\rightarrow$ ^{222}Rn $\rightarrow$ ^{218}Po DC search. The first row shows the energy distribution of the four events in the delayed coincidence, then the two dimensional distributions in the second and third rows allow a better understanding of the correlation between the events. Finally the last two plots reports the time difference distribution between the ^{226}Ra-^{222}Rn events (left) and ^{222}Rn-^{218}Po ones (right), notice how the two $t_{1/2}$ obtained from the exponential fits are compatible with their tabulated values $t_{1/2}(^{222}\text{Rn})$ and $t_{1/2}(^{218}\text{Po})$, also shown in Figure 5.1.

Chapter 6

Monte Carlo Simulations and Contamination Activity Results

The last part of this thesis is dedicated to the analysis of the simulated data and then, by combining the results of the DC searches with what is obtained from the analysis of Monte Carlo simulations, I will evaluate the specific activities of the contaminants of interests (^{238}U, ^{235}U and ^{232}Th).

6.1 Monte Carlo Simulations of the Decay Chains

The MC simulated data used for this analysis is obtained thanks to the two softwares *qshields* and *Ares* (see Section 4.2), with the first one being utilized to simulate precisely the events coming from bulk and surface contamination of thorium and uranium in the CUORE TeO_2 crystals. A total of six simulations were performed, two for each contaminant, one for a bulk contamination and one for a surface one. In CUORE, contamination are modeled with a depth distribution behaving as a decaying exponential with different decay constant. DC analysis is sensible to shallow contamination with a 10 nm decay constant and to very deep ones.
Then *Ares* handles the simulation outputs, so that the data will be as similar as possible to the CUORE real data. I reprocessed *Ares* output to explicitly have the same variables for each event as in the real data used for the DC searches and also to have the simulated data in the same format, for an easier analysis. Then the DC searches that I implemented for real data can be repeated on the simulated one to obtain the reconstruction efficiency for every considered DC signature.

First a very important distinction needs to be made: having two kinds of MC data, simulating a bulk or a surface contamination, it is important to appropriately apply the DC search to the proper set of simulated data. As an example an $M1$-$M1$ delayed coin-

cidence is more likely to be generated by a bulk contamination, since both events release their energy in a single crystal and so it needs to be searched in the bulk MC data; while a DC having one or more $M2$ events in the signature is more probable to be caused by a shallow contamination, therefore this kind of signatures should be searched instead in the MC data simulating a surface contamination.

6.1.1 Delayed Coincidence Search applied to Monte Carlo Data

The final goal of this work is to evaluate the specific activity, in Bq/cm^2 for surface contamination or Bq/kg for bulk ones, of the three main contaminants. The analysis of simulated data allows to extract the signature dependent reconstruction efficiency ε_R, defined as

$$\varepsilon_R = \frac{N_{DC}(\text{signature})}{N_{ev}(\text{DS})} \ , \tag{6.1}$$

where N_{DC} is the number of delayed coincidences found in the simulated data for a given signature and N_{ev} is the total number of events in the MC dataset in which the DC are searched.
The considered signatures are the same for which the real data analysis results are discussed in Chapter 5 and the conditions required on the events are also coherent with those applied to real data.
For each simulated signature the usual plots are obtained: the one dimensional energy distribution of the radiations involved in the decays together with the two dimensional one when relevant and the time difference distribution with the decaying exponential fit. As an example, Figure 6.1 shows the results of the $M1$-$M1$ ^{222}Rn $\rightarrow$ ^{218}Po DC search using the MC simulation of a bulk ^{238}U contamination. The exponential fit of the time difference distribution is applied to the MC only to evaluate the quality of the DC reconstruction and does not enter the evaluation of the contamination.

Before showing the results of Monte Carlo data DC analysis, Table 6.1 lists the total number of events in each simulation dataset together with the number of generated decay chains per datasets; the latter will be used in the following section for the direct evaluation of the specific activity uncertainties, while the former enters Eq. 6.1. Then Table 6.2 summarize the results of DC searches in the simulated data, by reporting the number of DC found N_{DC} and the value of ε_R for each signature, as defined in Eq. 6.1.

6.2 Results on the Specific Activity of the Contaminants

The last part of my thesis will be dedicated to the explanation of how to extract the specific activity of the contaminants from the results of the DC searches with both real

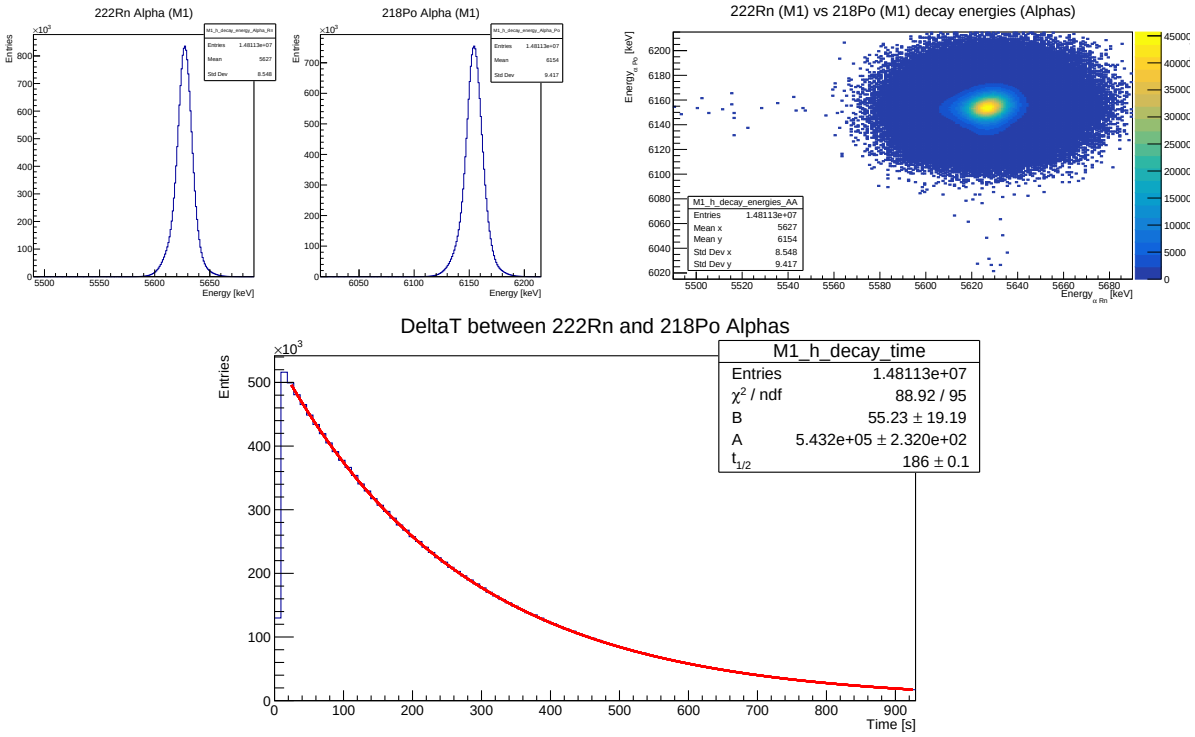

Figure 6.1: Example of DC search in simulated data for $M1$-$M1$ ^{222}Rn $\rightarrow$ ^{218}Po signature. From the time difference distribution, bottom plot, one can understand that the DC is very well reconstructed even in the simulated data.

Table 6.1: Number of generated chains and events for each type of contamination.

Contaminant	Type of Contamination	N_{chain} [$\times$ 10^7]	N_{ev} [$\times$ 10^7]
^{232}Th	Bulk	0.556	2.859
	Surface	1.111	6.335
^{235}U	Bulk	0.500	2.786
	Surface	0.500	2.783
^{238}U	Bulk	1.667	8.123
	Surface	1.667	7.997

Table 6.2: Results of DC analysis on MC simulated data. The first column exposes the type of simulated contamination, while the second and third defines the searched signature and the results of the analysis are shown in the last two columns. Notice that the enumeration of the $M1$-$M2$ ^{212}Bi $\rightarrow$ ^{208}Tl signatures follows their explanation in Section 5.2.1.

Contamination	Decay Sub-Chain	Signature	N_{DC}	ε_R
Bulk ^{232}Th	^{228}Th $\rightarrow$ ^{224}Ra	$M1$-$M1$	4770060	1.67×10^{-1}
Surf ^{232}Th	"	$M1$-$M2$	22676	3.58×10^{-4}
"	"	$M2$-$M1$	90854	1.43×10^{-3}
"	^{212}Pb $\rightarrow$ ^{212}Bi	$M2$-$M1$	30455	4.81×10^{-4}
"	^{212}Bi $\rightarrow$ ^{208}Tl	$M1$-$M3$	6047	9.55×10^{-5}
"	"	1^{st} $M1$-$M2$	17510	2.76×10^{-4}
"	"	2^{nd} $M1$-$M2$	17510	2.76×10^{-4}
"	"	3^{rd} $M1$-$M2$	17510	2.76×10^{-4}
Bulk ^{235}U	^{228}Th $\rightarrow$ ^{224}Ra	$M1$-$M1$	3372699	1.21×10^{-1}
Surf ^{235}U	"	$M2$-$M1$	49050	1.76×10^{-3}
Bulk ^{238}U	^{222}Rn $\rightarrow$ ^{218}Po	$M1$-$M1$	14811299	1.82×10^{-1}
Surf ^{238}U	"	$M1$-$M2$	1231304	1.54×10^{-2}
"	"	$M2$-$M1$	1143931	1.43×10^{-2}
"	"	$M2$-$M2$	584663	7.31×10^{-3}
Bulk ^{238}U	^{226}Ra $\rightarrow$ ^{222}Rn $\rightarrow$ ^{218}Po	$M1$-$M1$-$M1$	14497333	1.78×10^{-1}
Surf ^{238}U	"	$M2$-$M1$-$M1$	433077	5.42×10^{-3}
"	"	$M2$-$M2$-$M1$	245240	3.07×10^{-3}
"	"	$M2$-$M2$-$M2$	153405	1.92×10^{-3}

CUORE data and the simulated one. Then I will provide a comparison between the obtained results with the ones coming from past studies, such as material screening campaign (Table 4.1) and the CUORE-0 background model (Tables 4.2 and 4.3).

The specific activity of a contaminants is defined from the expression that connects the number of decays of interest $\mathcal{N}$ caused by the given contaminant, namely

$$\mathcal{N} = \mathcal{A} \cdot E \cdot \varepsilon_R \ , \tag{6.2}$$

where $\mathcal{A}$ is the specific activity measured in Bq/kg or Bq/cm^2, ε_R is the reconstruction efficiency obtained from MC data, while E is the exposure expressed in proper units: E needs to be in Total Detector Mass[kg]·yr if a bulk contamination is being evaluated, or in Total Detector Area[cm^2]·yr if a superficial one is being appraised instead. The two values E_B and E_S, for bulk and surface contamination evaluations respectively, are

$$E_B = 1038.4 \text{ kg} \cdot \text{yr} \quad , \quad E_S = \frac{E_B}{0.75 \text{ kg}} \cdot 6 \cdot 25 \text{ cm}^2 = 2.08 \times 10^5 \text{ cm}^2 \cdot \text{yr} \ , \tag{6.3}$$

where 0.75 kg and $6 \cdot 25$ cm^2 are the average mass and the total surface of each cubic TeO_2 crystal. Then by isolating $\mathcal{A}$ from Eq. 6.2, the specific activity can be written as

$$\mathcal{A}_{B,S} = \frac{\mathcal{N}}{E_{B,S} \cdot \varepsilon_R} \ , \tag{6.4}$$

where $\mathcal{N}$ can be identified as the A value obtained from the exponential fit of the time difference distribution for each searched delayed coincidence signature.

Table 6.3 summarize the results of both $\mathcal{A}_B$ and $\mathcal{A}_S$ evaluation for all the DC signatures searched in this work. The uncertainties are carefully evaluated by combining what is provided by the exponential fit of the time difference distributions with the binomially distributed ε_R. The results obtained for the ^{226}Ra $\rightarrow$ ^{222}Rn $\rightarrow$ ^{218}Po DC are derived by combining what is found from the two time difference fit, namely from the A and A' values reported in Table 5.3.
An important comment needs to be done, in this work the specific activities are evaluated assuming that all $M1$-$M1$ DC came from bulk contamination while the DC containing $M2$ events from surface ones. On the other hand, based on their depth distribution, surface contamination can also generate $M1$-$M1$ DC events. Then a subsequent step, not performed in the context of this thesis due to time constraints, is a bulk-surface combined analysis, that will provide more precise results.

A comparison between the specific activities evaluation from DC analysis with what has been obtained by previous research yields encouraging results for all types of contaminants. Some noteworthy results are:

- The ^{232}Th bulk contamination is a factor two lower than the known one and the measurement is more precise, while the surface contamination measurements are overall compatible with the CUORE-0 values.
- For the ^{235}U decay chain, these are the first measurements of this particular contaminant within the CUORE experiment, thus it is clear that additional studies must be carried out to refine these results.
- Lastly, for the ^{238}U bulk contamination I obtained a discrepancy between the one from the $^{222}\text{Rn} \rightarrow {}^{218}\text{Po}$ DC and the one from the triplet search; moreover they are not compatible with CUORE-0 BM results. Therefore in this case improvements in the DC analysis technique are required. Whereas the surface contamination measurements yielded an overall lower specific activity with respect to what was obtained by previous searches.

This suggests that a further refinement of such an analysis procedure for the characterization of natural radioactive contamination might lead to promising results; and highlights the possibility to extend it to other $0\nu\beta\beta$ decay experiments, such as the CUORE experiment upgrade, CUPID. Where DC analysis can be extended to superficial contamination of the copper holders, with a relevant impact on the evaluation of CUPID background budget. This is of course feasible only if MC simulations describing such contamination can be adequately implemented. Moreover, DC studies can be used to directly suppress the CUPID background, as it was done in CUPID-Mo [83].

Table 6.3: Summary of Specific Activity evaluation for each searched DC.

Contamination	Decay Sub-Chain	Signature	$\mathcal{A}_B$ [nBq/kg]	$\mathcal{A}_S$ [nBq/cm^2]
Bulk ^{232}Th	^{228}Th $\rightarrow$ ^{224}Ra	$M1$-$M1$	32.7 ± 0.9	
Surf ^{232}Th	"	$M1$-$M2$		1.1 ± 0.3
"	"	$M2$-$M1$		0.51 ± 0.07
"	^{212}Pb $\rightarrow$ ^{212}Bi	$M2$-$M1$		1.3 ± 0.2
"	^{212}Bi $\rightarrow$ ^{208}Tl	$M1$-$M3$		5.1 ± 0.9
"	"	1^{st} $M1$-$M2$		4.7 ± 0.8
"	"	2^{nd} $M1$-$M2$		4.8 ± 0.8
"	"	3^{rd} $M1$-$M2$		4.6 ± 0.8
Bulk ^{235}U	^{228}Th $\rightarrow$ ^{224}Ra	$M1$-$M1$	8.6 ± 0.9	
Surf ^{235}U	"	$M2$-$M1$		0.74 ± 0.01
Bulk ^{238}U	^{222}Rn $\rightarrow$ ^{218}Po	$M1$-$M1$	29.4 ± 0.8	
Surf ^{238}U	"	$M1$-$M2$		0.54 ± 0.03
"	"	$M2$-$M1$		0.33 ± 0.02
"	"	$M2$-$M2$		0.55 ± 0.06
Bulk ^{238}U	^{226}Ra $\rightarrow$ ^{222}Rn $\rightarrow$ ^{218}Po	$M1$-$M1$-$M1$	9.3 ± 0.5	
Surf ^{238}U	"	$M2$-$M1$-$M1$		0.89 ± 0.08
"	"	$M2$-$M2$-$M1$		0.23 ± 0.06
"	"	$M2$-$M2$-$M2$		0.36 ± 0.09

Conclusions

This thesis presents an evaluation of surface and bulk contamination of the TeO_2 crystals employed by the CUORE experiment with a delayed coincidence approach. The studied contamination, namely the ones from ^{238}U, ^{235}U and ^{232}Th, are investigated by looking into the 1 ton·yr CUORE data for events that can be identified as coming from particular decay sub-chains of the cited above nuclei.
To find events in delayed coincidence correctly associated with a decay chain, various constraints on single event properties must be applied, such as: multiplicity selections, cuts on the energy released and where is detected within the CUORE detector geometry and, most importantly, on the time at which the events are identified. The decays related to each contaminant can consist of different emissions (α, β or γ) with various energies and a single decay can also cause more than one energy deposition. Therefore even within the same pair or triplets of events in coincidence many signatures can be searched.

After selecting the events in delayed coincidence in the CUORE data, I studied their energy and time difference distribution. Through an exponentially decreasing fit of this latter distribution, the half-life of the daughter nucleus in the coincidence is extracted and compared with its tabulated value with the intention of verifying if the coincidence has been well reconstructed. Moreover, I applied the delayed coincidence search to Monte Carlo data simulating the expected effect of precise bulk and superficial contamination on the CUORE tellurium detectors to obtain the geometrical efficiency of each signature. By combining the results of the studies on the two types of data I was able to obtain an evaluation of Th and U activities ranging from 10^{-1} to 10^{1} nBq, which some are in agreement with previous results from material screening campaign and from the CUORE-0 experiment background model, while others highlights that a more refined analysis is required.
This is the first time that delayed coincidence analysis is carried out using the real CUORE data and, while providing promising results, it offers a solid starting point for additional research activities. The possible following steps consist of: a bulk-surface combined analysis, the introduction in the specific activities evaluation of the reconstruction efficiency in a channel dependent way and the consideration of the systematics on the depth distribution for surface contamination.

Appendix A

^{232}Th Decay Chain DC Analysis Additional Results

A.1 ^{228}Th $\rightarrow$ ^{224}Ra Results

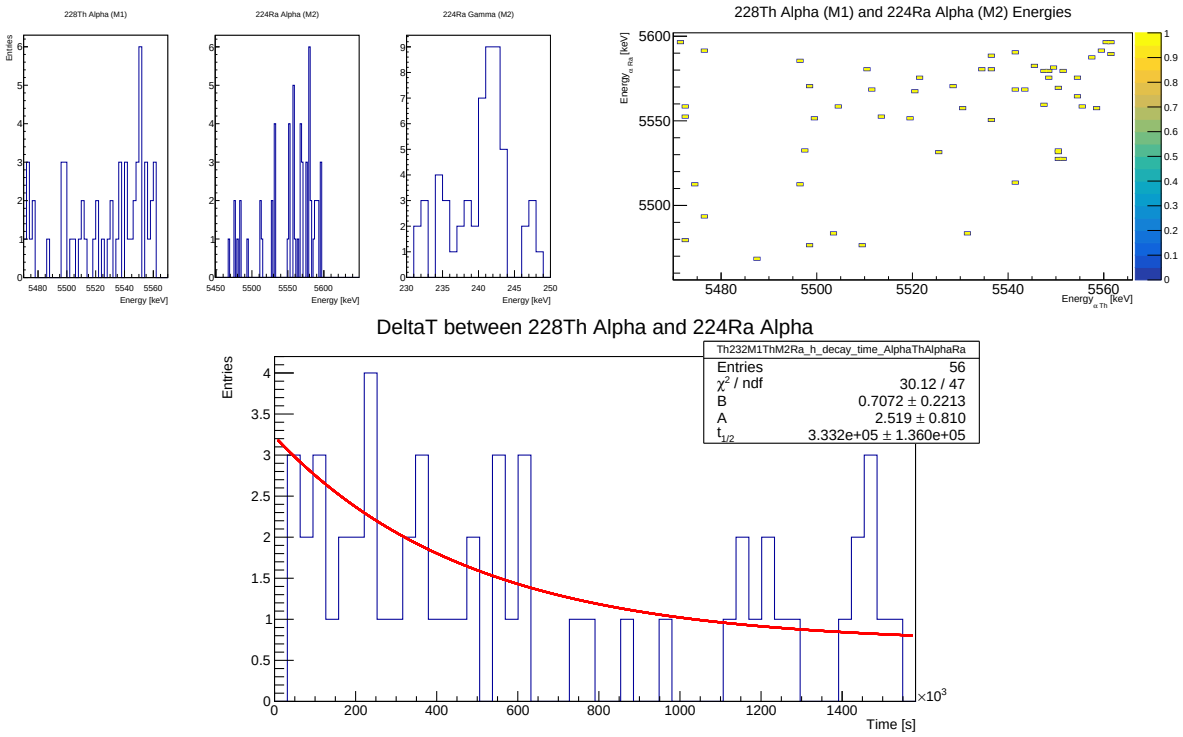

Figure A.1: Results of $M1$-$M2$ ^{228}Th $\rightarrow$ ^{224}Ra DC search. Top left/right: one/two dimensional energy distribution. Bottom: time difference distribution fitted with Eq. 5.1.

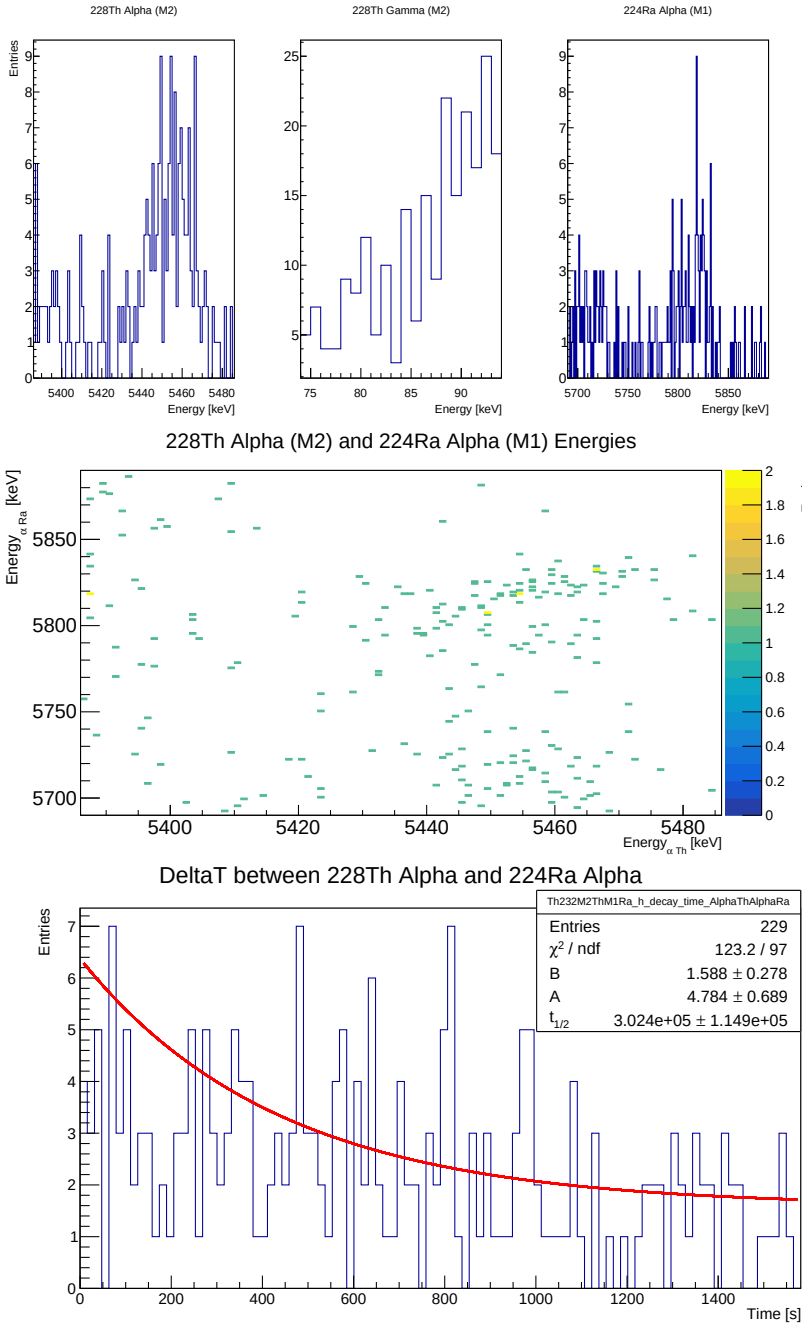

Figure A.2: Results of $M2$-$M1$ ^{228}Th $\rightarrow$ ^{224}Ra DC search.

A.2 ^{212}Pb $\rightarrow$ ^{212}Bi Results

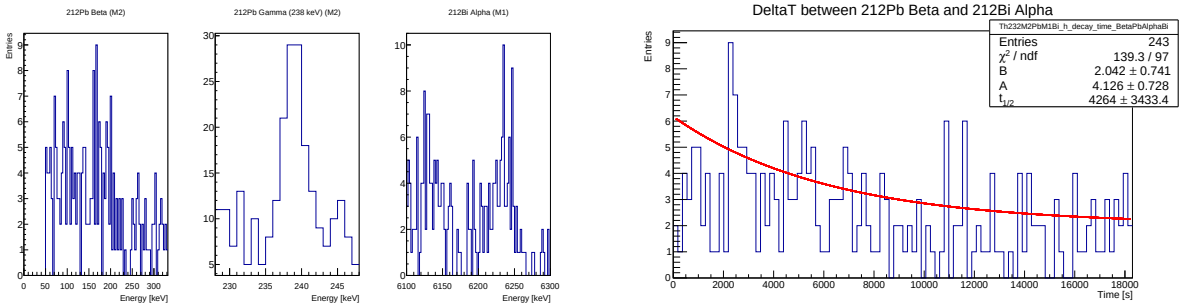

Figure A.3: Results of $M2$-$M1$ ^{212}Pb $\rightarrow$ ^{212}Bi DC search.

A.3 ^{212}Bi $\rightarrow$ ^{208}Tl Results

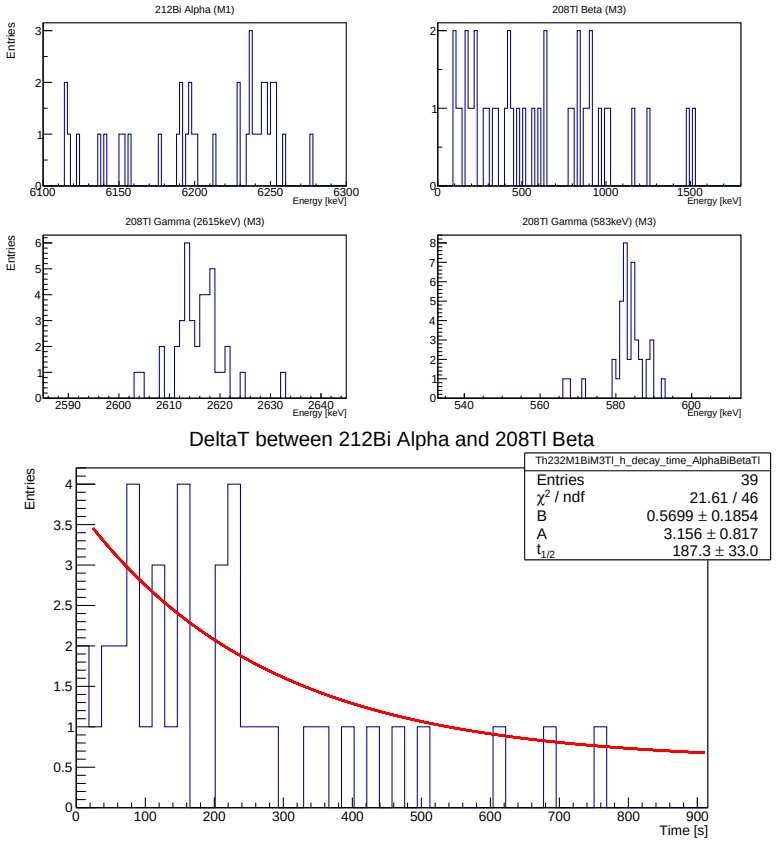

Figure A.4: Results of $M1$-$M3$ ^{212}Bi $\rightarrow$ ^{208}Tl DC search. Considering the 2615 keV and the 583 keV γ emissions, together with the β from the ^{208}Tl decay.

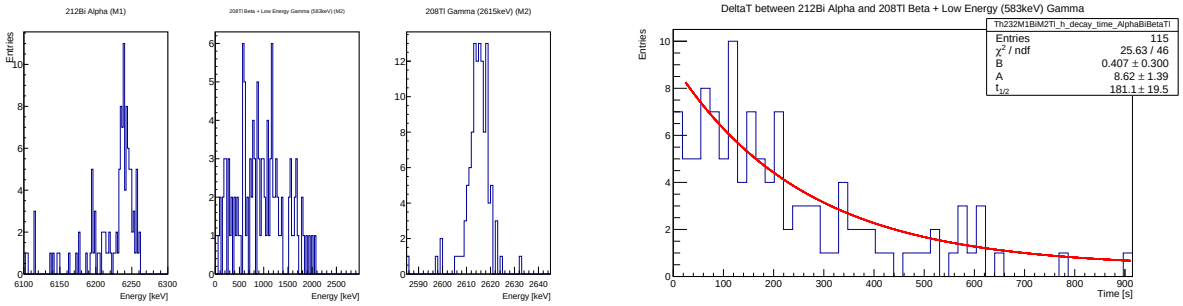

Figure A.5: Results of $M1$-$M2$ ^{212}Bi $\rightarrow$ ^{208}Tl DC search. Considering the $M2$ ^{208}Tl event as a β decay with the emission of 583 keV γ in the same channel and the 2615 keV photon.

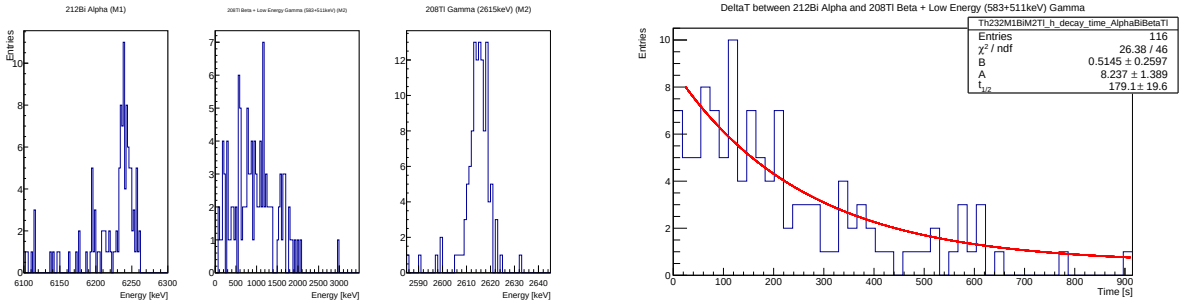

Figure A.6: Results of $M1$-$M2$ ^{212}Bi $\rightarrow$ ^{208}Tl DC search. Considering the $M2$ ^{208}Tl event as a β decay with the emission of low energy (511 and 583 keV) γs in the same channel and the 2615 keV photon.

Appendix B

^{235}U Decay Chain DC Analysis Additional Results

B.1 ^{227}Th $\rightarrow$ ^{223}Ra Results

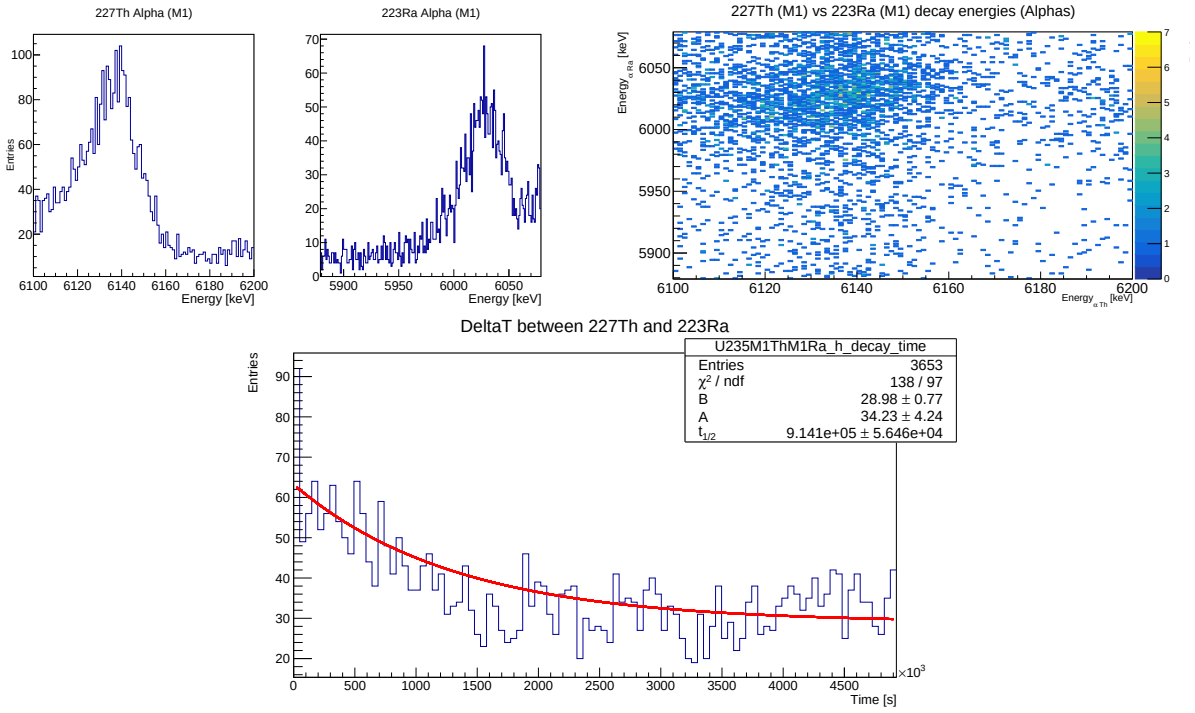

Figure B.1: Results of $M1$-$M1$ ^{227}Th $\rightarrow$ ^{223}Ra DC search. The top left plot shows the one dimensional energy distribution of the two events around their respective Q-value and the top right the two dimensional one. While the bottom plot reports the time difference distribution fitted with the usual decaying exponential function.

Appendix C

^{238}U Decay Chain DC Analysis Additional Results

C.1 ^{222}Rn $\rightarrow$ ^{218}Po Results

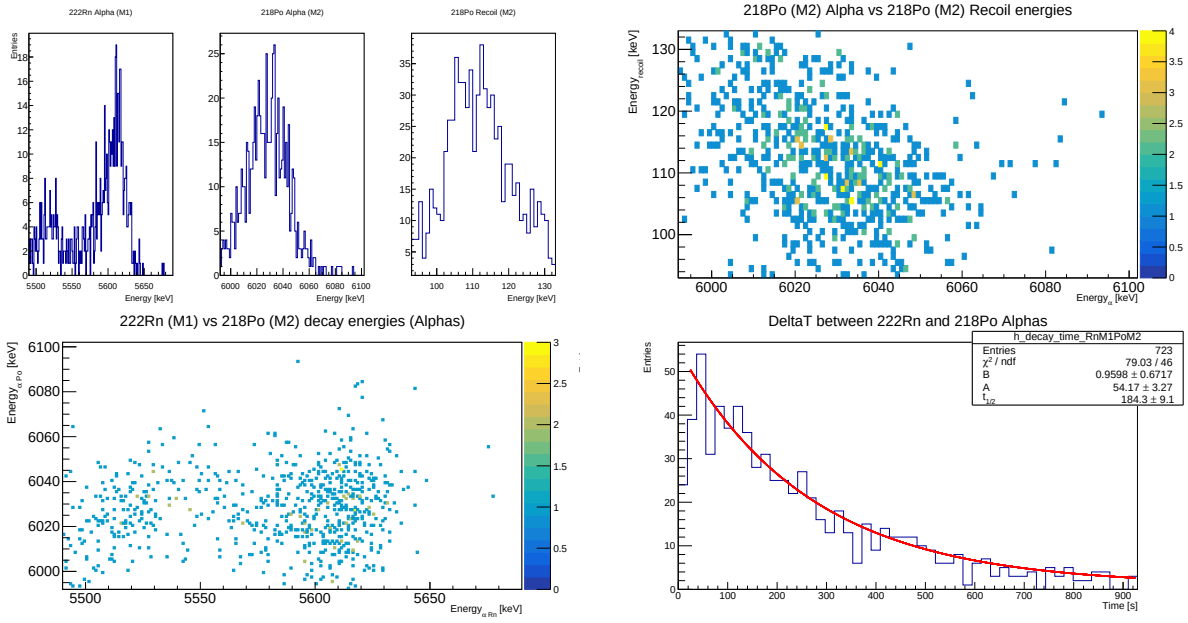

Figure C.1: Results of $M1$-$M2$ ^{222}Rn $\rightarrow$ ^{218}Po DC search.

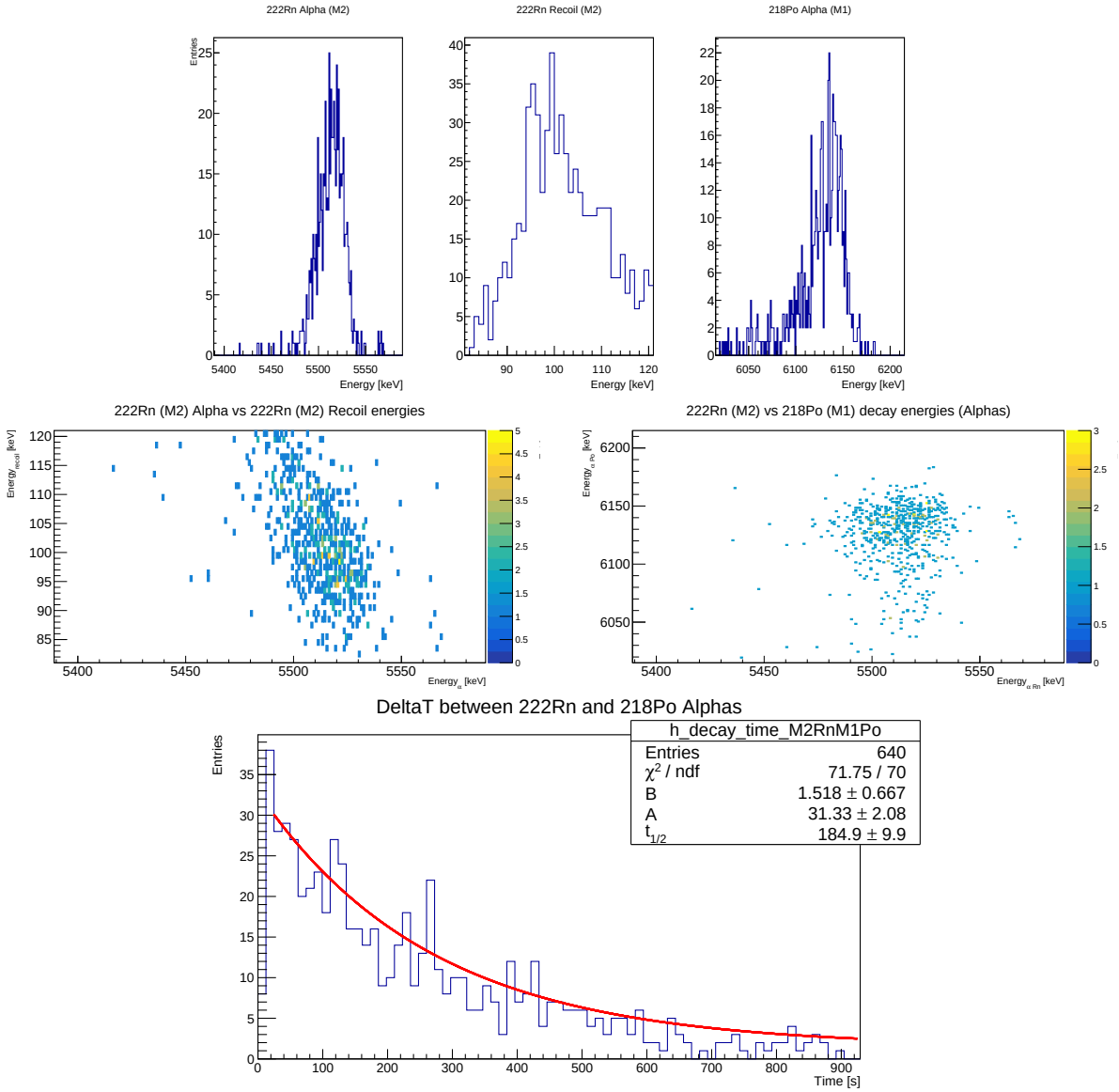

Figure C.2: Results of $M2$-$M1$ ^{222}Rn $\rightarrow$ ^{218}Po DC search.

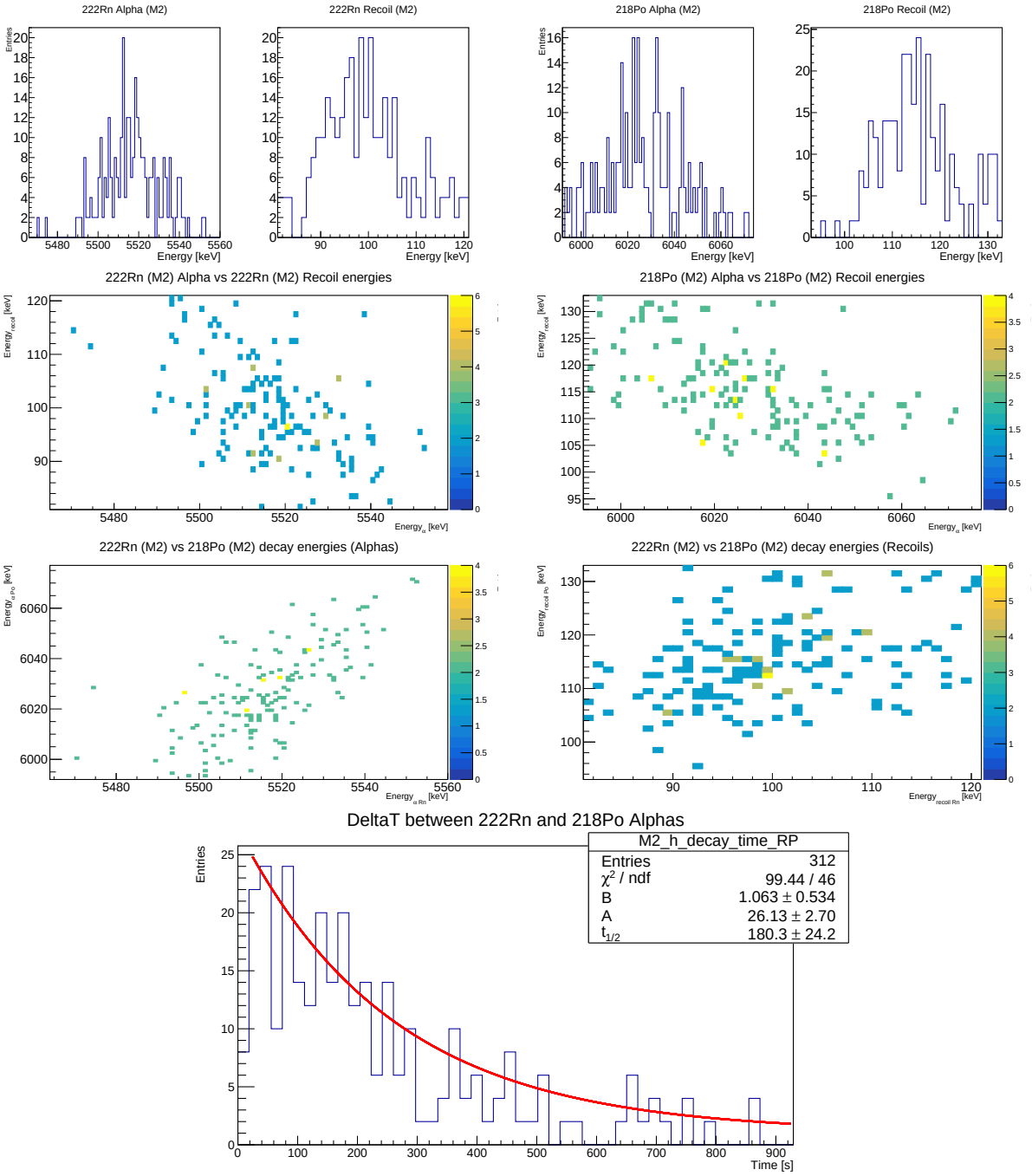

Figure C.3: Results of $M2$-$M2$ ^{222}Rn $\rightarrow$ ^{218}Po DC search.

C.2 ^{226}Ra $\rightarrow$ ^{222}Rn $\rightarrow$ ^{218}Po Results

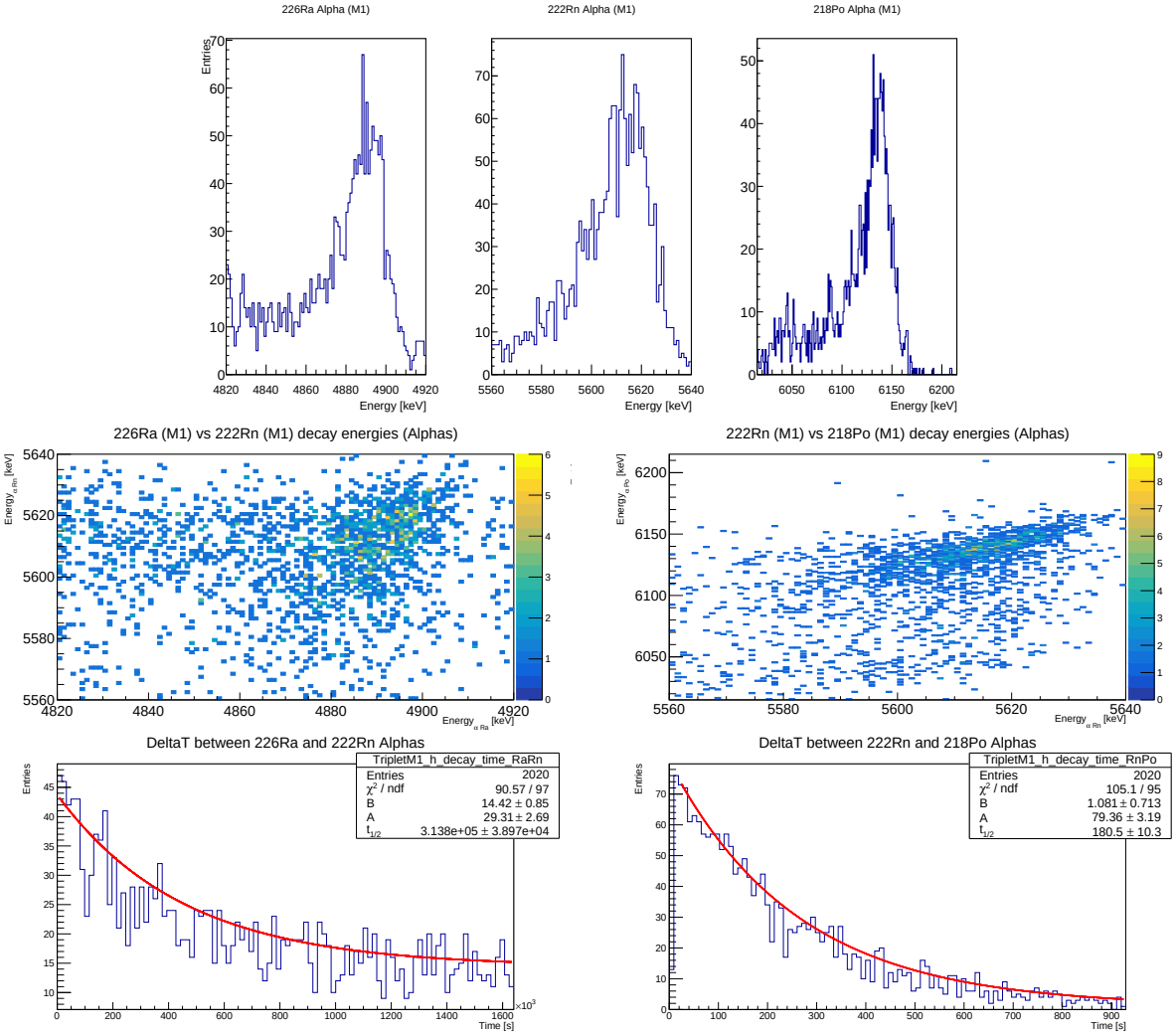

Figure C.4: Results of $M1$-$M1$-$M1$ ^{226}Ra $\rightarrow$ ^{222}Rn $\rightarrow$ ^{218}Po DC search.

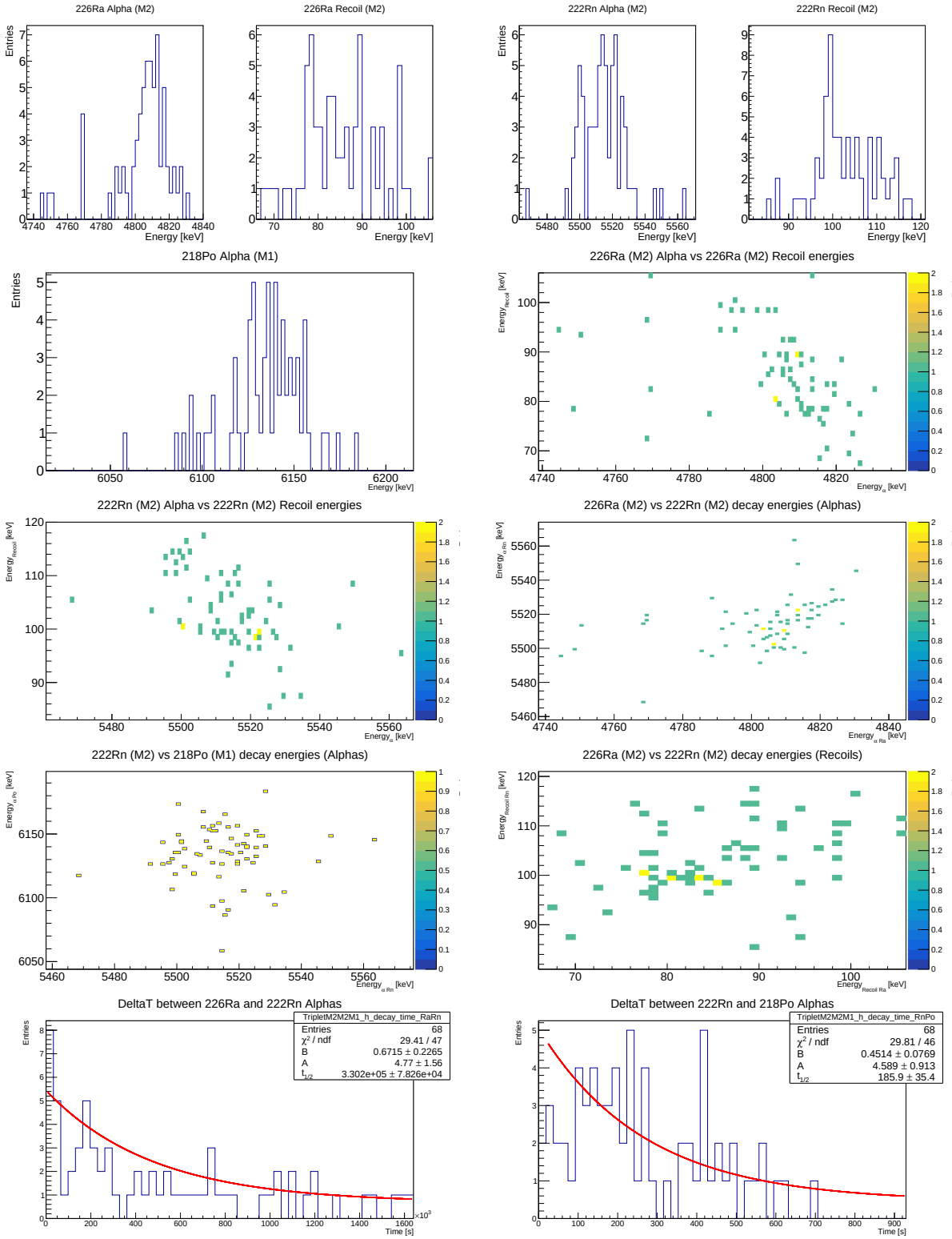

Figure C.5: Results of $M2$-$M2$-$M1$ ^{226}Ra $\rightarrow$ ^{222}Rn $\rightarrow$ ^{218}Po DC search.

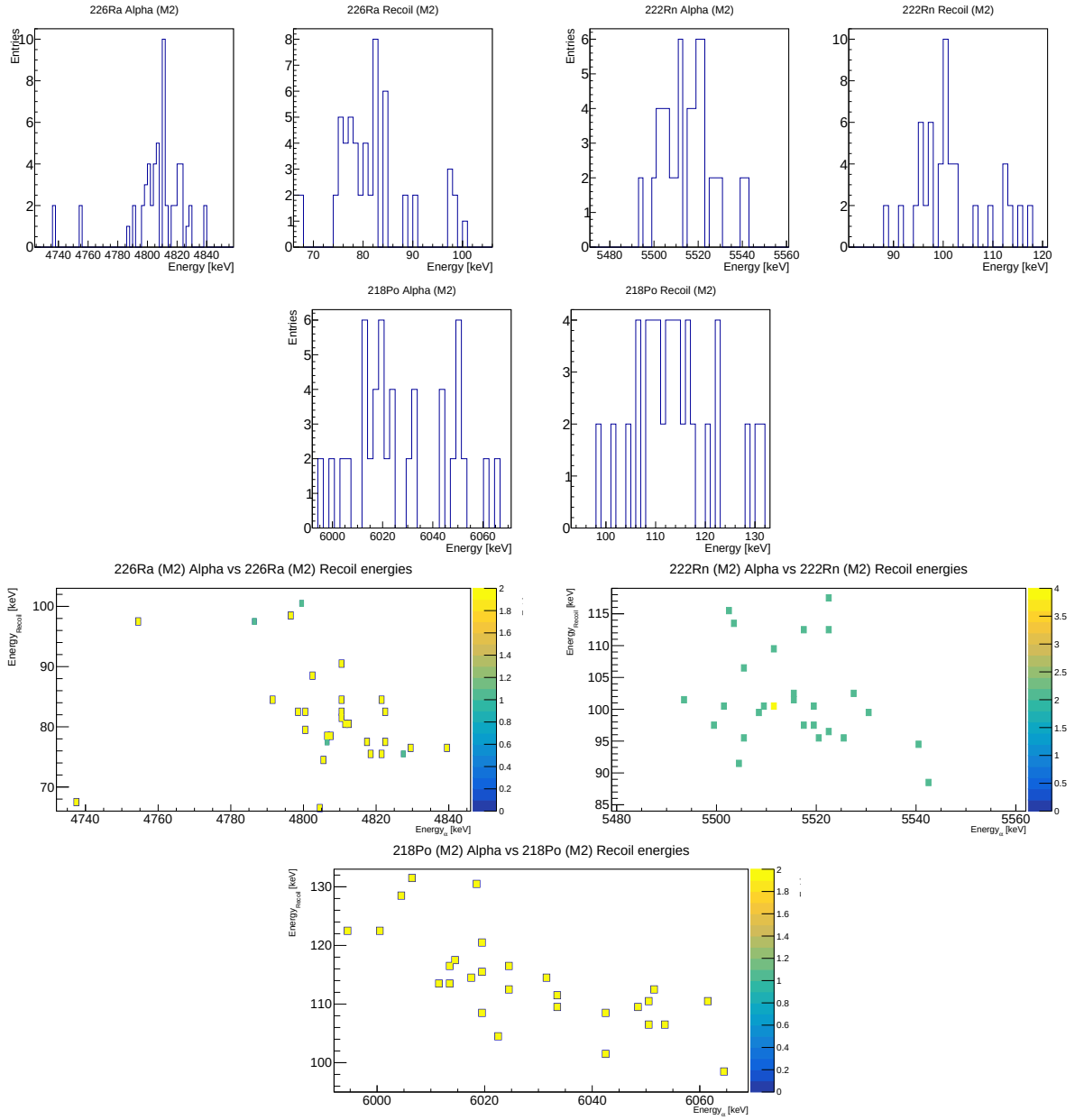

Figure C.6: First part of the results of $M2$-$M2$-$M2$ ^{226}Ra $\rightarrow$ ^{222}Rn $\rightarrow$ ^{218}Po DC search.

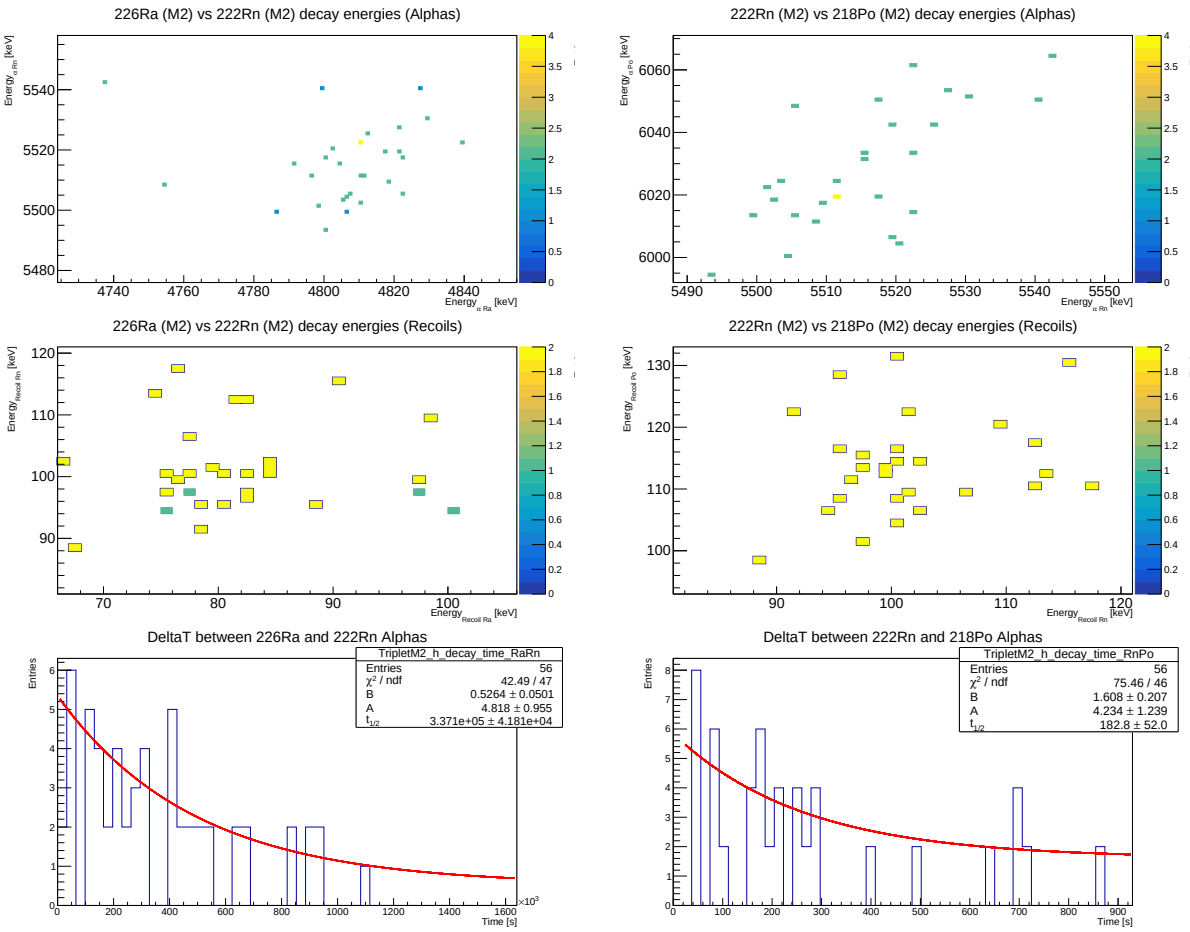

Figure C.7: Second part of the results of $M2$-$M2$-$M2$ ^{226}Ra $\rightarrow$ ^{222}Rn $\rightarrow$ ^{218}Po DC search.

List of Abbreviations

$0\nu\beta\beta$	Neutrinoless Double Beta Decay
$2\nu\beta\beta$	Two Neutrino Double Beta Decay
ANPS	Average Noise Power Spectrum
AP	Average Pulse
BEGe	Broad Energy Ge Detectors
BEH	Brout-Englert-Higgs
BI	Background Index
BM	Background Model
CL	Confidence Level
CP	Charge Parity
CUORE	Cryogenic Underground Observatory for Rare Events
DAQ	Data AQuisition
DC	Delayed Coincidences
DS	Detector Suspensions
DT	Derivative Trigger
DU	Dilution Unit
ELS	External Lead Shield
FCS	Fast Cooling System
FE	Front End

INFN	Istituto Nazionale di Fisica Nucleare
IO	Inverted Ordering
IVC	Inner Vacuum Chamber
JAGS	Just Another Gibbs Sampler
LH	Left-Handed
LNGS	Laboratori Nazionali del Gran Sasso
LS	Liquid Scintillator
MC	Monte Carlo
MCMC	Markov Chain Monte Carlo
MLS	Modern Lead Shield
MSP	Main Support Plate
NO	Normal Ordering
NTD-Ge	Neutron Transmutation Doped Germanium
OF	Optimum Filter
OFE	Oxygen-Free Electrolytic
OT	Optimum Trigger
OVC	Outer Vacuum Chamber
PCA	Principal Component Analysis
PGA	Programmable Gain Amplifiers
PMNS	Pontecorvo-Maki-Nakagawa-Sakata
PMT	Photo Multiplier Tubes
PSA	Pulse Shape Analysis
PTFE	PoliTetraFluoroEthilene
PTs	Pulse Tube
QD	Quasi Degenerate

RE	Reconstruction Error
RH	Right-Handed
RLS	Roman Lead Shield
RMS	Root Mean Square
ROC	Read-Out Chain
ROI	Region Of Interest
SM	Standard Model
SNR	Signal to Noise Ratio
TGS	Thermal Gain Stabilization

Bibliography

[1] C. L. Cowan, F. Reines, F. B. Harrison, H. W. Kruse, and A. D. McGuire, "Detection of the Free Neutrino: a Confirmation," *Science*, vol. 124, no. 3212, pp. 103–104, 1956. [Online]. Available: https://www.science.org/doi/abs/10.1126/science.124.3212.103

[2] G. Danby, J.-M. Gaillard, K. Goulianos, L. M. Lederman, N. Mistry, M. Schwartz, and J. Steinberger, "Observation of High-Energy Neutrino Reactions and the Existence of Two Kinds of Neutrinos," *Phys. Rev. Lett.*, vol. 9, pp. 36–44, Jul 1962. [Online]. Available: https://link.aps.org/doi/10.1103/PhysRevLett.9.36

[3] K. Kodama, N. Ushida, C. Andreopoulos, N. Saoulidou, G. Tzanakos, P. Yager, and B. B. et al, "Observation of tau neutrino interactions," *Physics Letters B*, vol. 504, no. 3, pp. 218–224, 2001. [Online]. Available: https://www.sciencedirect.com/science/article/pii/S0370269301003070

[4] A. B. McDonald, "The Sudbury Neutrino Observatory: observation of flavor change for solar neutrinos," *Annalen der Physik*, vol. 528, no. 6, pp. 469–480, 2016.

[5] T. Kajita, "Nobel Lecture: Discovery of atmospheric neutrino oscillations," *Reviews of Modern Physics*, vol. 88, no. 3, p. 030501, 2016.

[6] Z. Maki, M. Nakagawa, and S. Sakata, "Remarks on the Unified Model of Elementary Particles," *Progress of Theoretical Physics*, vol. 28, no. 5, pp. 870–880, 11 1962. [Online]. Available: https://doi.org/10.1143/PTP.28.870

[7] S. Bilenky, J. Hosek, and S. Petcov, "On oscillations of neutrinos with Dirac and Majorana masses," *Phys. Lett. B*, vol. 94, p. 495, 1980.

[8] K. Nakamura, S. Petcov *et al.*, "Neutrino masses, mixing, and oscillations," 2018.

[9] E. Majorana, "Teoria simmetrica dell'elettrone e del positrone," *Il Nuovo Cimento (1924-1942)*, vol. 14, no. 4, pp. 171–184, 1937.

[10] I. Esteban, M. Gonzalez-Garcia, M. Maltoni, T. Schwetz, and A. Zhou, "The fate of hints: updated global analysis of three-flavor neutrino oscillations,"

Journal of High Energy Physics, vol. 2020, no. 9, Sep 2020. [Online]. Available: http://dx.doi.org/10.1007/JHEP09(2020)178

[11] "NuFIT 5.1," vol. 2021. [Online]. Available: www.nu-fit.org

[12] R. N. Mohapatra and G. Senjanović, "Neutrino mass and spontaneous parity nonconservation," *Physical Review Letters*, vol. 44, no. 14, p. 912, 1980.

[13] S. Dell'Oro, S. Marcocci, M. Viel, and F. Vissani, "Neutrinoless double beta decay: 2015 review," *Advances in High Energy Physics*, vol. 2016, 2016.

[14] S. Bilenky and C. Giunti, "Neutrinoless double-beta decay: a probe of physics beyond the standard model," *International Journal of Modern Physics A*, vol. 30, no. 04n05, p. 1530001, 2015.

[15] J. Engel and J. Menéndez, "Status and future of nuclear matrix elements for neutrinoless double-beta decay: a review," *Reports on Progress in Physics*, vol. 80, no. 4, p. 046301, 2017.

[16] C. Giganti, S. Lavignac, and M. Zito, "Neutrino oscillations: the rise of the PMNS paradigm," *Progress in Particle and Nuclear Physics*, vol. 98, pp. 1–54, 2018.

[17] F. Capozzi, G. Fogli, E. Lisi, A. Marrone, D. Montanino, and A. Palazzo, "Status of three-neutrino oscillation parameters," *Physical Review D*, vol. 89, no. 9, p. 093018, 2014.

[18] P. Collaboration, Y. Akrami, F. Arroja, M. Ashdown, J. Aumont, C. Baccigalupi, M. Ballardini, A. Banday, R. Barreiro, N. Bartolo *et al.*, "Planck 2018 results. I. Overview and the cosmological legacy of Planck," 2020.

[19] C. Giunti, M. Laveder, Y. Li, and H. Long, "Pragmatic view of short-baseline neutrino oscillations," *Physical Review D*, vol. 88, no. 7, p. 073008, 2013.

[20] P. D. Group *et al.*, "Review of particle physics," *Progress of Theoretical and Experimental Physics*, vol. 2020, no. 8, pp. 1–2093, 2020.

[21] G. Drexlin, V. Hannen, S. Mertens, and C. Weinheimer, "Current direct neutrino mass experiments," *Advances in High Energy Physics*, vol. 2013, 2013.

[22] M. Aker, A. Beglarian, J. Behrens, A. Berlev, U. Besserer, B. Bieringer, F. Block, S. Bobien, M. Böttcher, B. Bornschein *et al.*, "Direct neutrino-mass measurement with sub-electronvolt sensitivity," *Nature Physics*, vol. 18, no. 2, pp. 160–166, 2022.

[23] C. Kraus, B. Bornschein, L. Bornschein, J. Bonn, B. Flatt, A. Kovalik, B. Ostrick, E. Otten, J. Schall, T. Thümmler *et al.*, "Final results from phase II of the Mainz neutrino mass searchin tritium beta decay," *The European Physical Journal C-Particles and Fields*, vol. 40, no. 4, pp. 447–468, 2005.

[24] V. Aseev, A. Belesev, A. Berlev, E. Geraskin, A. Golubev, N. Likhovid, V. Lobashev, A. Nozik, V. Pantuev, V. Parfenov *et al.*, "Upper limit on the electron antineutrino mass from the Troitsk experiment," *Physical Review D*, vol. 84, no. 11, p. 112003, 2011.

[25] M. Agostini, G. Benato, J. A. Detwiler, J. Menéndez, and F. Vissani, "Toward the discovery of matter creation with neutrinoless double-beta decay," *arXiv preprint arXiv:2202.01787*, 2022.

[26] M. Berglund and M. E. Wieser, "Isotopic compositions of the elements (IUPAC Technical Report)," *Pure and applied chemistry*, vol. 83, no. 2, pp. 397–410, 2011.

[27] A. Kwiatkowski, T. Brunner, J. Holt, A. Chaudhuri, U. Chowdhury, M. Eibach, J. Engel, A. Gallant, A. Grossheim, M. Horoi *et al.*, "New determination of double-β-decay properties in ^{48}Ca: High-precision Q$\beta\beta$-value measurement and improved nuclear matrix element calculations," *Physical Review C*, vol. 89, no. 4, p. 045502, 2014.

[28] S. Rahaman, V.-V. Elomaa, T. Eronen, J. Hakala, A. Jokinen, J. Julin, A. Kankainen, A. Saastamoinen, J. Suhonen, C. Weber *et al.*, "Q values of the ^{76}Ge and ^{100}Mo double-beta decays," *Physics Letters B*, vol. 662, no. 2, pp. 111–116, 2008.

[29] D. L. Lincoln, J. D. Holt, G. Bollen, M. Brodeur, S. Bustabad, J. Engel, S. J. Novario, M. Redshaw, R. Ringle, and S. Schwarz, "First Direct Double-β Decay Q-Value Measurement of ^{82}Se in Support of Understanding the Nature of the Neutrino"," *Physical review letters*, vol. 110, no. 1, p. 012501, 2013.

[30] M. Alanssari, D. Frekers, T. Eronen, L. Canete, J. Dilling, M. Haaranen, J. Hakala, M. Holl, M. Ješkovskỳ, A. Jokinen *et al.*, "Single and Double Beta-Decay Q Values among the Triplet ^{96}Zr, ^{96}Nb, and ^{96}Mo," *Physical review letters*, vol. 116, no. 7, p. 072501, 2016.

[31] S. Rahaman, V.-V. Elomaa, T. Eronen, J. Hakala, A. Jokinen, A. Kankainen, J. Rissanen, J. Suhonen, C. Weber, and J. Äystö, "Double-beta decay Q values of ^{116}Cd and ^{130}Te," *Physics Letters B*, vol. 703, no. 4, pp. 412–416, 2011.

[32] M. Redshaw, E. Wingfield, J. McDaniel, and E. G. Myers, "Mass and Double-Beta-Decay Q Value of ^{136}Xe," *Physical review letters*, vol. 98, no. 5, p. 053003, 2007.

[33] M. Agostini, A. Bakalyarov, M. Balata, I. Barabanov, L. Baudis, C. Bauer, E. Bellotti, S. Belogurov, A. Bettini, L. Bezrukov *et al.*, "Improved limit on neutrinoless double-β decay of ^{76}Ge from GERDA phase II," *Physical review letters*, vol. 120, no. 13, p. 132503, 2018.

[34] M. Agostini, A. Bakalyarov, M. Balata, I. Barabanov, L. Baudis, C. Bauer, E. Bellotti, S. Belogurov, S. Belyaev, G. Benato *et al.*, "Upgrade for Phase II of the Gerda experiment," *The European Physical Journal C*, vol. 78, no. 5, pp. 1–30, 2018.

[35] C. Macolino and G. Collaboration, "Results on neutrinoless double-beta decay from GERDA phase I," *Modern Physics Letters A*, vol. 29, no. 01, p. 1430001, 2014.

[36] S. Alvis, I. Arnquist, F. Avignone III, A. Barabash, C. Barton, V. Basu, F. Bertrand, B. Bos, M. Busch, M. Buuck *et al.*, "Search for neutrinoless double-β decay in ^{76}Ge with 26 kg yr of exposure from the Majorana Demonstrator," *Physical Review C*, vol. 100, no. 2, p. 025501, 2019.

[37] A. J. Zsigmond, L. Collaboration *et al.*, "LEGEND: The future of neutrinoless double-beta decay search with germanium detectors," in *Journal of Physics: Conference Series*, vol. 1468, no. 1. IOP Publishing, 2020, p. 012111.

[38] J. S. and, "Results and future plans for the KamLAND-Zen experiment," *Journal of Physics: Conference Series*, vol. 888, p. 012031, sep 2017. [Online]. Available: https://doi.org/10.1088/1742-6596/888/1/012031

[39] Z. Collaboration *et al.*, "First Search for the Majorana Nature of Neutrinos in the Inverted Mass Ordering Region with KamLAND-Zen," *arXiv preprint arXiv:2203.02139*, 2022.

[40] M. Endo, K. Hamaguchi, M. Ibe, T. Ishibashi, A. Ishikawa, M. Ishino, M. Ishitsuka, S. Kanemura, M. Kuriki, T. Mori *et al.*, "Japan's Strategy for Future Projects in High Energy Physics," *arXiv preprint arXiv:2203.13979*, 2022.

[41] E. Andreotti, C. Arnaboldi, F. Avignone III, M. Balata, I. Bandac, M. Barucci, J. Beeman, F. Bellini, C. Brofferio, A. Bryant *et al.*, "^{130}Te neutrinoless double-beta decay with CUORICINO," *Astroparticle Physics*, vol. 34, no. 11, pp. 822–831, 2011.

[42] C. Alduino, K. Alfonso, D. Artusa, F. Avignone, O. Azzolini, T. Banks, G. Bari, J. Beeman, F. Bellini, A. Bersani *et al.*, "Measurement of the two-neutrino double-beta decay half-life of ^{130}Te with the CUORE-0 experiment," *The European Physical Journal C*, vol. 77, no. 1, pp. 1–18, 2017.

[43] D. Artusa, F. Avignone, O. Azzolini, M. Balata, T. Banks, G. Bari, J. Beeman, F. Bellini, A. Bersani, M. Biassoni *et al.*, "Searching for neutrinoless double-beta decay of ^{130}Te with CUORE," *Advances in High Energy Physics*, vol. 2015, 2014.

[44] L. Cononica, L. Gladstone, E. Hansen, A. F. Leder, J. L. Ouellet, and L. Winslow, "CUORE sensitivity to $0\nu\beta\beta$ decay," *Eur. Phys. J.*, 2017.

[45] A. Alessandrello, C. Brofferio, D. Camin, O. Cremonesi, E. Fiorini, A. Giuliani, G. Pessina, and E. Previtali, "The first underground low radioactivity bolometric system," *Low temperature Detectors for Neutrinos and Dark Matter III*, pp. 253–262, 1990.

[46] E. Fiorini and T. Niinikoski, "Low-temperature calorimetry for rare decays," *Nuclear Instruments and Methods in Physics Research*, vol. 224, no. 1-2, pp. 83–88, 1984.

[47] C. Arnaboldi, C. Brofferio, A. Bryant, C. Bucci, L. Canonica, S. Capelli, M. Carrettoni, M. Clemenza, I. Dafinei, S. Di Domizio *et al.*, "Production of high purity TeO_2 single crystals for the study of neutrinoless double beta decay," *Journal of Crystal Growth*, vol. 312, no. 20, pp. 2999–3008, 2010.

[48] M. Barucci, C. Brofferio, A. Giuliani, E. Gottardi, I. Peroni, and G. Ventura, "Measurement of low temperature specific heat of crystalline TeO_2 for the optimization of bolometric detectors," *Journal of Low Temperature Physics*, vol. 123, no. 5, pp. 303–314, 2001.

[49] G. White, S. Collocott, and J. Collins, "Thermal properties of paratellurite (TeO_2) at low temperatures," *Journal of Physics: Condensed Matter*, vol. 2, no. 37, p. 7715, 1990.

[50] D. Q. Adams *et al.*, "Search for Majorana neutrinos exploiting millikelvin cryogenics with CUORE," *Nature*, vol. 604, no. 7904, pp. 53–58, 2022.

[51] C. Alduino, K. Alfonso, D. Artusa, F. Avignone III, O. Azzolini, M. Balata, T. Banks, G. Bari, J. Beeman, F. Bellini *et al.*, "CUORE-0 detector: design, construction and operation," *Journal of Instrumentation*, vol. 11, no. 07, p. P07009, 2016.

[52] A. Drobizhev, C. Collaboration *et al.*, "The Research, Development, and Production of Neutron Transmutation Doped Germanium Thermistors for the CUPID Experiment." in *APS Division of Nuclear Physics Meeting Abstracts*, vol. 2021, 2021, pp. MB–003.

[53] C. Alduino, F. Alessandria, M. Balata, D. Biare, M. Biassoni, C. Bucci, A. Caminata, L. Canonica, L. Cappelli, G. Ceruti *et al.*, "The CUORE cryostat: An infrastructure for rare event searches at millikelvin temperatures," *Cryogenics*, vol. 102, pp. 9–21, 2019.

[54] M. Schwark, F. Pobell, W. Halperin, C. Buchal, J. Hanssen, M. Kubota, and R. Mueller, "Ortho-para conversion of hydrogen in copper as origin of time-dependent heat leaks," *Journal of low temperature physics*, vol. 53, no. 5, pp. 685–694, 1983.

[55] C. E. Pagliarone, L. Cappelli, C. Bucci, P. Gorla, D. Damiano, F. Marignetti, G. Erme, and S. Kartal, "The CUORE fast cooling system," in *Proceedings of the European Physical Society Conference on High Energy Physics*, 2017, p. 634.

[56] A. D'Addabbo, C. Bucci, L. Canonica, S. Di Domizio, P. Gorla, L. Marini, A. Nucciotti, I. Nutini, C. Rusconi, and B. Welliver, "An active noise cancellation technique for the CUORE Pulse Tube Cryocoolers," *Cryogenics*, vol. 93, pp. 56–65, 2018.

[57] F. Pobell, *Matter and methods at low temperatures*. Springer, 2007, vol. 2.

[58] L. Pattavina, J. Beeman, M. Clemenza, O. Cremonesi, E. Fiorini, L. Pagnanini, S. Pirro, C. Rusconi, and K. Schäffner, "Radiopurity of an archaeological Roman lead cryogenic detector," *The European Physical Journal A*, vol. 55, no. 8, pp. 1–6, 2019.

[59] C. Alduino, K. Alfonso, D. Artusa, F. Avignone, O. Azzolini, T. Banks, G. Bari, J. Beeman, F. Bellini, G. Benato *et al.*, "The projected background for the CUORE experiment," *The European Physical Journal C*, vol. 77, no. 8, pp. 1–16, 2017.

[60] D. Twerenbold, "Cryogenic particle detectors," *Reports on Progress in Physics*, vol. 59, no. 3, p. 349, 1996.

[61] Y. Levinson, "Propagation of Nonequilibrium Phonons with Frequency Down-conversion: Anthracene," *Molecular Crystals and Liquid Crystals*, vol. 57, no. 1, pp. 23–38, 1980.

[62] A. Alessandrello, J. Beeman, C. Brofferio, O. Cremonesi, E. Fiorini, A. Giuliani, E. Haller, A. Monfardini, A. Nucciotti, M. Pavan *et al.*, "High energy resolution bolometers for nuclear physics and X-ray spectroscopy," *Physical Review Letters*, vol. 82, no. 3, p. 513, 1999.

[63] H.-C. Stahl, "Cryogenic Particle Detection," 2005.

[64] A. Miller and E. Abrahams, "Impurity conduction at low concentrations," *Physical Review*, vol. 120, no. 3, p. 745, 1960.

[65] B. I. Shklovskii and A. L. Efros, *Electronic properties of doped semiconductors*. Springer Science & Business Media, 2013, vol. 45.

[66] C. Arnaboldi, P. Carniti, L. Cassina, C. Gotti, X. Liu, M. Maino, G. Pessina, C. Rosenfeld, and B. Zhu, "A front-end electronic system for large arrays of bolometers," *Journal of Instrumentation*, vol. 13, no. 02, p. P02026, 2018.

[67] C. Arnaboldi, M. Cariello, S. Di Domizio, A. Giachero, and G. Pessina, "A programmable multichannel antialiasing filter for the CUORE experiment," *Nuclear Instruments and Methods in Physics Research Section A: Accelerators, Spectrometers, Detectors and Associated Equipment*, vol. 617, no. 1-3, pp. 327–328, 2010.

[68] S. Di Domizio, A. Branca, A. Caminata, L. Canonica, S. Copello, A. Giachero, E. Guardincerri, L. Marini, M. Pallavicini, and M. Vignati, "A data acquisition and control system for large mass bolometer arrays," *Journal of Instrumentation*, vol. 13, no. 12, p. P12003, 2018.

[69] S. Copello, S. Di Domizio, A. Branca, A. Caminata, L. Canonica, A. Giachero, E. Guardincerri, L. Marini, M. Pallavicini, and M. Vignati, "The CUORE Data Acquisition System," *Journal of Low Temperature Physics*, vol. 199, no. 1, pp. 258–263, 2020.

[70] K. Alfonso, P. Carniti, L. Cassina, A. Giachero, C. Gotti, and G. Pessina, "A high precision pulse generation and stabilization system for bolometric experiments," *Journal of Instrumentation*, vol. 13, no. 02, p. P02029, 2018.

[71] S. Di Domizio, F. Orio, and M. Vignati, "Lowering the energy threshold of large-mass bolometric detectors," *Journal of Instrumentation*, vol. 6, no. 02, p. P02007, 2011.

[72] L. Gladstone, D. Biare, L. Cappelli, J. Cushman, F. Del Corso, B. Fujikawa, K. Hickerson, N. Moggi, C. Pagliarone, B. Schmidt *et al.*, "The CUORE slow monitoring systems," in *Journal of Physics: Conference Series*, vol. 888, no. 1. IOP Publishing, 2017, p. 012234.

[73] I. Nutini, "The CUORE experiment: detector optimization and modelling and CPT conservation limit," 2019.

[74] C. Alduino, K. Alfonso, D. Artusa, F. Avignone III, O. Azzolini, T. Banks, G. Bari, J. Beeman, F. Bellini, A. Bersani *et al.*, "Analysis techniques for the evaluation of the neutrinoless double-β decay lifetime in ^{130}Te with the CUORE-0 detector," *Physical Review C*, vol. 93, no. 4, p. 045503, 2016.

[75] A. Alessandrello, C. Brofferio, C. Bucci, O. Cremonesi, A. Giuliani, B. Margesin, A. Nucciotti, M. Pavan, G. Pessina, E. Previtali *et al.*, "Methods for response stabilization in bolometers for rare decays," *Nuclear Instruments and Methods in Physics*

Research Section A: Accelerators, Spectrometers, Detectors and Associated Equipment, vol. 412, no. 2-3, pp. 454–464, 1998.

[76] J. S. Cushman, A. Dally, C. J. Davis, L. Ejzak, D. Lenz, K. E. Lim, K. M. Heeger, R. H. Maruyama, A. Nucciotti, S. Sangiorgio *et al.*, "The detector calibration system for the CUORE cryogenic bolometer array," *Nuclear Instruments and Methods in Physics Research Section A: Accelerators, Spectrometers, Detectors and Associated Equipment*, vol. 844, pp. 32–44, 2017.

[77] I. T. Jolliffe and J. Cadima, "Principal component analysis: a review and recent developments," *Philosophical Transactions of the Royal Society A: Mathematical, Physical and Engineering Sciences*, vol. 374, no. 2065, p. 20150202, 2016.

[78] R. G. Huang, "Searching for $0\nu\beta\beta$ Decay with CUORE and CUPID," Ph.D. dissertation, University of California, Berkeley, 2021.

[79] S. Agostinelli, J. Allison, K. a. Amako, J. Apostolakis, H. Araujo, P. Arce, M. Asai, D. Axen, S. Banerjee, G. Barrand *et al.*, "GEANT4—a simulation toolkit," *Nuclear instruments and methods in physics research section A: Accelerators, Spectrometers, Detectors and Associated Equipment*, vol. 506, no. 3, pp. 250–303, 2003.

[80] R. Persiani, "Measurement of the muon-induced neutron flux at LNGS with the LVD experiment," 2011.

[81] G. Cowan, *Statistical data analysis*. Oxford university press, 1998.

[82] S. Depaoli, J. P. Clifton, and P. R. Cobb, "Just another gibbs sampler (jags) flexible software for mcmc implementation," *Journal of Educational and Behavioral Statistics*, vol. 41, no. 6, pp. 628–649, 2016.

[83] E. Armengaud, C. Augier, A. Barabash, F. Bellini, G. Benato, A. Benoit, M. Beretta, L. Bergé, J. Billard, Y. A. Borovlev *et al.*, "New Limit for Neutrinoless Double-Beta Decay of ^{100}Mo from the CUPID-Mo Experiment," *Physical review letters*, vol. 126, no. 18, p. 181802, 2021.

Acknowledgments

I take here the opportunity to express my sincere gratitude to my supervisors Prof. Stefano Zucchelli and Dott. Giovanni Benato for helping me in the development of my thesis, while providing me with more than valuable knowledge on a sort of new research field for me. I also thank them for giving me the opportunity to present and discuss my work with the components of the CUORE collaboration, which also allowed them to know me better from a scientific point of view. During this months, I learnt a lot from them and from the whole collaboration and I hope that I gave even something small back.

Here I explicitly apologize to Giovanni for all the questions asked and all the doubts that he solved for me while he was in a different country almost every month. He was very helpful, with tips, comments and material for my work. I very much look up to him as a researcher and as a person.

My, and I think many others, experience as students in these years has been, let's say, tough, but I still want to thank every professor that I met. They did a phenomenal job in teaching us during these unusual years and in preparing us to achieve our future goals. With a particular mention to Prof. Maximiliano Sioli, he was like a mentor during my bachelors' degree and he also introduced me to the CUORE collaboration.

I thank all my closest friends at UNIBO: Ana, Chiara, Davide, Elisa and Luca for their support and help during the masters' years. I very much wish them the best for their careers in the research field they love the most.

Basketball has been and always will be part of my life, I take the opportunity to thank every one that I shared the court with as a teammate and as opponents. This helped me being a better team person and allowed me to meet many wonderful people.

I would like to thank my long time friends Claudio, Eugenia and Giovanni; I know them for more than ten years and I would like to spend one hundred more grilling and making fresh pasta, while laughing about old memories and making new ones together.

With them I want to thank the most important person that I ever met, my girlfriend and best friend Margherita. I would not be me without her, she is always there for me expressing her support while also helping me overcome all the challenges and difficulties that I encountered. She is truly the best partner I have ever dreamt of and I cannot wait to see what the future has in store for the two of us.

Lastly, I want to state how grateful I am to my parents, Andrea and Daniela, and my sister Irene. I would not ever achieve all my results in life without them. They always encouraged me and cheered for me unconditionally, while giving me the opportunity and time to pursue my dreams.